

POLITECNICO DI TORINO

Scuola di Dottorato (SCUDO)

Dottorato di Ricerca in Ingegneria Aerospaziale - XXV ciclo

Ecole Doctorale "Connaissance, Langage, Modélisation" (ED139)

Doctorat en mécanique de l'Université Paris Ouest - Nanterre La Défense

Ph.D. Dissertation

**Advanced modelling of multilayered composites
and functionally graded structures by means of
Unified Formulation**



DANIELA CRISAFULLI

Tutors

prof. Erasmo Carrera

prof. Olivier Polit

January 2013

*“... a model must be wrong, in some respects – else it would be the thing itself.
The trick is to see where it is right.”*

Henry A. Bent

Acknowledgements

I would like to thank Professor E.Carrera, from Politecnico di Torino, for his work as Ph.D. Tutor and the Ministère de la Culture, de l'Enseignement Supérieur et de la Recherche of Luxembourg, through the Fond National de la Recherche, for the support to this research via the AFR Grant PHD-MARP-03. Thanks to the Public Research Center Henri Tudor of Luxembourg, and to Dr. G.Giunta, for his supervision regarding the first part of the thesis. As far as the second part of the thesis, I want to thank Dr. M.Cinefra. Further thank you goes to the University Paris X, for the co-tutorship carried out by Professor O.Polit.

Summary

Most of the engineering problems of the last two centuries have been solved thanks to structural models for both beams, and for plates and shells. Classical theories, such as Euler-Bernoulli, Navier and De Saint-Venant for beams, and Kirchhoff-Love and Mindlin-Reissner for plates and shells, permitted to reduce the generic 3-D problem, in one-dimensional one for beams and two-dimensional for shells and plates. Refined higher order theories have been proposed in the course of time, as the classical models do not consent to obtain a complete stress/strain field.

Carrera Unified Formulation (UF) has been proposed during the last decade, and allows to develop a large number of structural theories with a variable number of main unknowns by means of a compact notation and referring to few fundamental nuclei. This Unified Formulation allows to derive straightforwardly higher-order structural models, for beams, plates and shells. In this framework, this thesis aims to extend the formulation for the analysis of Functionally Graded structures, introducing also the thermo-mechanical problem, in the case of functionally graded beams. Following the Unified Formulation, the generic displacements variables are written in terms of a base functions, which multiplies the unknowns. In the second part of the thesis, new bases functions for shells modelling, accounting for trigonometric approximation of the displacements variables, are considered.

Sommario

La maggior parte dei problemi ingegneristici degli ultimi due secoli sono stati risolti grazie a modelli strutturali per travi, piastre e gusci. Le teorie classiche, come ad esempio Eulero-Bernoulli, Navier e De Saint-Venant per le travi, e Kirchhoff-Love e Mindlin-Reissner per piastre e gusci, hanno permesso di ridurre il generico problema 3-D, a problemi monodimensionali per le travi e bidimensionali per gusci e piastre. Teorie di ordine superiore sono state proposte nel corso del tempo, in quanto i modelli classici non consentono di ottenere un campo completo di tensioni e deformazioni. La Carrera Unified Formulation (UF) $\tilde{\sim}$ stata proposta nel corso dell'ultimo decennio, e permette di sviluppare un gran numero di teorie strutturali con un numero variabile di incognite mediante una notazione compatta e con riferimento pochi nuclei fondamentali. Questa formulazione unificata permette di derivare semplicemente modelli strutturali di ordine superiore, per travi, piastre e gusci. In questo quadro, questa tesi si propone di estendere la formulazione unificata per l'analisi di strutture Functionally Graded (FGM), introducendo anche il problema termomeccanico, nel caso di travi FGM. Grazie alla formulazione unificata, le generiche variabili spostamento sono scritte in termini di funzioni di base, che moltiplicano le incognite. Nella seconda parte della tesi sono state introdotte nuove basi di funzioni per la modellazione di strutture a guscio, basate sull'approssimazione delle variabili spostamento secondo funzioni trigonometriche.

Résumé

La plupart des problèmes d'ingénierie des deux derniers siècles ont été résolus grâce à des modèles structuraux pour poutres, plaques et coques. Les théories classiques, tels que Euler-Bernoulli, Navier et de Saint-Venant pour les poutres, et Kirchhoff-Love et Mindlin-Reissner pour plaques et coques, ont permis de réduire le problème générique 3-D, dans le problème unidimensionnel pour les poutres et deux dimensionnelle pour les coques et les plaques. Théories raffinés d'ordre supérieur ont été proposées au cours du temps, comme les modèles classiques ne consentent pas à d'obtenir une complète domaine des contraintes et des déformations. La Carrera Unified Formulation (UF) a été proposé au cours de la dernière décennie, et permet de développer un grand nombre de théories structurelles avec un nombre variable d'inconnues principales au moyen d'une notation compacte et se référant à des nuclei fondamentales. Cette formulation unifiée permet de dériver carrément des modèles structurels d'ordre supérieur, pour les poutres, plaques et coques. Dans ce cadre, cette thèse vise à étendre la formulation pour l'analyse des structures fonctionnellement gradués (FGM), en introduisant aussi le problème thermo-mécanique, dans le cas des poutres fonctionnellement gradués. Suite à la formulation unifiée, les variables génériques déplacements sont écrits en termes de fonctions de base, qui multiplie les inconnues. Dans la deuxième partie de la thèse, de nouvelles fonctions de bases pour la modélisation des coques, qui représentent une approximation trigonométrique des variables déplacements, sont pris en compte.

Contents

Acknowledgements	v
Summary	vii
Sommario	ix
Résumé	xi
1 Introduction	1
2 Beam's Higher-order Modelling	3
2.1 Introduction	3
2.2 Modelling Literature Review	3
2.3 Higher-order models based on Carrera's Unified Formulation	4
2.3.1 Preliminaries	5
2.4 Hierarchical Beam Theories	6
2.5 Governing Equations	8
2.5.1 Virtual Variation of the Strain Energy	8
2.5.2 Virtual Variation of the Inertial Work	9
2.5.3 Governing Equations' Fundamental Nucleo	10
2.6 Closed Form Analytical Solution	11
2.7 Numerical Results and Discussion	11
2.7.1 Square Cross-Section	12
2.7.2 Box Cross-Section	14
2.7.3 I Cross-Section	19
2.7.4 C Cross-Section	26
2.8 Conclusions	34
3 Functionally Graded Materials	35
3.1 Introduction	35
3.2 FGMs Laws	35
3.3 Free vibration analysis of Functionally Graded Beams: Overview	36
3.4 Constitutive equations for FG beams	37
3.5 Numerical Results and Discussion	37

3.5.1	Material gradation along a cross-section direction	38
3.5.2	Material gradation along both cross-section directions	38
3.6	Conclusions	45
4	Thermo-mechanical analysis of orthotropic and FG beams	46
4.1	Introduction	46
4.2	Unified formulation for thermo-mechanical analysis of beams: overview . . .	47
4.2.1	Constitutive equations for thermo-mechanical problems	48
4.2.2	Fourier's heat conduction equation	49
4.3	Governing Equations	50
4.4	Closed Form Analytical Solution	53
4.5	Numerical Results and Discussion	53
4.5.1	Isotropic material	53
4.5.2	Orthotropic material	61
4.5.3	Functionally Graded Materials	63
4.5.4	Sandwich FGM beam	78
4.6	Conclusions	85
5	Refined shell's and plate's theories via Unified Formulation	86
5.1	Introduction	86
5.2	Geometry	89
5.3	Overview of the considered Shell Theories	90
5.3.1	Classical theories	90
5.3.2	Higher Order Theories	91
5.3.3	Layer-Wise Theories	92
5.3.4	Mixed Theories based on Reissner's Mixed Variational Theorem . .	93
5.3.5	Carrera Unified Formulation	93
5.4	Governing Equations	93
5.5	Results	97
5.5.1	Assessment	98
5.5.2	Influence of the degree of orthotropy	100
5.5.3	Effect of the lamination sequence	101
5.5.4	Influence of the Radius-to-Thickness ratio and Love's approximation	102
5.5.5	Analysis of curvature parameter and Donnell effect	104
5.5.6	Natural frequencies versus wave mode number curves	105
5.6	Conclusions	109
6	Trigonometric basis functions and Unified Formulation	110
6.1	Introduction	110
6.2	Trigonometric Shell Theories	111
6.2.1	Equivalent single layer model	111
6.2.2	Layer-wise approach	112
6.2.3	Carrera Unified Formulation	112
6.3	Governing Equations	113

6.3.1	Equations for the N_l layers	113
6.3.2	Assemblage and Multilayer equations	115
6.4	Closed form solution	115
6.5	Numerical Results and Discussion	117
6.5.1	Assessment	117
6.5.2	Bending of Plates	118
6.5.3	Bending of Shells	126
6.6	Conclusions	133
7	Conclusions	134
	Bibliography	136

Chapter 1

Introduction

The present thesis concerns with a unified approach, named 'Carrera Unified Formulation (UF)' that allows to formulate several axiomatic theories for beams, plates and shells structures. The first part of the thesis present the formulation for beam structures. After a brief introduction and literature survey on beam modelling, we introduce the UF for beam with solid and thin-walled cross-section and results for the modal analysis of such structures is carried out. The concept of the Unified Formulation in beams structure analysis is to assume A N -order polynomials approximation on the cross-section for the displacement unknown variables. The three-dimensional kinematic field is derived in a compact form as a generic N -order approximation, being N a free parameter of the formulation. The governing differential equations and the boundary conditions are derived by variationally imposing the equilibrium via the principle of virtual displacements. They are written in terms of a fundamental nucleo that does not depend upon the approximation order. The free vibration analysis of solid and thin-walled isotropic beams is carried out through a closed form, Navier type solution. Bending, torsional and axial modes, as well as local modes are considered. Results are assessed toward finite element solutions.

The free vibration analysis of functionally graded beams via higher-order models and unified formulation is straight after considered.

Functionally graded materials are a class of composite materials, whose mechanical and thermal properties vary continuously on the space directions according to a specific gradation law, in order to accomplish certain functions. Bones are an example of functionally graded materials present in nature. In general these materials are made of a metal and a ceramic component, since their principal purpose concern high-temperature application. We considered a power law distribution in terms of volume fraction of material constituents, along the cross-section of the beam. Young's modulus, Poisson's ratio and density vary along one or two dimensions of the cross-section. A Navier-type, closed form solution is adopted. Higher-order displacements-based theories that account for non-classical effects are formulated. Classical beam models, such as Euler-Bernoulli's and Timoshenko's, are obtained as particular cases.

The thermal behaviour of beams made of orthotropic and functionally graded materials is also investigated. The governing equations are derived from the principle of virtual

displacements accounting for the temperature field as an external load only. The required temperature field is not assumed a priori, but is determined solving Fourier's heat conduction equation. Numerical results for temperature, displacements and stress distributions are provided and moreover a comparison with finite elements solutions obtained via the commercial code ANSYS are presented.

The second part of the thesis presents the derivation of various shell's and plate's theories, based on the Unified Formulation, where the assumed displacements field is written in terms of new trigonometric basis functions of the thickness coordinate. To introduce this topic we presented a comparison of several, significant shell theories to evaluate the free vibration response of multi-layered, orthotropic cylindrical shells. Carrera Unified Formulation for the modelling of composite spherical shell structures is adopted. Via this approach, higher order, zig-zag, layer-wise and mixed theories can be easily formulated. As a particular case, the equations related to Love's approximations and Donnell's approximations and as well as of the corresponding classical lamination and shear deformation theories (CLT and FSDT) are derived. The governing differential equations of the dynamic problem are presented in a compact general form. These equations are solved via a Navier-type, closed form solution.

Equivalent single layer and Layer-wise shells theories based on trigonometric functions expansions are derived in chapter 6. The aim of this part is to extend the bases functions used for higher order shell theories, in the framework of Carrera Unified Formulation, to new trigonometric basis functions, outlined in an appropriate way. These theories are then considered to evaluate the static behaviour of multilayered, orthotropic plates and shells.

Chapter 2

Beam's Higher-order Modelling

2.1 Introduction

Modelling refers to the process of generating a model, and in particular a mathematical model, as a conceptual representation of some phenomenon. A mathematical model is a representation, similar but simpler, of an object or system, using mathematical concepts and language. A beam is a structural element, characterized by a prevalent dimension over the other two, that is capable of withstand load primarily by resisting bending. An important feature of the beams is the cross-section shape, that can be solid or thin-walled. Many primary and secondary structural elements, such as helicopter rotor blades, automotive frames, robot arms and space erect-able booms, can be idealised as beams. These structures play an important role in engineering fields (such as aeronautics and space) in which an effective and safe design is mandatory.

2.2 Modelling Literature Review

There are different beam models with different accuracy present in literature. Classical beam models are based on the theories developed by Euler-Bernoulli [12], [43], De Saint-Venant [40], [40] and Timoshenko [115], [116]. The first two models neglect transverse shear deformation, whereas the last model accounts for uniform shear distribution along the beam cross-section. Non classical effects are not identified by these theories and therefore it required the development of higher-order theories. A review of historical contributions to refined beams theories can be find in the book of Carrera et al. [31]. The free vibration characteristics are of fundamental importance in the design of beam structures, and therefore, the analysis of solid and thin-walled isotropic beams via refined theories represents an interesting research topic. Benamar et al. [11] presented a general model for large vibration amplitudes of thin straight beams. Hamilton's principle was used to determine a set of non-linear algebraic equations. A condition is imposed on the contribution of one motion in order to obtain a numerical solution for the non-linear problem. Simply supported and clamped-clamped boundary condition were investigated. Matsunaga [72] analysed the natural frequencies and buckling loads of simply supported beams subjected

to initial axial forces. Thin rectangular cross-sections were investigated. A bi-dimensional displacement field was assumed. Chen et al. [37] combined the state space method with the differential quadrature method to obtain a semi-analytical method for the free vibration analysis of straight isotropic and orthotropic beams with rectangular cross-sections. A discussion about properties of the natural frequencies and modes for a Timoshenko beam was presented by Van Rensburg and Van Der Merwe [118]. In [7] Attarnejad et al. introduced the basic displacement functions (BDF), that are calculated solving the governing differential equations of transverse motion of Timoshenko beams by means of power series method. BDF are applied for free vibration analysis of non-prismatic beams. Gunda et al. [51] analyzed the large amplitude free vibration of Timoshenko beams using a finite element formulation. Transverse shear and rotatory inertia are considered, together with several boundary conditions. Tanaka and Bercin [113] studied the natural frequencies of uniform thin-walled beams having no cross sectional symmetry. A study on the free vibration of axially loaded slender thin-walled beams is presented in the work by Jun et al. [56]. The effects of warping stiffness and axial force are included within the Euler-Bernoulli beam theory. Chen and Hsiao [35] investigated the natural frequency of the axial and torsional vibration for Z-section beams. The governing equations are derived by the principle of virtual work. Numerical examples investigate the effect of boundary conditions. In [36], the same authors presented a finite element formulation for the coupled free vibration analysis of thin-walled beams with a generic open cross-section. Duan [42] presented a finite element formulation for the non-linear free vibration of thin-walled curved beams with non-symmetric open cross-section. Vörös [123] accounted for the coupling between different vibration modes considering that is induced not only by the eccentricity of geometry but also by steady state lateral loads and internal stress resultants. The governing differential equations and boundary conditions were derived using the linearized theory of large rotations and small strains, the principle of virtual work and a finite element model with seven degrees of freedom per node. Ambrosini [3, 4] presented a numerical and experimental study on the natural frequencies of doubly non-symmetrical thin-walled and open cross-section beams. Vlasov’s theory equations of motion were modified to include the effects of shear deformation, rotatory inertia and variable cross-section properties. An extension of the previous theory is used in the work of Borbón and Ambrosini [39] to investigate natural frequencies of thin-walled beams axially loaded. They carried out experimental tests in order to verify the proposed theory.

2.3 Higher-order models based on Carrera’s Unified Formulation

In the following sections we present results for higher-order beams models derived via a Unified Formulation (UF) that has been previously formulated for plates and shells, (see Carrera [26]). In the Unified Formulation the displacements’ assumptions are written in a compact form. The governing equations variationally consistent with the made hypothesis are derived through the Principle of Virtual Displacements, in terms of ‘fundamental nucleo’. This is a free parameter of the formulation, since it does not depend upon the order

of expansion. As a result, an exhaustive variable kinematic model can be obtained that accounts for transverse shear deformability and cross-section in- and out-of-plane warping. Classic and higher modes are predicted although no warping functions are assumed.

2.3.1 Preliminaries

A beam is a structure whose axial extension (l) is predominant if compared to any other dimension orthogonal to it. The cross-section (Ω) is identified by intersecting the beam with planes that are orthogonal to its axis. A Cartesian reference system is adopted: y - and z -axis are two orthogonal directions laying on Ω . The x coordinate is coincident to the axis of the beam. Cross-sections that are obtainable by the union of N_{Ω^k} rectangular sub-domains:

$$\Omega = \bigcup_{k=1}^{N_{\Omega^k}} \Omega^k \quad (2.1)$$

with:

$$\Omega^k = \left\{ (y, z) : y_1^k \leq y \leq y_2^k; z_1^k \leq z \leq z_2^k \right\} \quad (2.2)$$

are considered, see Fig. 1. Terms $\left\{ (y_i^k, z_j^k) : i, j = 1, 2 \right\}$ are the coordinates of the corner points of a k sub-domain. Through the paper, superscript ‘ k ’ represents a cross-section sub-domain index, while, as subscript, it stands for summation over the range $[1, N_{\Omega^k}]$. The cross-section is considered to be constant along x . The displacement field is:

$$\mathbf{u}^T(x, y, z) = \left\{ u_x(x, y, z) \quad u_y(x, y, z) \quad u_z(x, y, z) \right\} \quad (2.3)$$

in which u_x , u_y and u_z are the displacement components along x -, y - and z -axes. Superscript ‘ T ’ represents the transposition operator. Stress, $\boldsymbol{\sigma}$, and strain, $\boldsymbol{\varepsilon}$, vectors are grouped into vectors $\boldsymbol{\sigma}_n$, $\boldsymbol{\varepsilon}_n$ that lay on the cross-section:

$$\boldsymbol{\sigma}_n^T = \left\{ \sigma_{xx} \quad \sigma_{xy} \quad \sigma_{xz} \right\} \quad \boldsymbol{\varepsilon}_n^T = \left\{ \varepsilon_{xx} \quad \varepsilon_{xy} \quad \varepsilon_{xz} \right\} \quad (2.4)$$

and $\boldsymbol{\sigma}_p$, $\boldsymbol{\varepsilon}_p$ laying on planes orthogonal to Ω :

$$\boldsymbol{\sigma}_p^T = \left\{ \sigma_{yy} \quad \sigma_{zz} \quad \sigma_{yz} \right\} \quad \boldsymbol{\varepsilon}_p^T = \left\{ \varepsilon_{yy} \quad \varepsilon_{zz} \quad \varepsilon_{yz} \right\} \quad (2.5)$$

The strain-displacement geometrical relations are:

$$\begin{aligned} \boldsymbol{\varepsilon}_n^T &= \left\{ u_{x,x} \quad u_{x,y} + u_{y,x} \quad u_{x,z} + u_{z,x} \right\} \\ \boldsymbol{\varepsilon}_p^T &= \left\{ u_{y,y} \quad u_{z,z} \quad u_{y,z} + u_{z,y} \right\} \end{aligned} \quad (2.6)$$

Subscripts ‘ x ’, ‘ y ’ and ‘ z ’, when preceded by comma, represent derivation versus the corresponding spatial coordinate. A compact vectorial notation can be adopted for Eqs. (2.6):

$$\begin{aligned} \boldsymbol{\varepsilon}_n &= \mathbf{D}_{np} \mathbf{u} + \mathbf{D}_{nx} \mathbf{u} \\ \boldsymbol{\varepsilon}_p &= \mathbf{D}_p \mathbf{u} \end{aligned} \quad (2.7)$$

where \mathbf{D}_{np} , \mathbf{D}_{nx} , and \mathbf{D}_p are the following differential matrix operators:

$$\mathbf{D}_{np} = \begin{bmatrix} 0 & 0 & 0 \\ \frac{\partial}{\partial y} & 0 & 0 \\ \frac{\partial}{\partial z} & 0 & 0 \end{bmatrix} \quad \mathbf{D}_{nx} = \mathbf{I} \frac{\partial}{\partial x} \quad \mathbf{D}_p = \begin{bmatrix} 0 & \frac{\partial}{\partial y} & 0 \\ 0 & 0 & \frac{\partial}{\partial z} \\ 0 & \frac{\partial}{\partial z} & \frac{\partial}{\partial y} \end{bmatrix} \quad (2.8)$$

\mathbf{I} is the unit matrix. Under the hypothesis of linear elastic materials, the generalised Hooke law holds. According to Eqs. (2.4) and (2.5), it reads:

$$\begin{aligned} \boldsymbol{\sigma}_p &= \mathbf{C}_{pp}\boldsymbol{\varepsilon}_p + \mathbf{C}_{pn}\boldsymbol{\varepsilon}_n \\ \boldsymbol{\sigma}_n &= \mathbf{C}_{np}\boldsymbol{\varepsilon}_p + \mathbf{C}_{nn}\boldsymbol{\varepsilon}_n \end{aligned} \quad (2.9)$$

Matrices \mathbf{C}_{pp} , \mathbf{C}_{pn} , \mathbf{C}_{np} and \mathbf{C}_{nn} in Eqs. (2.9) are:

$$\begin{aligned} \mathbf{C}_{pp} &= \begin{bmatrix} C_{22} & C_{23} & 0 \\ C_{23} & C_{33} & 0 \\ 0 & 0 & C_{44} \end{bmatrix} & \mathbf{C}_{pn} &= \mathbf{C}_{np}^T = \begin{bmatrix} C_{12} & 0 & 0 \\ C_{13} & 0 & 0 \\ 0 & 0 & 0 \end{bmatrix} \\ \mathbf{C}_{nn} &= \begin{bmatrix} C_{11} & 0 & 0 \\ 0 & C_{66} & 0 \\ 0 & 0 & C_{55} \end{bmatrix} \end{aligned} \quad (2.10)$$

In the case of isotropic material, coefficients C_{ij} are:

$$\begin{aligned} C_{11} = C_{22} = C_{33} &= \frac{1 - \nu}{(1 + \nu)(1 - 2\nu)} E & C_{12} = C_{13} = C_{23} &= \frac{\nu}{(1 + \nu)(1 - 2\nu)} E \\ C_{44} = C_{55} = C_{66} &= \frac{1}{2(1 + \nu)} E \end{aligned} \quad (2.11)$$

being E the Young modulus and ν the Poisson ratio.

2.4 Hierarchical Beam Theories

The variation of the displacement field over the cross-section can be postulated a-priori. Several displacement-based theories can be formulated on the basis of the following generic kinematic field:

$$\mathbf{u}(x, y, z) = F_\tau(y, z) \mathbf{u}_\tau(x) \quad \text{with } \tau = 1, 2, \dots, N_u \quad (2.12)$$

N_u stands for the number of unknowns. It depends on the approximation order N that is a free parameter of the formulation. The compact expression is based on Einstein’s notation: subscript τ indicates summation. Thanks to this notation, problem’s governing differential equations and boundary conditions can be derived in terms of a single ‘fundamental nucleo’. The theoretical formulation is valid for the generic approximation order

N	N_u	F_τ
0	1	$F_1 = 1$
1	3	$F_2 = y \quad F_3 = z$
2	6	$F_4 = y^2 \quad F_5 = yz \quad F_6 = z^2$
3	10	$F_7 = y^3 \quad F_8 = y^2z \quad F_9 = yz^2 \quad F_{10} = z^3$
...
N	$\frac{(N+1)(N+2)}{2}$	$F_{\frac{(N^2+N+2)}{2}} = y^N \quad F_{\frac{(N^2+N+4)}{2}} = y^{N-1}z \quad \dots$ $\dots \quad F_{\frac{N(N+3)}{2}} = yz^{N-1} \quad F_{\frac{(N+1)(N+2)}{2}} = z^N$

Table 2.1. Mac Laurin’s polynomials terms via Pascal’s triangle.

and approximating functions $F_\tau(y, z)$. In the following, the functions F_τ are assumed to be Mac Laurin’s polynomials. This choice is inspired by the classical beam models. N_u and F_τ as functions of N can be obtained via Pascal’s triangle as shown in Table 2.1. The actual governing differential equations and boundary conditions due to a fixed approximation order and polynomials type are obtained straightforwardly via summation of the nucleo corresponding to each term of the expansion. According to the previous choice of polynomial function, the generic, N -order displacement field is:

$$\begin{aligned}
 u_x &= u_{x1} + u_{x2}y + u_{x3}z + \dots + u_{x\frac{(N^2+N+2)}{2}}y^N + \dots + u_{x\frac{(N+1)(N+2)}{2}}z^N \\
 u_y &= u_{y1} + u_{y2}y + u_{y3}z + \dots + u_{y\frac{(N^2+N+2)}{2}}y^N + \dots + u_{y\frac{(N+1)(N+2)}{2}}z^N \\
 u_z &= u_{z1} + u_{z2}y + u_{z3}z + \dots + u_{z\frac{(N^2+N+2)}{2}}y^N + \dots + u_{z\frac{(N+1)(N+2)}{2}}z^N
 \end{aligned} \tag{2.13}$$

As far as the first-order approximation order is concerned, the kinematic field is:

$$\begin{aligned}
 u_x &= u_{x1} + u_{x2}y + u_{x3}z \\
 u_y &= u_{y1} + u_{y2}y + u_{y3}z \\
 u_z &= u_{z1} + u_{z2}y + u_{z3}z
 \end{aligned} \tag{2.14}$$

Classical models, such as Timoshenko’s beam theory (TB):

$$\begin{aligned}
 u_x &= u_{x1} + u_{x2}y + u_{x3}z \\
 u_y &= u_{y1} \\
 u_z &= u_{z1}
 \end{aligned} \tag{2.15}$$

and Euler-Bernoulli beam theory (EB):

$$\begin{aligned}
 u_x &= u_{x1} - u_{y1,x}y - u_{z1,x}z \\
 u_y &= u_{y1} \\
 u_z &= u_{z1}
 \end{aligned} \tag{2.16}$$

are straightforwardly derived from the first-order approximation model. In TB, no shear correction coefficient is considered, since it depends upon several parameters, such as the

geometry of the cross-section (see, for instance, Cowper [38] and Murty [78]). Higher order models yield a more detailed description of the shear mechanics (no shear correction coefficient is required), of the in- and out-of-section deformations, of the coupling of the spatial directions due to Poisson’s effect and of the torsional mechanics than classical models do. EB theory neglects them all, since it was formulated to describe the bending mechanics. TB model accounts for constant shear stress and strain components. In the case of classical models and first-order approximation, the material stiffness coefficients should be corrected in order to contrast a phenomenon known in literature as Poisson’s locking (see Carrera and Brischetto [28, 29]).

2.5 Governing Equations

The Principle of Virtual Displacements reads:

$$\delta L_i + \delta L_{in} = 0 \quad (2.17)$$

δ stands for a virtual variation, L_i represents the strain energy and L_{in} stands for the inertial work.

2.5.1 Virtual Variation of the Strain Energy

According to the grouping of the stress and strain components in Eqs. (2.4) and (2.5), the virtual variation of the strain energy is considered as sum of two contributes:

$$\delta L_i = \int_l \left(\int_{\Omega^k} \delta \epsilon_n^T \boldsymbol{\sigma}_n d\Omega \right)_k dx + \int_l \left(\int_{\Omega^k} \delta \epsilon_p^T \boldsymbol{\sigma}_p d\Omega \right)_k dx \quad (2.18)$$

By substitution of the geometrical relations, Eqs. (2.7), the material constitutive equations, Eqs. (2.9), and the unified hierarchical approximation of the displacements, Eq. (2.12), and after integration by parts, Eq. (2.18) reads:

$$\begin{aligned} \delta L_i = & \int_l \delta \mathbf{u}_\tau^T \left(\int_{\Omega^k} \left[-\mathbf{D}_{nx}^T \mathbf{C}_{np}^k F_\tau (\mathbf{D}_p F_s \mathbf{I}) - \mathbf{D}_{nx}^T \mathbf{C}_{nn}^k F_\tau (\mathbf{D}_{np} F_s \mathbf{I}) + \right. \right. \\ & -\mathbf{D}_{nx}^T \mathbf{C}_{nn}^k F_\tau F_s \mathbf{D}_{nx} + (\mathbf{D}_{np} F_\tau \mathbf{I})^T \mathbf{C}_{np}^k (\mathbf{D}_p F_s \mathbf{I}) + (\mathbf{D}_{np} F_\tau \mathbf{I})^T \mathbf{C}_{nn}^k (\mathbf{D}_{np} F_s \mathbf{I}) + \\ & + (\mathbf{D}_{np} F_\tau \mathbf{I})^T \mathbf{C}_{nn}^k F_s \mathbf{D}_{nx} + (\mathbf{D}_p F_\tau \mathbf{I})^T \mathbf{C}_{pp}^k (\mathbf{D}_p F_s \mathbf{I}) + (\mathbf{D}_p F_\tau \mathbf{I})^T \mathbf{C}_{pn}^k (\mathbf{D}_{np} F_s \mathbf{I}) + \\ & \left. \left. + (\mathbf{D}_p F_\tau \mathbf{I})^T \mathbf{C}_{pn}^k F_s \mathbf{D}_{nx} \right] d\Omega \right)_k \mathbf{u}_s dx + \\ & + \left[\delta \mathbf{u}_\tau^T \left(\int_{\Omega^k} F_\tau \left[\mathbf{C}_{np}^k (\mathbf{D}_p F_s \mathbf{I}) + \mathbf{C}_{nn}^k (\mathbf{D}_{np} F_s \mathbf{I}) + \mathbf{C}_{nn}^k F_s \mathbf{D}_{nx} \right] d\Omega \right)_k \mathbf{u}_s \right]_{x=0}^{x=l} \end{aligned} \quad (2.19)$$

In a compact vectorial form:

$$\delta L_i = \int_l \delta \mathbf{u}_\tau^T \overline{\mathbf{K}}^{\tau s} \mathbf{u}_s dx + [\delta \mathbf{u}_\tau^T \boldsymbol{\Pi}^{\tau s} \mathbf{u}_s]_{x=0}^{x=l} \quad (2.20)$$

The components of the differential linear stiffness matrix $\overline{\mathbf{K}}^{\tau s}$ are:

$$\begin{aligned}
 \overline{K}_{xx}^{\tau s} &= J_{\tau, y^s, y}^{66} + J_{\tau, z^s, z}^{55} - J_{\tau s}^{11} \frac{\partial^2}{\partial x^2} & \overline{K}_{xy}^{\tau s} &= \left(J_{\tau, y^s}^{66} - J_{\tau s, y}^{12} \right) \frac{\partial}{\partial x} \\
 \overline{K}_{yy}^{\tau s} &= J_{\tau, y^s, y}^{22} + J_{\tau, z^s, z}^{44} - J_{\tau s}^{66} \frac{\partial^2}{\partial x^2} & \overline{K}_{yx}^{\tau s} &= \left(J_{\tau, y^s}^{12} - J_{\tau s, y}^{66} \right) \frac{\partial}{\partial x} \\
 \overline{K}_{zz}^{\tau s} &= J_{\tau, y^s, y}^{44} + J_{\tau, z^s, z}^{33} - J_{\tau s}^{55} \frac{\partial^2}{\partial x^2} & \overline{K}_{zx}^{\tau s} &= \left(J_{\tau, z^s}^{13} - J_{\tau s, z}^{55} \right) \frac{\partial}{\partial x} \\
 & & \overline{K}_{xz}^{\tau s} &= \left(J_{\tau, z^s}^{55} - J_{\tau s, z}^{13} \right) \frac{\partial}{\partial x} \\
 & & \overline{K}_{yz}^{\tau s} &= J_{\tau, y^s, z}^{23} + J_{\tau, z^s, y}^{44} \\
 & & \overline{K}_{zy}^{\tau s} &= J_{\tau, z^s, y}^{23} + J_{\tau, y^s, z}^{44}
 \end{aligned} \tag{2.21}$$

The generic term $J_{\tau(\phi)^s(\xi)}^{gh}$ is a cross-section moment:

$$J_{\tau(\phi)^s(\xi)}^{gh} = \left(\int_{\Omega^k} C_{gh}^k F_{\tau(\phi)} F_{s(\xi)} d\Omega \right)_k \tag{2.22}$$

Be:

$$F_{\tau(\phi)} F_{s(\xi)} = k_y y^{n_y} k_z z^{n_z} \tag{2.23}$$

where k_y , k_z , n_y and n_z are constant depending upon indexes τ and s as in Table 2.1 and whether differentiation with respect to y and z should be performed or not, the analytical solution of integral in Eq. (2.22) is:

$$J_{\tau, \phi^s, \xi}^{gh} = \left\{ C_{gh}^k \frac{k_y}{n_y + 1} \left[\left(y_2^k \right)^{n_y + 1} - \left(y_1^k \right)^{n_y + 1} \right] \frac{k_z}{n_z + 1} \left[\left(z_2^k \right)^{n_z + 1} - \left(z_1^k \right)^{n_z + 1} \right] \right\}_k \tag{2.24}$$

As far as the boundary conditions are concerned, the components of $\mathbf{\Pi}^{\tau s}$ are:

$$\begin{aligned}
 \Pi_{xx}^{\tau s} &= J_{\tau s}^{11} \frac{\partial}{\partial x} & \Pi_{xy}^{\tau s} &= J_{\tau s, y}^{12} & \Pi_{xz}^{\tau s} &= J_{\tau s, z}^{13} \\
 \Pi_{yy}^{\tau s} &= J_{\tau s}^{66} \frac{\partial}{\partial x} & \Pi_{yx}^{\tau s} &= J_{\tau s, y}^{66} & \Pi_{yz}^{\tau s} &= 0 \\
 \Pi_{zz}^{\tau s} &= J_{\tau s}^{55} \frac{\partial}{\partial x} & \Pi_{zx}^{\tau s} &= J_{\tau s, z}^{55} & \Pi_{zy}^{\tau s} &= 0
 \end{aligned} \tag{2.25}$$

2.5.2 Virtual Variation of the Inertial Work

The virtual variation of the inertial work is:

$$\delta L_{in} = \int_l \left(\int_{\Omega^k} \rho^k \delta \mathbf{u}^k \ddot{\mathbf{u}}^k d\Omega \right)_k dx \tag{2.26}$$

where dot stands for differentiation versus time. Upon substitution of Eq. (2.12), Eq. (2.26) becomes:

$$\delta L_{in} = \int_l \delta \mathbf{u}_\tau^T \left(\int_{\Omega^k} \rho^k F_\tau F_s d\Omega \right)_k \ddot{\mathbf{u}}_s dx \quad (2.27)$$

In a compact vectorial form:

$$\delta L_{in} = \int_l \delta \mathbf{u}_\tau^T \overline{\mathbf{M}}^{\tau s} \ddot{\mathbf{u}}_s dx \quad (2.28)$$

The components of the matrix $\overline{\mathbf{M}}^{\tau s}$ are:

$$\overline{M}_{ij}^{\tau s} = \delta_{ij} \rho^k J_{\tau s} \quad \text{with } i, j = x, y, z \quad (2.29)$$

where δ_{ij} is Kronecker’s delta and:

$$J_{\tau s} = \left(\int_{\Omega^k} F_\tau F_s d\Omega \right)_k \quad (2.30)$$

2.5.3 Governing Equations’ Fundamental Nucleo

The explicit form of the fundamental nucleo of the governing equations is:

$$\begin{aligned} & \delta u_{x\tau} : \\ & -J_{\tau s}^{11} u_{xs,xx} + \left(J_{\tau,zs}^{55} + J_{\tau,y}^{66} \right) u_{xs} + \left(J_{\tau,y}^{66} - J_{\tau s}^{12} \right) u_{ys,x} + \left(J_{\tau,zs}^{55} - J_{\tau s}^{13} \right) u_{zs,x} \\ & + \rho^k J_{\tau s} \ddot{u}_{xs} = 0 \\ & \delta u_{y\tau} : \\ & \left(J_{\tau,y}^{12} - J_{\tau s}^{66} \right) u_{xs,x} - J_{\tau s}^{66} u_{ys,xx} + \left(J_{\tau,y}^{22} + J_{\tau,zs}^{44} \right) u_{ys} + \left(J_{\tau,y}^{23} + J_{\tau,zs}^{44} \right) u_{zs} \\ & + \rho^k J_{\tau s} \ddot{u}_{ys} = 0 \\ & \delta u_{z\tau} : \\ & \left(J_{\tau,zs}^{13} - J_{\tau s}^{55} \right) u_{xs,x} + \left(J_{\tau,zs}^{23} + J_{\tau,y}^{44} \right) u_{ys} - J_{\tau s}^{55} u_{zs,xx} + \left(J_{\tau,zs}^{33} + J_{\tau,y}^{44} \right) u_{zs} \\ & + \rho^k J_{\tau s} \ddot{u}_{zs} = 0 \end{aligned} \quad (2.31)$$

The boundary conditions are:

$$\begin{aligned} & \left[\delta u_{x\tau} \left(J_{\tau s}^{11} u_{xs,x} + J_{\tau s}^{12} u_{ys} + J_{\tau s}^{13} u_{zs} \right) \right]_{x=0}^{x=l} = 0 \\ & \left[\delta u_{y\tau} \left(J_{\tau s}^{66} u_{xs} + J_{\tau s}^{66} u_{ys,x} \right) \right]_{x=0}^{x=l} = 0 \\ & \left[\delta u_{z\tau} \left(J_{\tau s}^{55} u_{xs} + J_{\tau s}^{55} u_{zs,x} \right) \right]_{x=0}^{x=l} = 0 \end{aligned} \quad (2.32)$$

For a fixed approximation order, the nucleo has to be expanded versus the indexes τ and s in order to obtain the governing equations and the boundary conditions of the desired model.

2.6 Closed Form Analytical Solution

The previous differential equations are solved via a Navier-type solution. Simply supported beams are, therefore, investigated. The following harmonic displacement field is adopted:

$$\begin{aligned} u_{x\tau} &= U_{x\tau} \cos(\alpha x) e^{i\omega_m t} \\ u_{y\tau} &= U_{y\tau} \sin(\alpha x) e^{i\omega_m t} \\ u_{z\tau} &= U_{z\tau} \sin(\alpha x) e^{i\omega_m t} \end{aligned} \quad (2.33)$$

where α is:

$$\alpha = \frac{m\pi}{l} \quad \text{with } m \in \mathbb{N} \setminus 0 \quad (2.34)$$

m represents the half-wave number along the beam axis. $i = \sqrt{-1}$ is the imaginary unit and t the time. $\{U_{i\tau} : i = x, y, z\}$ are the maximal amplitudes of the displacement components. The displacement field in Eqs. (2.33) satisfies the boundary conditions since:

$$\begin{aligned} u_{x\tau,x}(0) &= u_{x\tau,x}(l) = 0 \\ u_{y\tau}(0) &= u_{y\tau}(l) = 0 \\ u_{z\tau}(0) &= u_{z\tau}(l) = 0 \end{aligned} \quad (2.35)$$

Upon substitution of Eqs. (2.33) into Eqs. (2.31), the fundamental nucleo of the algebraic eigensystem is obtained:

$$\delta \mathbf{U}_\tau : (\mathbf{K}^{\tau s} - \omega_m^2 \mathbf{M}^{\tau s}) \mathbf{U}_s = 0 \quad (2.36)$$

The components of the algebraic stiffness matrix ($\mathbf{K}^{\tau s}$) and of the inertial one ($\mathbf{M}^{\tau s}$) are:

$$\begin{aligned} K_{xx}^{\tau s} &= \alpha^2 J_{\tau s}^{11} + J_{\tau,zs,z}^{55} + J_{\tau,ys,y}^{66} & K_{xy}^{\tau s} &= \alpha \left(J_{\tau,ys}^{66} - J_{\tau s,y}^{12} \right) \\ K_{yy}^{\tau s} &= \alpha^2 J_{\tau s}^{66} + J_{\tau,ys,y}^{22} + J_{\tau,zs,z}^{44} & K_{yx}^{\tau s} &= \alpha \left(J_{\tau s,y}^{66} - J_{\tau,ys}^{12} \right) \\ K_{zz}^{\tau s} &= \alpha^2 J_{\tau s}^{55} + J_{\tau,zs,z}^{33} + J_{\tau,ys,y}^{44} & K_{zx}^{\tau s} &= \alpha \left(J_{\tau s,z}^{55} - J_{\tau,zs}^{13} \right) \\ K_{xz}^{\tau s} &= \alpha \left(J_{\tau,zs}^{55} - J_{\tau s,z}^{13} \right) \\ K_{yz}^{\tau s} &= J_{\tau,ys,z}^{23} + J_{\tau,zs,y}^{44} \\ K_{zy}^{\tau s} &= J_{\tau,zs,y}^{23} + J_{\tau,ys,z}^{44} \end{aligned} \quad (2.37)$$

and:

$$M_{ij}^{\tau s} = \delta_{ij} \rho^k J_{\tau s} \quad \text{with } i, j = x, y, z \quad (2.38)$$

For a fixed approximation order and m , the eigensystem has to be assembled according to the summation indexes τ and s . Its solution yields as many eigenvalues and eigenvectors (or modes) as the degrees of freedom of the model.

2.7 Numerical Results and Discussion

The proposed formulation has been applied to the free vibration analysis of solid and thin-walled beams and these results have been compared with three-dimensional FEM

models. Beams made of the aluminium alloy 7075-T6 are considered. Mechanical properties are: Young’s modulus equal to 71700 MPa, Poisson’s ratio equal to 0.3. Solid and thin-walled cross-sections are considered. For thin-walled cross-sections, the ratio between a representative dimension of the cross-section (a) and the walls’ thickness (h) is 20. a is assumed equal to $2 \cdot 10^{-2}$ m. The length-to-side ratio is as high as 100 and as low as 5. Slender and deep beams are, therefore, investigated. Classical (bending and torsional) and higher modes up to the axial one are investigated. For the sake of brevity the natural frequency related to the axial mode is not included in tables, since this modal shape is already accurately provided by classical theories. Natural frequencies are put into the following dimensionless form:

$$\bar{\omega} = 10^2 \omega a \sqrt{\frac{\rho}{E}} \quad (2.39)$$

As far as validation is concerned, results are compared with three-dimensional FEM solutions obtained via the commercial code ANSYS[®]. The quadratic three-dimensional “Solid95” element is used. A convergence analysis of the three-dimensional FEM solution versus the element sides’ length (x_e, y_e, z_e) is also carried out. Modal shapes are compared via visualisation. Although the three-dimensional FEM solution and the analytical one are different in nature, some considerations about computational time and effort can be addressed. For the reference FEM simulations, the computational time is as high as about five minutes (refined meshes) and as low as about a minute (coarse meshes). In the case of the proposed analytical solutions, the computational time is less than a second for the highest considered approximation order ($N = 15$). The same amount of time is required by a FEM model based on the proposed theories and a very fine mesh (see Carrera et al. [30]). As far as the computational effort is concerned, it should be noticed that the degrees of freedom (DOF) of the three-dimensional reference solution are, at least, about $6 \cdot 10^4$, whereas in the case of a 12^{th} -order analytical model, they are 273.

2.7.1 Square Cross-Section

A square cross-section is considered. Tables 2.2 to 2.4 present the dimensionless natural frequencies for $l/a = 100$, ten and five. Flexural (Mode I, II) and torsional (Mode III) modes are reported. The half-wave number m is assumed equal to one and two. Results are compared with three-dimensional FEM solutions where two different meshes (a refined and a coarse ones) are used in order to show the convergence of the solution.

Due to cross-section symmetry, two bending modes are present. Bending occurs on planes rotated by ± 45 degrees versus y -axis, since the cross-section presents the minimum inertia along those directions. Classical theories results agree with FEM 3D solution for the flexural modes, with a maximum error rate of 0.05% in the case $m = 2$. The torsional mode is not provided by classical theories. The Hierarchical Beam Theories show a good agreement with the FEM 3D solutions. For the flexural mode $\bar{\omega}$ converges already for $N = 3$, while an expansion order higher than 10 is required to have convergence also for the torsional mode for the case $m = 2$. The FEM 3D analysis carried out using a refined mesh gives results more accurate only in the case of $m = 2$, but the time needed to perform the computation increases noticeably. Deep beam are investigated in Tables 2.3

$\bar{\omega}$	$m = 1$		$m = 2$	
	Mode I, II	Mode III	Mode I, II	Mode III
	$\times 10^2$	$\times 1$	$\times 10$	$\times 1$
FEM 3D ^a	2.8487	1.7894	1.1389	3.5787
FEM 3D ^b	2.8487	1.7894	1.1391	3.5788
$N \geq 10$	2.8486	1.7894	1.1389	3.5787
$N = 8, 9$	2.8486	1.7894	1.1389	3.5788
$N = 6, 7$	2.8486	1.7899	1.1389	3.5798
$N = 4, 5$	2.8486	1.7904	1.1389	3.5808
$N = 3$	2.8486	1.9483	1.1389	3.8967
$N = 2$	2.8487	1.9483	1.1390	3.8967
$N = 1$	2.8487	1.9483	1.1390	3.8967
TB	2.8487	– ^c	1.1390	–
EB	2.8490	–	1.1395	–

a: mesh $80 \times 15 \times 15$ elements. *b*: mesh $50 \times 10 \times 10$ elements.
c: mode not provided by the theory.

Table 2.2. Dimensionless natural frequency, square cross-section, $l/a = 100$.

$\bar{\omega}$	$m = 1$		$m = 2$	
	Mode I, II	Mode III	Mode I, II	Mode III
	$\times 1$	$\times 10^{-1}$	$\times 10^{-1}$	$\times 10^{-1}$
FEM 3D ^a	2.8038	1.7893	1.0730	3.5786
FEM 3D ^b	2.8038	1.7894	1.0731	3.5786
$N = 12$	2.8039	1.7893	1.0730	3.5786
$N = 10, 11$	2.8039	1.7894	1.0730	3.5786
$N = 8, 9$	2.8039	1.7894	1.0730	3.5787
$N = 6, 7$	2.8039	1.7899	1.0730	3.5797
$N = 5$	2.8039	1.7904	1.0730	3.5807
$N = 4$	2.8039	1.7905	1.0731	3.5819
$N = 3$	2.8039	1.9483	1.0731	3.8967
$N = 2$	2.8086	1.9483	1.0796	3.8967
TB	2.8081	– ^c	1.0788	–
EB	2.8374	–	1.1213	–

a: mesh $40 \times 20 \times 20$ elements. *b*: mesh $20 \times 10 \times 10$ elements.
c: mode not provided by the theory.

Table 2.3. Dimensionless natural frequency, square cross-section, $l/a = 10$.

$\bar{\omega}$	$m = 1$		$m = 2$	
	Mode I, II $\times 10^{-1}$	Mode III $\times 10^{-1}$	Mode I, II $\times 10^{-1}$	Mode III $\times 10^{-1}$
FEM 3D ^a	1.0730	3.5786	3.7362	7.1563
FEM 3D ^b	1.0730	3.5786	3.7363	7.1565
N = ≥ 10	1.0730	3.5786	3.7362	7.1563
N = 8, 9	1.0730	3.5787	3.7362	7.1565
N = 7	1.0730	3.5797	3.7362	7.1586
N = 6	1.0730	3.5797	3.7362	7.1587
N = 5	1.0730	3.5807	3.7362	7.1611
N = 4	1.0731	3.5819	3.7369	7.1707
N = 3	1.0731	3.8967	3.7383	7.7933
N = 2	1.0796	3.8967	3.8024	7.7933
N = 1	1.0788	3.8967	3.7955	7.7933
TB	1.0788	– ^c	3.7955	–
EB	1.1213	–	4.2848	–

a: mesh $40 \times 20 \times 20$ elements. *b*: mesh $20 \times 10 \times 10$ elements.
c: mode not provided by the theory.

Table 2.4. Dimensionless natural frequency, square cross-section, $l/a = 5$.

and 2.4. Table 2.3 shows results for $l/a = 10$. Classical theories provide acceptable results for the flexural modes, with a maximum error rate of 4.5% in the case $m = 2$. As seen for slender beams, the hierarchical beam theories addressed before provide good agreement with results obtained via the FEM 3D analysis, even for the torsional mode. Table 2.4 is referred to $l/a = 5$. As expected the frequencies predicted by the proposed hierarchical beam theories are smaller than those predicted by the classical beam theories. In fact, as known from mechanical vibrations, natural frequencies decrease as the stiffness of a structure decreases. Furthermore, the difference between the frequencies of classical theories and the hierarchical beam theories decreases as the value of l/a increases, with respect of the flexural mode. Then it can be notice that the classical theories can be accepted only for slender beams. The natural frequencies increase when the value of l/a is reduced, by virtue of the fact that the longer beam is less rigid. Moreover the natural frequencies increase as the half-wave number m along the beam axis increases.

2.7.2 Box Cross-Section

A beam with a box cross-section is considered, as shown in Fig. 2.1. The half-wave number m is assumed equal to one. Several modes have been identified. Different behaviors between slender and deep beams can be observed. Table 2.5 presents the natural dimensionless frequency in the case of $l/a = 100$. Since the cross-section of the beam is symmetric two flexural modes are present, indicated as Mode I, II. Torsion is addressed as

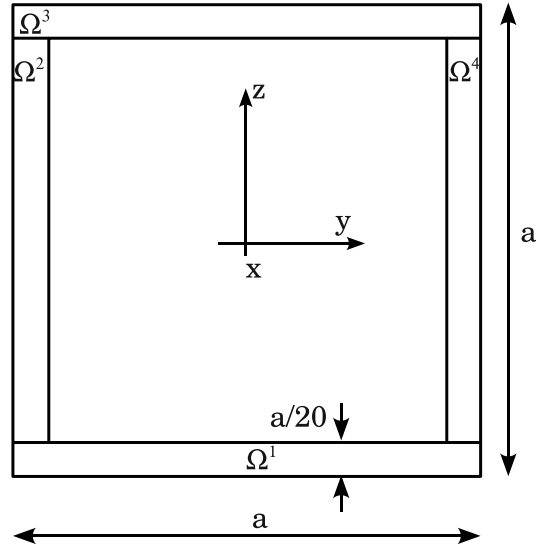


Figure 2.1. Box-beam cross-section geometry.

Mode III. Modes I and II lay on planes rotated by $\pm 45^\circ$ respect to the cross-section axes. Two three-dimensional FEM solutions are provided, in order to present a convergence analysis. For the flexural modes the hierarchical beam theories match the FEM solution

	Mode I, II	Mode III
$\bar{\omega}$	$\times 10^2$	$\times 1$
FEM 3D ^a	3.8311	1.7067
FEM 3D ^b	3.8311	1.7078
N = 14	3.8313	1.7214
N = 12	3.8313	1.7229
N = 10	3.8313	1.7311
N = 8	3.8313	1.7326
N = 6	3.8314	1.7387
N = 4	3.8315	1.7703
N = 2	3.8321	1.9483
TB	3.8321	- ^c
EB	3.8328	-

a: mesh $200 \times 40 \times 40$ elements.

b: mesh $100 \times 20 \times 20$ elements.

c: mode not provided by the theory.

Table 2.5. Dimensionless natural frequency, box cross-section, $l/a = 100$.

with an expansion order as low as 4. The natural frequency related to the torsional mode

	Mode I,II	Mode III	Mode IV	Mode V
$\bar{\omega}$	$\times 1$	$\times 10^{-1}$	$\times 10^{-1}$	$\times 10^{-1}$
FEM 3D ^a	3.6483	1.0028	1.6585	1.6980
FEM 3D ^b	3.6488	1.0139	1.6594	1.6991
N = 15	3.6544	1.1399	1.6625	1.7133
N = 13	3.6560	1.2463	1.6666	1.7150
N = 11	3.6583	1.2546	1.6700	1.7239
N = 9	3.6616	1.5908	1.6921	1.7260
N = 7	3.6672	2.1342	1.7067	1.7361
N = 6	3.6708	- ^c	2.1612	1.7385
N = 5	3.6720	-	2.3703	1.7702
N = 4	3.6823	-	-	1.7705
N = 2	3.7362	-	-	1.9483
TB	3.7353	-	-	-
EB	3.8048	-	-	-

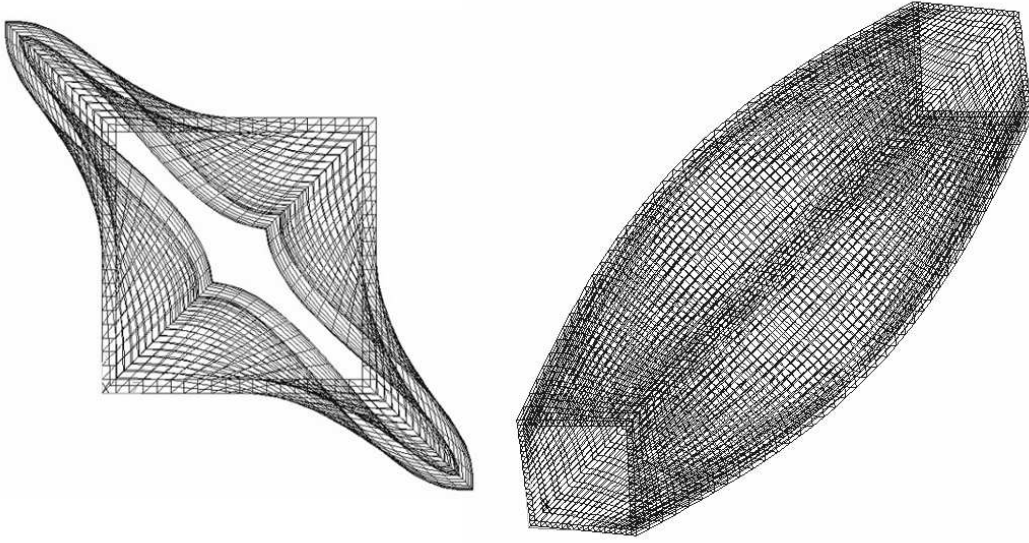
a: mesh $80 \times 40 \times 40$ elements.

b: mesh $40 \times 20 \times 20$ elements.

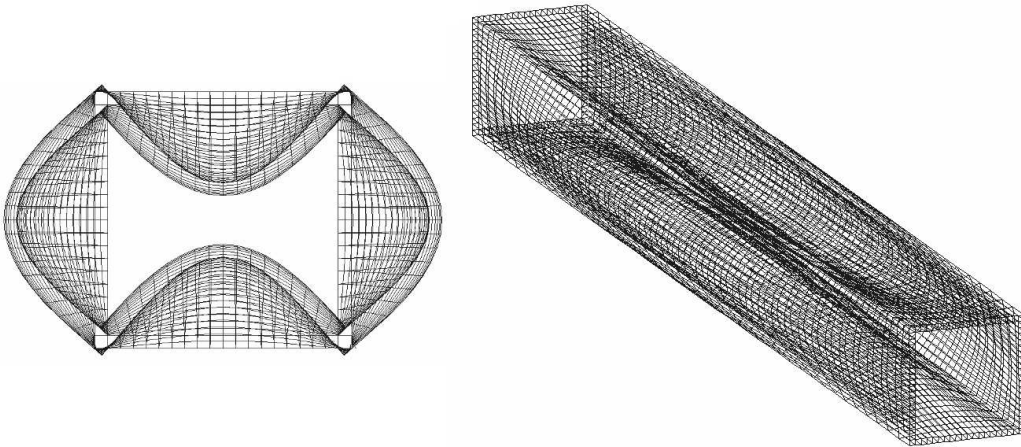
c: mode not provided by the theory.

Table 2.6. Dimensionless natural frequency, box cross-section, $l/a = 10$.

converges more slowly and a higher order of expansion is required in order to minimize the error, which is less than 1% for $N = 14$. Classical theories yield good results for the flexural modes, differing the values from the FEM solution only in the fourth significant digit. Torsional mode is not provided by classical theories. The case $l/a = 10$ is presented in Table 2.6, where values for the first five dimensionless natural frequencies are presented. Modes I and II refer also in this case to symmetric flexural modes rotated by $\pm 45^\circ$. Mode III is a shear mode on plane yz , as shown in Fig. 2.2. Fig. 2.3 shows Mode IV, characterised by bending on different sense for two contiguous sides of the cross-section. Mode V correspond to torsion. The highest expansion order is required for modes III, IV and V in order to achieve a good convergence with the FEM solution. However, the shear mode differs from the FEM solution by about 14% even when $N = 15$. This problem could be solved by using a local approach. It should be noted that for low expansion orders not all the modal shapes are obtained. In particular, for Mode III an expansion order equal to seven is necessary. This explains the error rate observed before. Higher modes are not provided by medium-low order theories, then higher values of N are required to match the FEM results. Classical theories are not suitable when $l/a = 10$ because only the two flexural modes are provided. The corresponding values of the frequencies are in accordance with the FEM solution, being the error about 4%. Table 2.7 presents the dimensionless natural frequencies for a deep beam ($l/a = 5$). The first eight values of $\bar{\omega}$

Figure 2.2. Box beam, Mode III, $l/a = 10$.

are reported. Modes I and II refer to the $\pm 45^\circ$ bending seen before. Modes III and IV observed in the previous analysis are also present. Other three modes (VI, VII and VIII) after the torsional one (Mode V) are present. Modes VI and VII are characterised by the same value of $\bar{\omega}$ (see Fig. 2.4). Mode VIII is presented in Fig. 2.5. It is confirmed that, for a deep beam, the maximum expansion order is necessary in order to achieve a good

Figure 2.3. Box beam, Mode IV, $l/a = 10$.

	Mode I, II	Mode III	Mode IV	Mode V	Mode VI, VII	Mode VIII
$\bar{\omega}$	$\times 10^{-1}$	$\times 10^{-1}$	$\times 10^{-1}$	$\times 10^{-1}$	$\times 10^{-1}$	$\times 10^{-1}$
FEM 3D ^a	1.2487	1.3043	1.7032	3.3320	3.4390	3.8525
FEM 3D ^b	1.2503	1.3123	1.7044	3.3348	3.4630	3.9189
N = 15	1.2673	1.4065	1.7152	3.3669	3.7586	4.7429
N = 13	1.2727	1.4914	1.7302	3.3716	3.8908	4.8897
N = 11	1.2798	1.4983	1.7333	3.3956	4.1046	5.7512
N = 9	1.2898	1.7844	1.8052	3.4038	4.4573	5.8295
N = 8	1.2952	2.2817	1.8075	3.4349	4.5126	- ^c
N = 7	1.3080	2.2829	1.8443	3.4558	-	-
N = 5	1.3189	5.1352	2.9848	3.5393	-	-
N = 4	1.3309	-	-	3.5422	-	-
N = 2	1.3969	-	-	3.8967	-	-
TB	1.3957	-	-	-	-	-
EB	1.4894	-	-	-	-	-

a: mesh $80 \times 40 \times 40$ elements.

b: mesh $40 \times 20 \times 20$ elements.

c: mode not provided by the theory.

Table 2.7. Dimensionless natural frequency, box cross-section, $l/a = 5$.

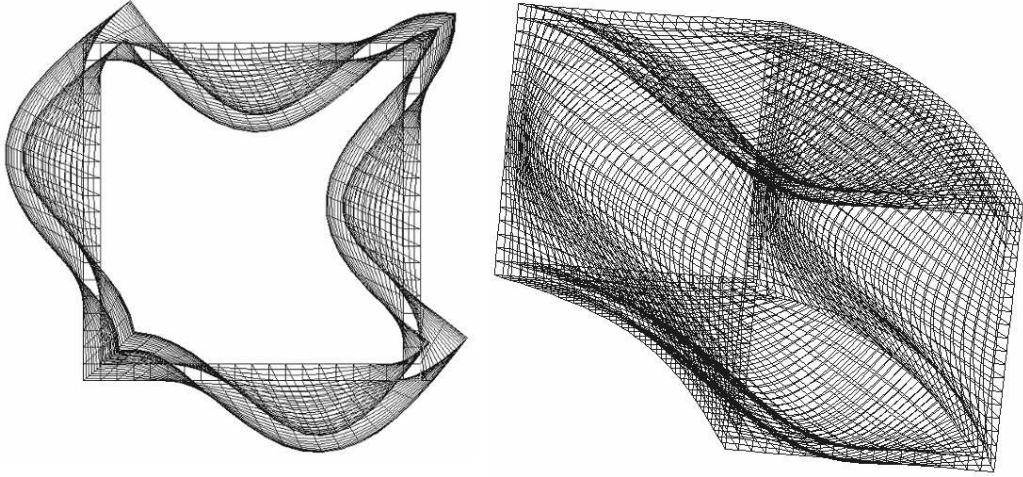


Figure 2.4. Box beam, Mode VI and VII, $l/a = 5$.

agreement with the FEM solution. The maximum error, about 20%, is found for Mode VIII. This modal shape is provided only for high expansion orders ($N \geq 9$). The modes

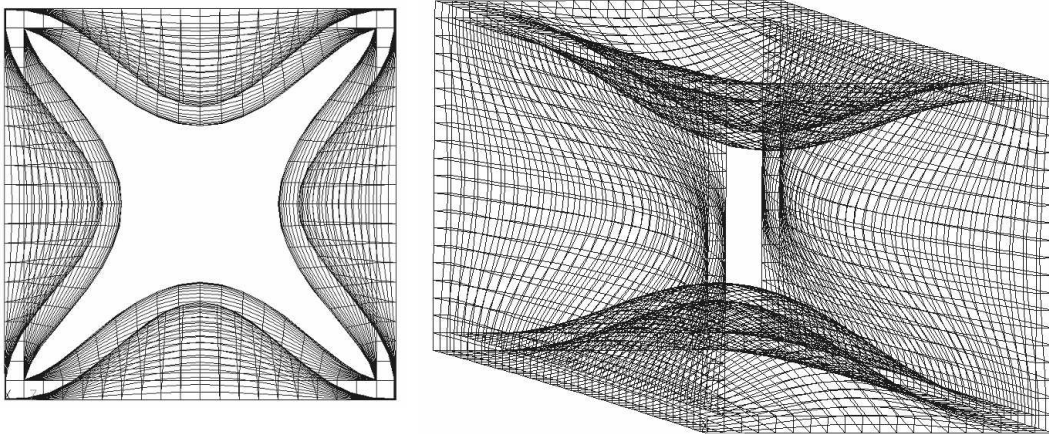


Figure 2.5. Box beam, Mode VIII, $l/a = 5$.

that are provided already from $N = 2$ are the flexural modes (I and II) and the torsion (V). The others modal shapes are detected at higher N . For instance, $N = 5$ is necessary to identify modes III and IV, whereas $N = 8$ is the minimum expansion order that yields Modes VI and VII. Classical theories are not applicable because only two modes (I, II) are provided.

2.7.3 I Cross-Section

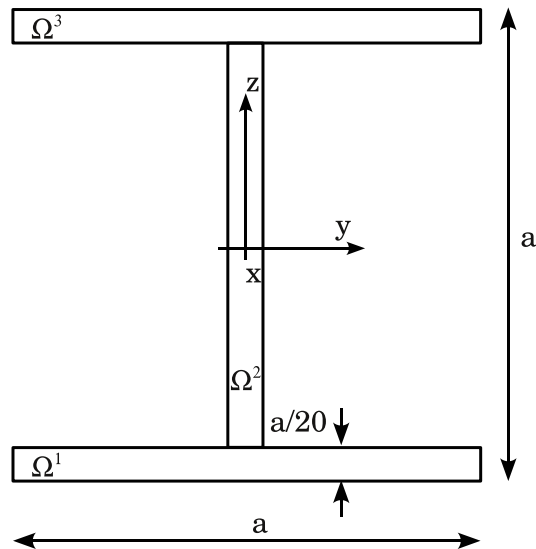


Figure 2.6. I-shaped cross-section geometry.

A beam with I-shaped cross-section is investigated (see Fig. 2.6).

Table 2.8 presents the first three dimensionless natural frequency for a slender beam ($l/a = 100$), considering a half-wave number $m = 1$ and $m = 2$. It is possible to identify a

$\bar{\omega}$	$m = 1$			$m = 2$		
	Mode I	Mode II	Mode III	Mode I	Mode II	Mode III
	$\times 10^2$	$\times 10^2$	$\times 10$	$\times 10^2$	$\times 10$	$\times 10$
FEM 3D ^a	2.3671	4.1451	1.1915	9.4639	1.6538	2.5143
FEM 3D ^b	2.3671	4.1451	1.1934	9.4646	1.6539	2.5178
N = 15	2.3670	4.1452	1.3134	9.4641	1.6540	2.7446
N = 12	2.3671	4.1453	1.3780	9.4642	1.6540	2.8680
N = 10	2.3671	4.1453	1.4725	9.4643	1.6541	3.0491
N = 8	2.3671	4.1454	1.8149	9.4644	1.6542	3.7122
N = 7	2.3671	4.1454	3.1243	9.4644	1.6542	6.2883
N = 4	2.3671	4.1458	3.3051	9.4653	1.6548	6.6508
N = 3	2.3671	4.1458	16.774	9.4653	1.6548	33.548
N = 2	2.3672	4.1474	16.774	9.4658	1.6574	33.550
TB	2.3671	4.1474	- ^c	9.4657	1.6574	-
EB	2.3673	4.1483	-	9.4641	1.6540	-

a: mesh $200 \times 40 \times 40$ elements.

b: mesh $100 \times 20 \times 40$ elements.

c: mode not provided by the theory.

Table 2.8. Dimensionless natural frequency, I-shaped cross-section, $l/a = 100$.

flexural mode on the xy plane, bending on the xz plane, and a torsional mode. They are referred to in Table as Mode I, II and III, respectively. Fifteenth-order model matches the FEM solution except for the torsional mode, where the error is around 10%. This value is however acceptable if compared with lower-order theory such as seventh-order, where the error overcomes 150%. Classical theories do not provide Mode III. Modes I agrees with FEM solution already for $N = 3$, in the case of $m = 1$.

Table 2.9 refers to a deep beam. Only the case $m = 1$ is reported. The first six values of the dimensionless natural frequency are presented. Mode I stands for a flexural mode on plane xy , whereas Mode III refers to a flexural mode on plane xz . Between these two modes is found the torsional mode (II). Higher modes, due to the fact that beams with thin-walled cross-sections present a ‘plate’ behaviour locally, are also found. Modes IV, V and VI are shown in Figs. 2.7, 2.8 and 2.9, respectively. An expansion order up to fifteen is used. Results match the FEM solution for the flexural modes and the torsional one. Local modes are found for higher expansion orders and at least $N = 11$ is required to detect mode VI. Mode IV and V appear from $N = 4$ and $N = 6$, respectively, but low expansion orders are not accurate. Table 2.10 refers to the case $l/a = 5$. Mode I and IV correspond to a flexural mode respect to the plane xy , with different symmetries of the

	Mode I	Mode II	Mode III	Mode IV	Mode V	Mode VI
FEM 3D ^a	2.3277	2.5626	3.8133	7.2068	13.179	21.843
FEM 3D ^b	2.3278	2.5633	3.8138	7.2230	13.263	21.957
N = 15	2.3292	2.6093	3.8275	7.6793	15.355	25.236
N = 13	2.3295	2.6382	3.8305	7.8576	16.135	26.179
N = 11	2.3301	2.6811	3.8355	8.1270	17.669	27.787
N = 10	2.3312	2.6812	3.8390	8.2092	19.696	- ^c
N = 7	2.3334	3.7276	3.8531	9.6172	23.787	-
N = 6	2.3360	3.7711	3.8648	10.661	70.623	-
N = 5	2.3372	3.9052	3.8653	21.908	-	-
N = 4	2.3415	3.9067	3.8856	24.367	-	-
N = 3	2.3416	16.780	3.8867	-	-	-
N = 2	2.3446	16.808	4.0262	-	-	-
TB	2.3436	-	4.0257	-	-	-
EB	2.3607	-	4.1129	-	-	-

a: mesh $80 \times 40 \times 40$ elements.

b: mesh $40 \times 20 \times 40$ elements.

c: mode not provided by the theory.

Table 2.9. Dimensionless natural frequency, I-shaped cross-section, $l/a = 10$.

fins, as shown in Figs. 2.10 and 2.11. Between these two modal shapes the torsional mode (II) and the flexural mode respect to the plane xz (Mode III, see Fig. 2.12) are found.

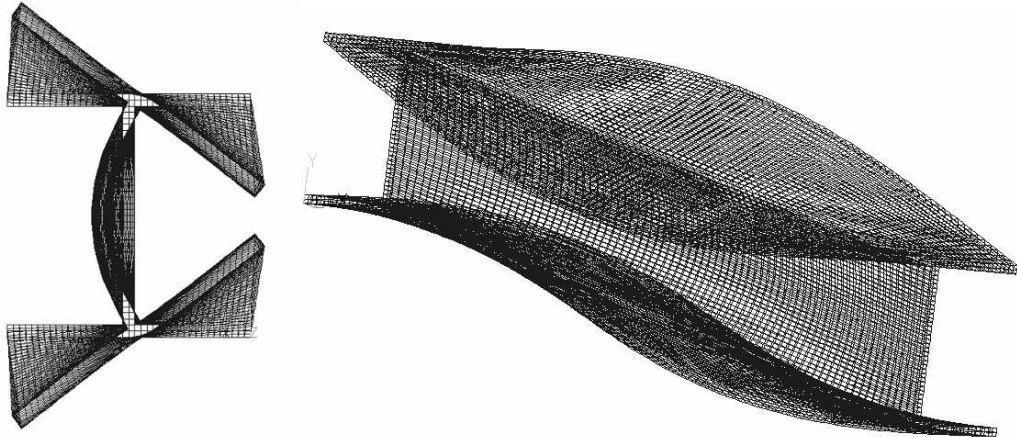


Figure 2.7. I-shaped cross-section beam, Mode IV, $l/a = 10$.

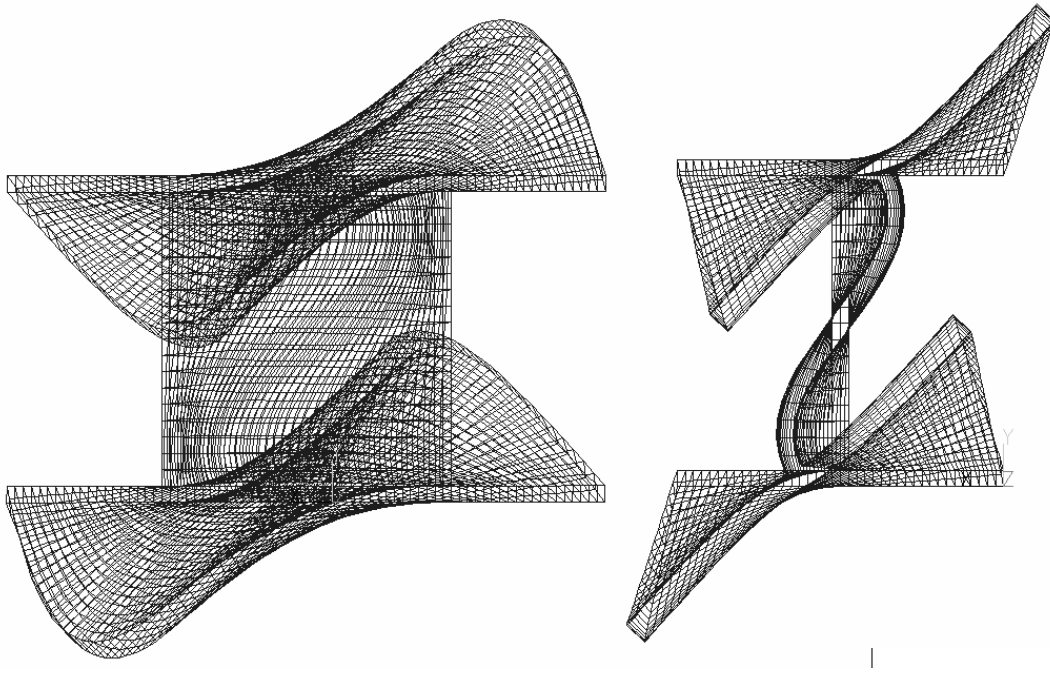


Figure 2.8. I-shaped cross-section beam, Mode V, $l/a = 10$.

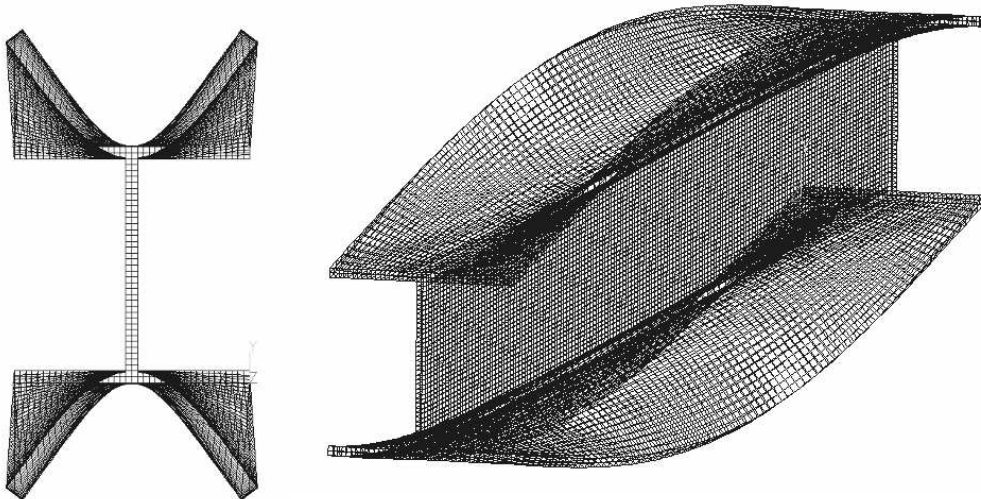


Figure 2.9. I-shaped cross-section beam, Mode VI, $l/a = 10$.

	Mode I	Mode II	Mode III	Mode IV	Mode V
FEM 3D ^a	7.5865	8.5485	9.3928	11.939	14.575
FEM 3D ^b	7.5977	8.5596	9.4017	11.952	14.646
N = 15	7.9297	8.7744	9.6487	12.308	16.514
N = 13	8.0482	8.8484	9.7658	12.393	17.245
N = 11	8.1934	8.9472	9.9520	12.531	18.705
N = 9	8.4642	9.1832	10.422	12.752	20.843
N = 7	8.7776	10.209	11.754	12.958	25.757
N = 6	8.9600	10.285	14.747	13.074	- ^c
N = 4	9.0737	10.447	32.061	13.322	-
N = 3	9.0792	33.599	-	13.362	-
N = 2	9.1235	33.812	-	14.903	-
TB	9.1098	-	-	14.897	-
EB	9.3635	-	-	16.043	-

a: mesh $80 \times 40 \times 40$ elements.

b: mesh $40 \times 20 \times 40$ elements.

c: mode not provided by the theory.

Table 2.10. Dimensionless natural frequency, I-shaped cross-section, $l/a = 5$.

The fifth frequency (Mode V) is associated with the higher mode shown in Fig. 2.13. The same considerations done for $l/a = 10$ are valid also in this case. Classical theories provide only modes I and IV.

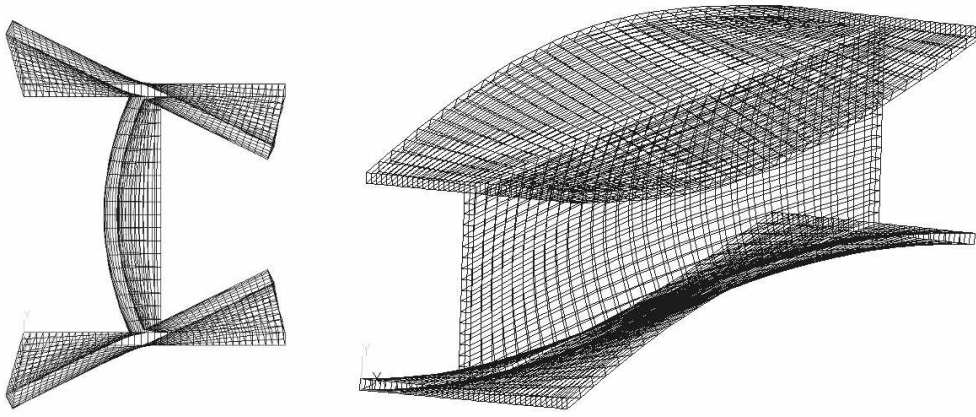


Figure 2.10. I-shaped cross-section beam, Mode I, $l/a = 5$.

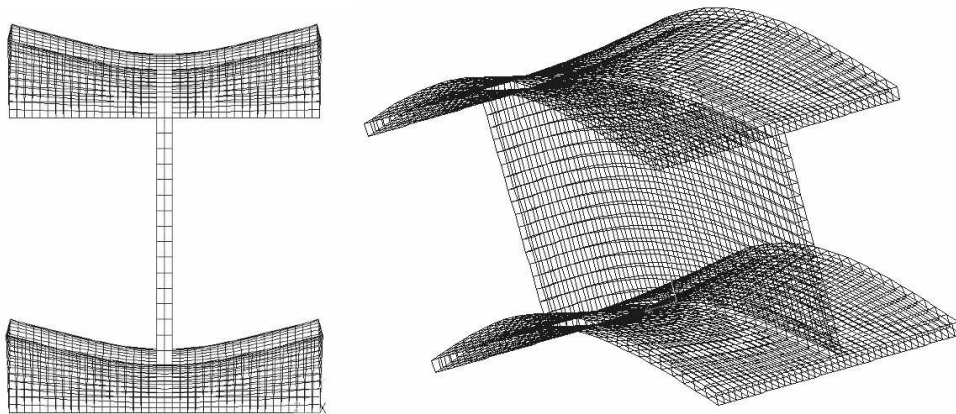


Figure 2.11. I-shaped cross-section beam, Mode IV, $l/a = 5$.

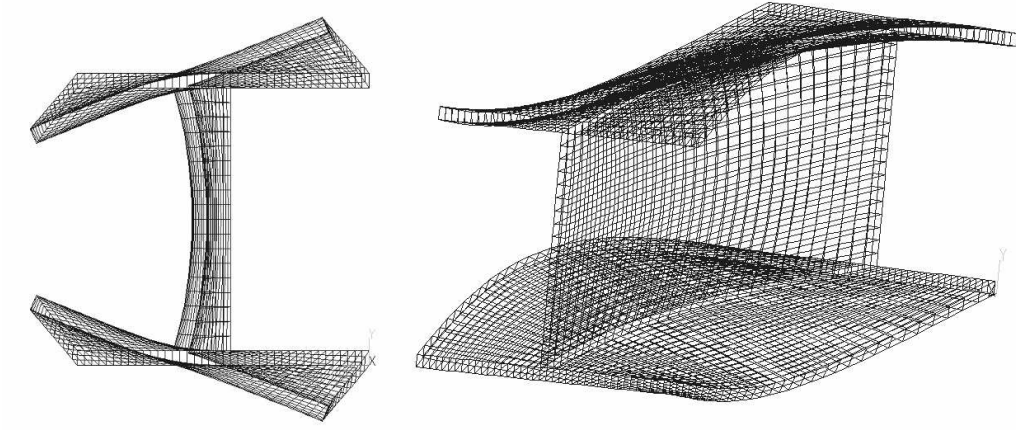


Figure 2.12. I-shaped cross-section beam, Mode III, $l/a = 5$.

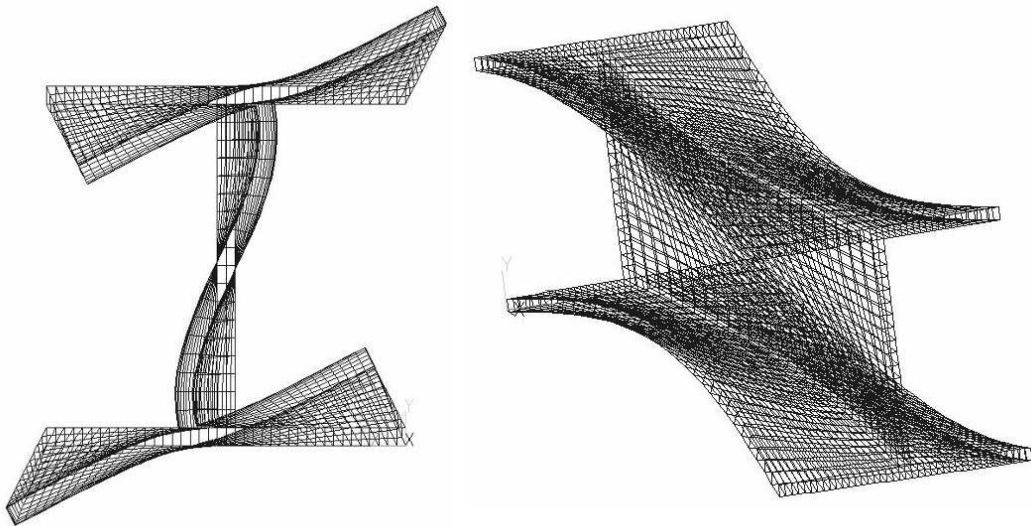


Figure 2.13. I-shaped cross-section beam, Mode V, $l/a = 5$.

2.7.4 C Cross-Section

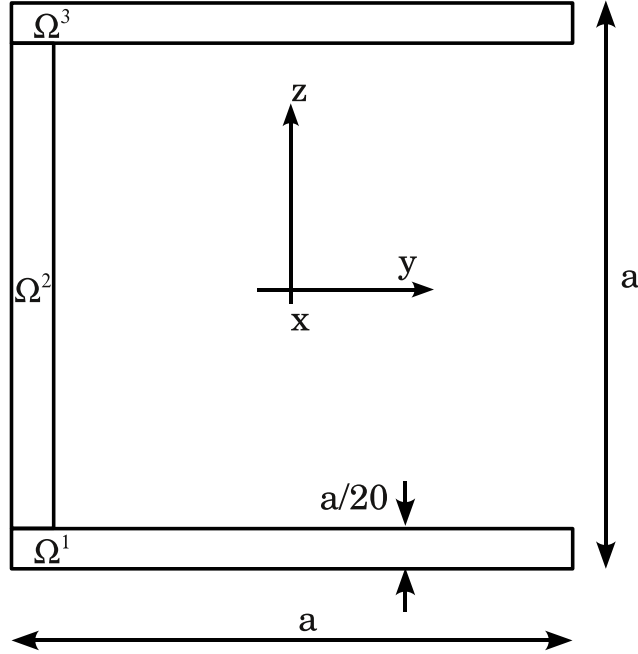


Figure 2.14. C-shaped cross-section geometry.

A free vibration analysis of slender and deep beams with C-shaped cross-section is carried out (see Fig. 2.14). For $l/a = 100$, Tab. 2.11, three modal shapes are present: two flexural modes on plane xy (Mode I) and xz (Mode II) and a torsional mode (III). For the first mode an expansion order $N = 4$ matches already the FEM solution. For modes II and III, a higher expansion order is required in order to match the FEM solution. $N = 14$ gives a relative error around 1% for the second flexural mode and around 3% for the torsional mode.

Up to seven values of $\bar{\omega}$ can be retrieved when $l/a = 10$, Tab. 2.12. Mode I corresponds to a bending on plane xz , whereas Mode II stand for a flexural mode on plane xy . In Fig. 2.15 the third modal shape is presented. The torsional mode is addressed as Mode IV. Other two modal shapes (V and VI) are found, related to a local behaviour of the beam’s faces. These are shown in Fig. 2.16 and 2.17, respectively. An expansion order up to $N = 6$ is necessary to identify them, whereas $N = 4$ provides Mode III only. Since the beam is deep a high expansion order is required, in particular when higher modes are taken into account. Figs. 2.18, 2.19 and 2.20 show the behaviour of $\bar{\omega}$ respect to N in the case of $l/a = 5$. Modes I, III and VI are found for $N \geq 5$ and correspond to a flexural mode on plane xz (see Fig. 2.21), a shear mode (see Fig. 2.22) and a local mode (see Fig. 2.23). Modes II, IV and V are found already for $N = 2$ and correspond to bending on plane xz (see Fig. 2.24), a bending on plane xy and to the torsional mode. Other two

	Mode I	Mode II	Mode III
$\bar{\omega}$	$\times 10^2$	$\times 10^2$	$\times 10$
FEM 3D ^a	3.2098	3.6048	1.2469
FEM 3D ^b	3.2098	3.6066	1.2485
N = 14	3.2098	3.6466	1.2857
N = 11	3.2098	3.6861	1.3286
N = 9	3.2098	3.7695	1.4421
N = 7	3.2098	3.9056	1.7488
N = 6	3.2098	4.0340	2.4709
N = 4	3.2098	4.1026	3.8367
N = 3	3.2099	4.1446	16.110
N = 2	3.2100	4.1474	18.860
TB	3.2101	4.1474	- ^c
EB	3.2105	4.1483	-

a: mesh $200 \times 40 \times 40$ elements.

b: mesh $100 \times 20 \times 20$ elements.

c: mode not provided by the theory.

Table 2.11. Dimensionless natural frequency, C-shaped cross-section, $l/a = 100$.

	Mode I	Mode II	Mode III	Mode IV	Mode V	Mode VI
FEM 3D ^a	1.4328	3.0814	3.4639	6.6624	7.7554	22.717
FEM 3D ^b	1.4339	3.0828	3.4813	6.6629	7.8192	22.741
N = 14	1.4500	3.0940	3.6994	6.6646	8.5880	22.869
N = 12	1.4577	3.0967	3.7704	6.6652	9.0209	22.924
N = 10	1.4866	3.1014	3.9789	6.6672	9.5124	23.077
N = 8	1.5163	3.1098	4.4073	6.6724	11.273	23.307
N = 6	1.8337	3.1150	5.2359	6.7889	15.947	28.907
N = 5	2.2074	3.1252	17.940	7.0154	- ^c	-
N = 4	2.3205	3.1273	22.289	7.1906	-	-
N = 3	3.7922	3.1326	-	16.320	-	-
N = 2	4.0234	3.1490	-	18.867	-	-
TB	4.0257	3.1524	-	-	-	-
EB	4.1129	3.1940	-	-	-	-

a: mesh $80 \times 40 \times 40$ elements.

b: mesh $40 \times 20 \times 20$ elements.

c: mode not provided by the theory.

Table 2.12. Dimensionless natural frequency, C-shaped cross-section, $l/a = 10$.

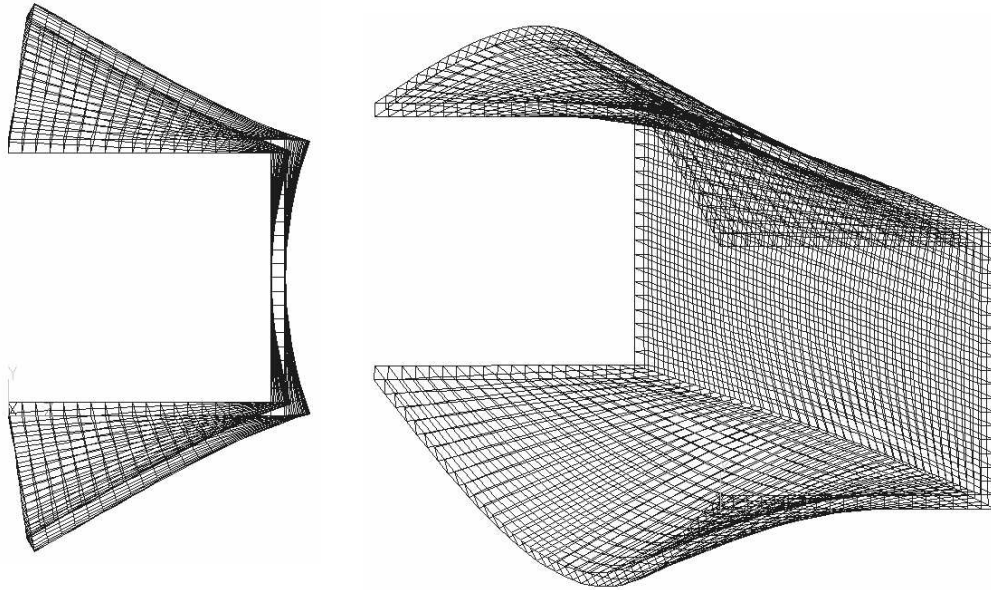


Figure 2.15. C-shaped cross-section beam, Mode III, $l/a = 10$.

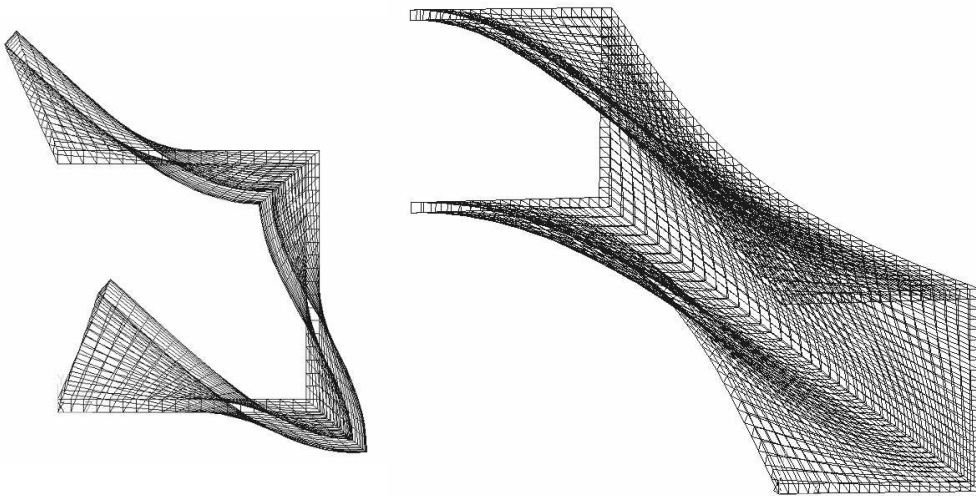


Figure 2.16. C-shaped cross-section beam, Mode V, $l/a = 10$.

higher modes are found when the expansion order is $N \geq 8$. These modes are shown in Figs. 2.25 and 2.26 and are indicated as Mode VII and VIII, respectively. All curves show a decreasing trend as the expansion order increase since the higher the number of degree

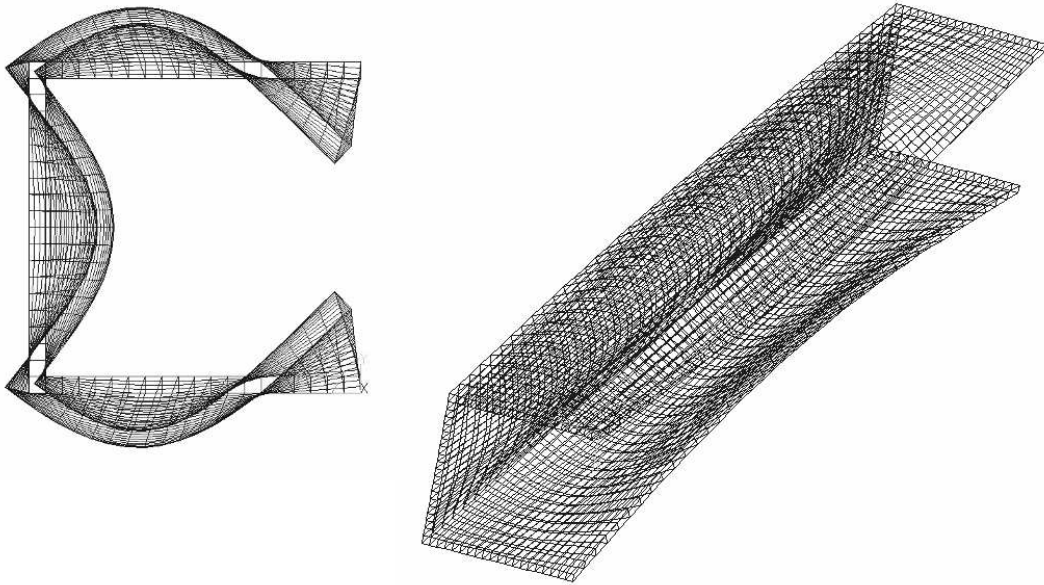


Figure 2.17. C-shaped cross-section beam, Mode VI, $l/a = 10$.

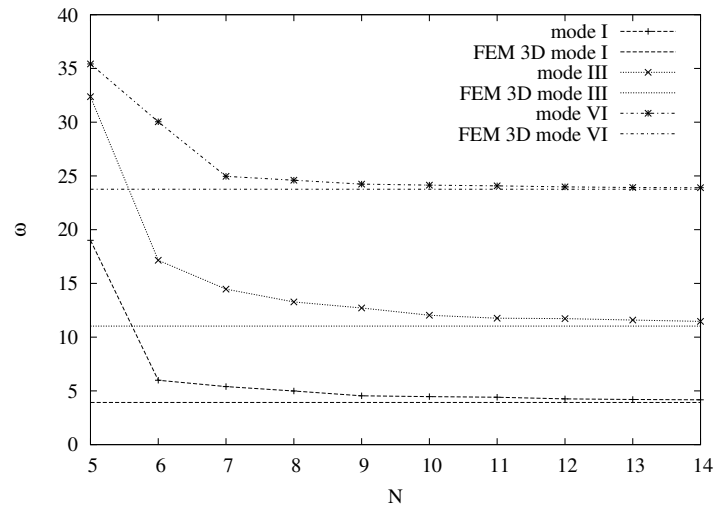


Figure 2.18. Frequency convergence versus N , Mode I, III and VI, C-shaped cross-section beam, $l/a = 5$.

of freedom in the model, the lower is the stiffness of the structure. Convergence depends on the considered mode. The maximum error respect to the FEM solution is achieved for mode VIII. The axial mode is not reported in the graphics since it is already outlined by lower expansion orders.

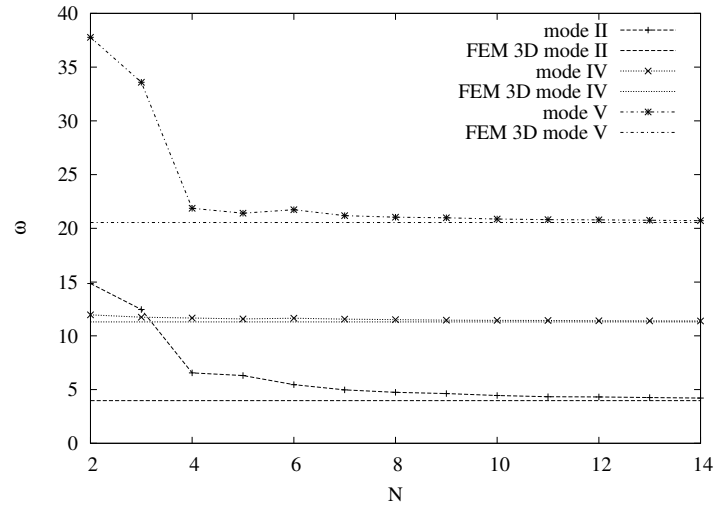


Figure 2.19. Frequency convergence versus N , Mode II, IV and V, C-shaped cross-section beam, $l/a = 5$.

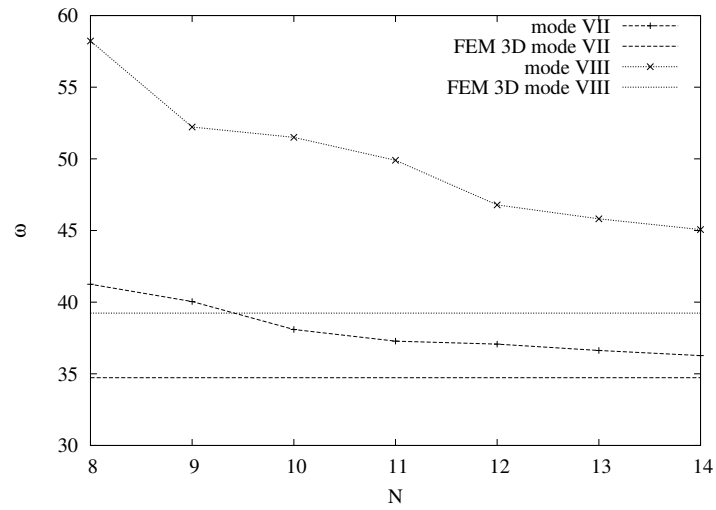


Figure 2.20. Frequency convergence versus N , Mode VII and VIII, C-shaped cross-section beam, $l/a = 5$.

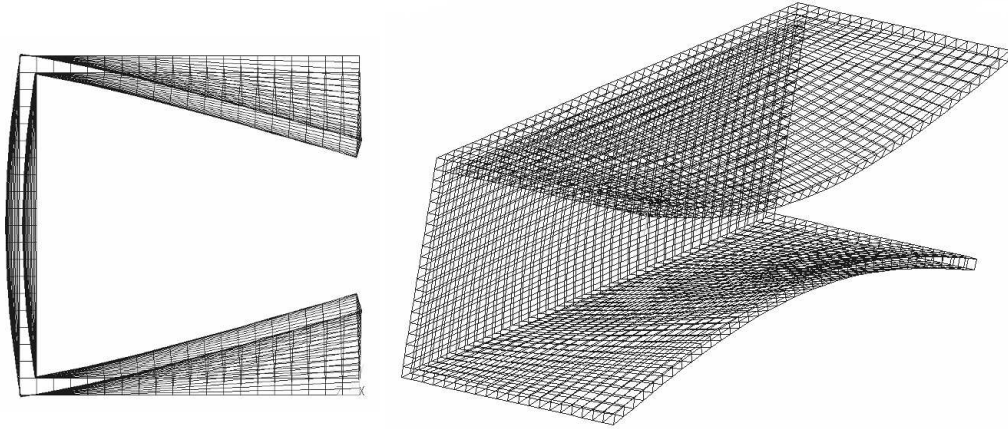


Figure 2.21. C-shaped cross-section beam, Mode I, $l/a = 5$.

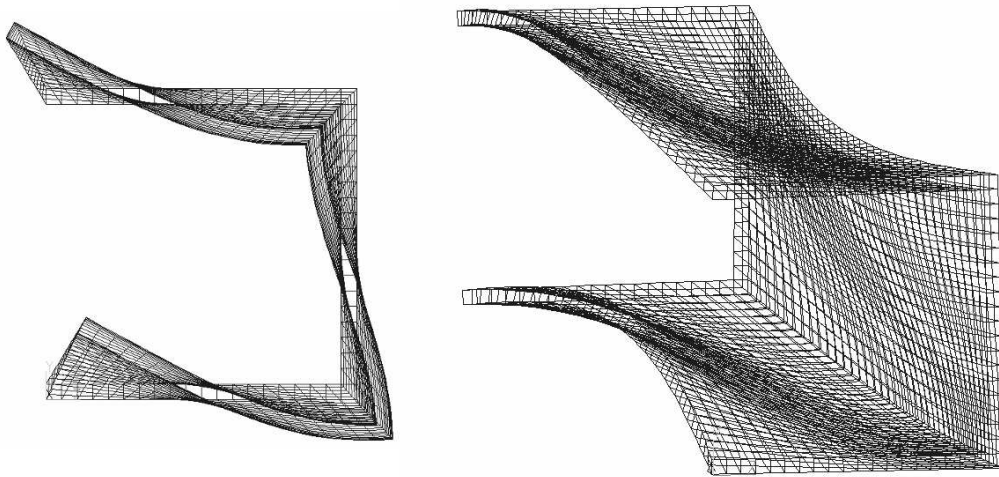


Figure 2.22. C-shaped cross-section beam, Mode III, $l/a = 5$.

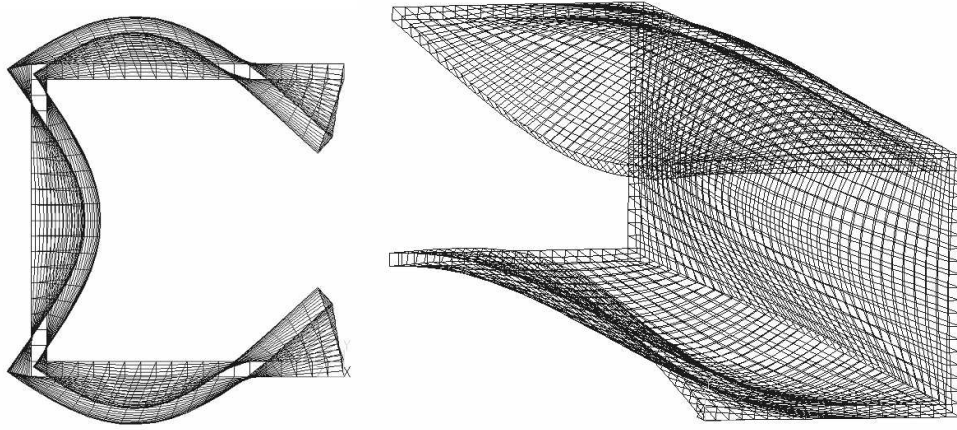


Figure 2.23. C-shaped cross-section beam, Mode VI, $l/a = 5$.

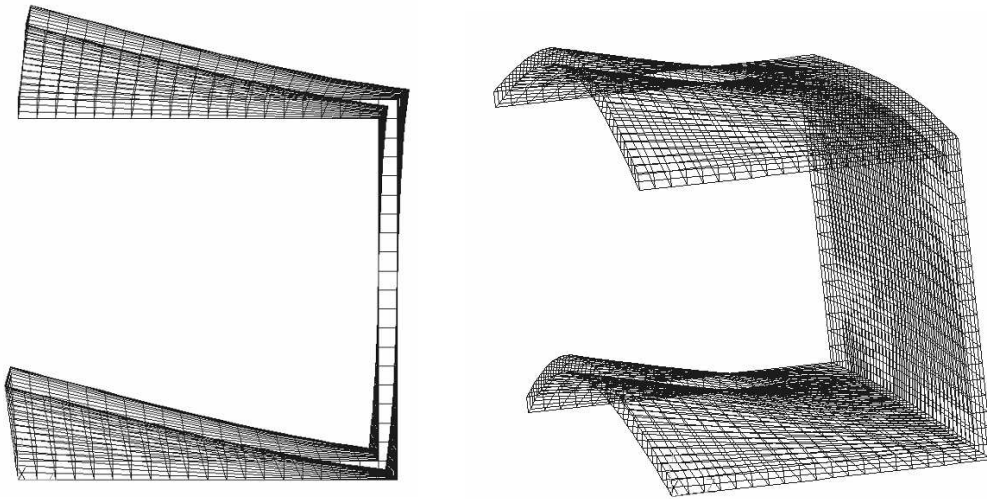


Figure 2.24. C-shaped cross-section beam, Mode II, $l/a = 5$.

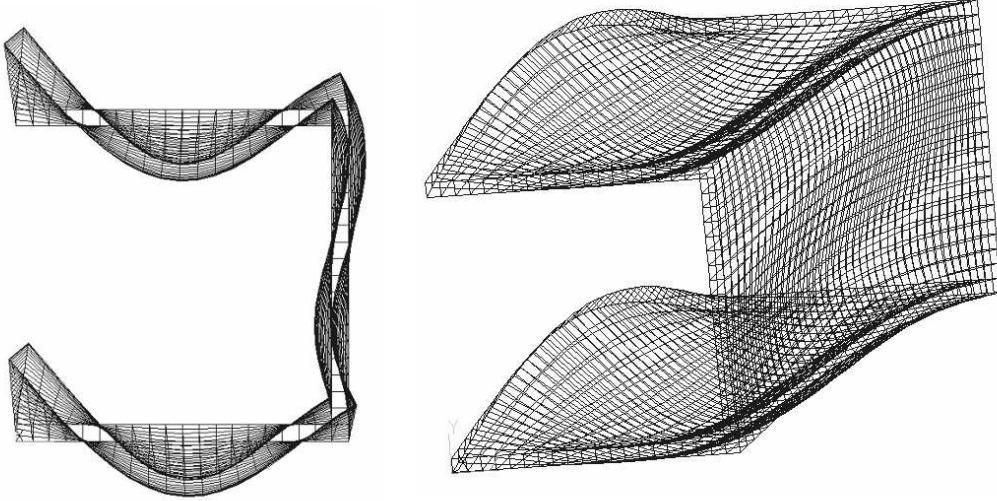


Figure 2.25. C-shaped cross-section beam, Mode VII, $l/a = 5$.

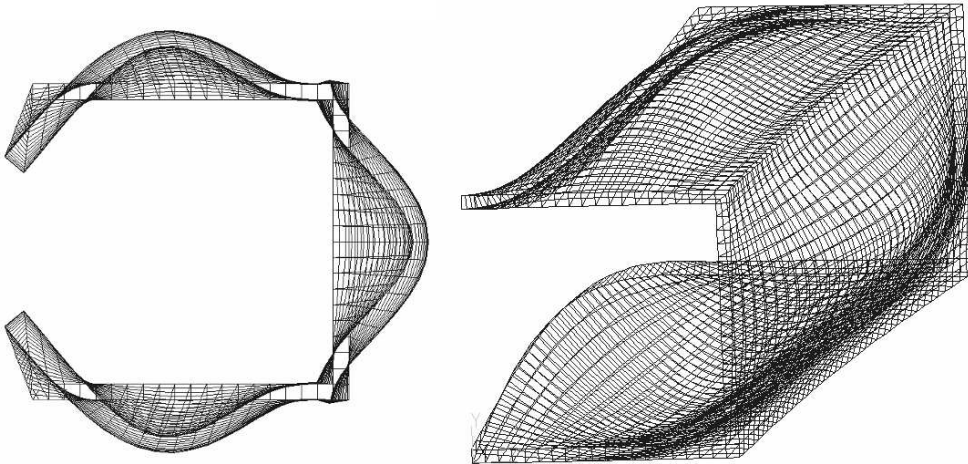


Figure 2.26. C-shaped cross-section beam, Mode VIII, $l/a = 5$.

2.8 Conclusions

A unified formulation (UF) has been proposed in the previous part and some application to the free vibration analysis of solid and thin-walled beam structures have been presented. Via this approach, higher-order models that account for shear deformations, in- and out-of-plane warping can be formulated straightforwardly. Classical models, such as Euler-Bernoulli's and Timoshenko's, are regarded as particular cases. A closed form, Navier-type solution has been addressed. Thin-walled beams with several cross-sections (box, I-shaped and C-shaped) have been investigated. Three-dimensional FEM solutions obtained via the commercial code ANSYS® have been considered as reference solutions. On the basis of the presented results, the following conclusions can be drawn:

- the proposed formulation allows obtaining results as accurate as desired through an appropriate choice of the approximation order. Results of one-dimensional CUF models match the three-dimensional FEM solution.
- The description of warping does not require any specific warping-function within CUF. It derives from the formulation itself.
- No local reference coordinates for the cross-section have to be defined.
- Classical models are not applicable, except for flexural modes of slender beams.
- Mechanics due to torsional modes as well as local modes is more difficult to describe accurately. Higher approximation order than for the flexural modes are required.
- The efficiency of the models is very high since the computational cost is few seconds for the highest order model considered, whereas the three-dimensional finite element models require about 10 minutes.

Chapter 3

Functionally Graded Materials

3.1 Introduction

Functionally graded materials (FGM) are a particular kind of composite materials, characterised by the continuous variation of the properties of their components, in order to accomplish specific functions. The mechanical and thermal response of materials with spacial gradients in composition and micro-structure is nowadays of considerable interest in several technological fields. The use of structures made from functionally graded materials is increasing because a smooth variation of material properties along some preferred direction, provides continuous stress distribution in the FGM structures. An overview on functionally graded materials, fabrication processes, area of application and some recent research studies is presented in the work of Mahamood et al. [69]. FGM structures can be studied assuming that the material properties, such as Young's modulus, poisson ratio and density, vary through the directions of the structures according to several gradation laws.

3.2 FGMs Laws

In literature we find various gradation laws, proposed to study structures made of FGM, whose parameters may be varied to obtain different distributions of the component materials through the dimensions of the structure. One of the most exploited gradation laws was adopted by Praveen and Reddy [88] and is based on a power law distribution. For plates it reads:

$$P(z) = (P_c - P_m) \left(\frac{2z + h}{2h} \right)^n + P_m \quad (3.1)$$

z is the thickness coordinate and h is the total thickness of the plate. P stands for the generic material property, subscripts c and m refer to the ceramic component and the metallic component, respectively. n is the volume fraction exponent ($n \geq 0$). When n is equal to 0 we have a fully ceramic plate. The above power law assumption reflects a simple rule of mixtures that allows to obtain the effective properties of a ceramic-metal plate. The previous power law distribution is found also in several works [44, 64, 83, 108, 126,

9, 33, 63, 57, 54, 71]. Qian et al [96] and Ganapathi [49] evaluated the effective material moduli by using the Mori-Tanaka homogenization technique [75].

$$\begin{aligned} \frac{K - K_m}{K_c - K_m} &= V_c \left/ \left[1 + (1 - V_c) \frac{3(K_c - K_m)}{3K_m + 4G_m} \right] \right. \\ \frac{G - G_m}{G_c - G_m} &= V_c \left/ \left[1 + (1 - V_c) \frac{(G_c - G_m)}{G_m + f_1} \right] \right. \\ f_1 &= \frac{G_m(9K_m + 8G_m)}{6(K_m + 2G_m)} \end{aligned} \quad (3.2)$$

K and G are the bulk modulus and the shear modulus, whereas V is volume-fraction of phase material. It should be mentioned that in [33], an exponential gradation law is also applied:

$$P(z) = (P_m \exp(-\delta(1 - 2z/h))), \delta = \frac{1}{2} \log \left(\frac{P_m}{P_c} \right) \quad (3.3)$$

3.3 Free vibration analysis of Functionally Graded Beams: Overview

Free Vibration and modal analysis of beams represents an interesting and important research topic. A brief overview of recent works about the free vibration of functionally graded beams is reported below. Fundamental frequency analysis of functionally graded (FG) beams with several boundary conditions have been carried out by Simsek [110] using classical, first order and various higher order shear deformation beam theories. Kapuria et al. [58] validated through experiments the static and free vibration response of layered functionally graded beams. A third order zigzag theory based model in conjunction with the modified rule of mixtures (MROM) for effective modulus of elasticity has been considered. Timoshenko beam theory is adopted by Xiang and Yang [128] for the study of free and forced vibration of laminated functionally graded beam of variable thickness under thermally induced initial stresses. Aydogdu and Taskin [8] investigated free vibration of simply supported FG beam by different higher order shear deformation and classical beam theories. Young's modulus of beam varies in the thickness direction according to power and exponential law. Static and dynamic behaviour of functionally graded Timoshenko and Euler-Bernoulli beams is investigated by Li [63] adopting a unified approach. [111] A new first-order shear deformation beam theory is used by Sina et al. [111] to analyse free vibration of functionally graded beams. The equations of motion are derived using Hamilton's principle. Different boundary conditions are considered. FG beam properties are assumed to be according to a simple power law function of the volume fractions of the beam material constituents. The free vibration analysis of FG beams is investigated using numerical finite element method in the work of Alshorbagy et al. [2]. Material gradation in axially and transversally through the thickness based on a power law is considered. The system of equations of motion is derived by using the principle of virtual work under the assumptions of the Euler-Bernoulli beam theory. Mur an et al. [77] consider linear beam theory to establishing the equilibrium and kinematic equations of

multi-layered FGM sandwich beams. The shear force deformation effect and the effect of consistent mass distribution and mass inertia moment have been taken into account. Numerical experiments were performed to calculate the eigenfrequencies and corresponding eigenmodes. The solution results are compared with those obtained using a commercial finite element model (FEM) code. A free vibration analysis of FGM beams via hierarchical models is presented in the following. The Unified Formulation (UF) that has been previously presented (Chapter 2) is extended to functionally graded beams. Material gradation is considered through a power law function of either one or two cross-section coordinates. The proposed models are validated through comparison with three-dimensional FEM solutions. Numerical results show that very accurate results can be obtained with small computational costs.

3.4 Constitutive equations for FG beams

In the case of isotropic FGMs, the matrices' coefficients \mathbf{C}_{pp} , \mathbf{C}_{pn} , \mathbf{C}_{np} and \mathbf{C}_{nn} of the constitutive equations (2.9) take into account the variation of the coefficients C_{ij} as follow:

$$\begin{aligned} C_{11} = C_{22} = C_{33} &= \frac{1 - \nu}{(1 + \nu)(1 - 2\nu)} E & C_{12} = C_{13} = C_{23} &= \frac{\nu}{(1 + \nu)(1 - 2\nu)} E \\ C_{44} = C_{55} = C_{66} &= \frac{1}{2(1 + \nu)} E \end{aligned} \quad (3.4)$$

being Young's modulus (E) and Poisson's ratio (ν) function of the position above the cross-section. The generic material property f is assumed to vary versus y or/and z coordinate according to a power law distribution:

$$f = (f_1 - f_2) (\alpha_y y + \beta_y)^{n_y} (\alpha_z z + \beta_z)^{n_z} + f_2 \quad (3.5)$$

This gradation law is obtained through the assumption of a power gradation law of the volume fraction of two constituent materials and the rule of mixtures, see Reddy [88] and Chakraborty et al. [33].

3.5 Numerical Results and Discussion

FGMs beams made of alumina and steel are considered. The mechanical properties of alumina are: $E_1 = 3.9 \cdot 10^5$ MPa, $\nu_1 = 0.25$, $\rho_1 = 3.96 \cdot 10^3$ kg/m³. In the case of steel, the following mechanical properties are used: $E_2 = 2.1 \cdot 10^5$ MPa, $\nu_2 = 0.31$, $\rho_2 = 7.80 \cdot 10^3$ kg/m³. E , ν and ρ vary along either y-axis or both y and z directions according to the power gradation law. Unless differently stated, a linear variation is considered in Eq. 3.5. Square cross-sections are considered. The sides of the cross-section are $a = b = 0.1$ m. The length-to-side ratio l/a is equal 100, ten and five. Slender and deep beams are, therefore, investigated. The half-wave number m in Eq. 2.34 is assumed equal to one. Flexural, torsional and axial free vibration modes are investigated. Natural frequencies are put into

the following dimensionless form:

$$\bar{\omega} = 10^2 \omega a \sqrt{\frac{\rho_2}{E_2}} \quad (3.6)$$

As far as validation is concerned, results (in terms of both natural frequencies and modes) are compared with three-dimensional FEM solutions obtained via the commercial code ANSYS[®], see ANSYS theory manual [5], Madenci and Guven [68] and Barbero [10]. The three-dimensional quadratic element “Solid95” is used. Each element is considered as homogeneous by referring to the material properties at its centre point. The accuracy of the three-dimensional FEM solution depends upon both the FEM numerical approximation and the approximation of the gradation law. In order to present the convergence of the three-dimensional reference solution, for each case three different meshes are considered. Acronym FEM 3D^a stand for a three-dimensional FEM model with 40 elements along the axial direction and 30 elements along y and z directions. Coarser solutions FEM 3D^b (30 × 20 × 20 elements) and FEM 3D^c (20 × 10 × 10 elements) are also considered. Although the three-dimensional FEM solution and the analytical one are different in nature, some considerations about computational time and effort can be addressed. For the reference FEM simulations, the computational time is as high as about two hour (refined mesh) and as low as about a minute (coarsest mesh). In the case of the proposed analytical solutions, the computational time is less than a second regardless the considered approximation order.

3.5.1 Material gradation along a cross-section direction

In this first example, material properties are supposed to vary along the y-axis only. Tables 3.1 to 3.3 present the dimensionless natural natural frequencies for $l/a = 100$, ten and five. Mode I and II are two flexural modes on planes xz and xy, respectively. Mode III is a torsional mode and Mode IV is an axial one. Refined and coarsest three-dimensional solutions differ by less than about 0.1%. Increasing the number of degrees of freedom, the frequencies decrease since a less stiff model is considered. Considering five significant digits, the considered natural frequencies converge for an expansion order equal to eight in the case of slender beams and ten for $l/a \leq 10$. Convergence is determined by the torsional mode, higher-order terms are required to accurately describe the in-plane cross-section warping. Torsional natural frequencies computed via a second- and a third-order theory differ from the FEM 3D^a solution by about 9%. In the case of $N = 4$, the difference reduces to about 0.1%. Converged results differ from FEM 3D^a solution by the last significant digit only. Classical models account for a stiff cross-section in its plane and, therefore, no torsional mode is present. EB yields very accurate flexural natural frequencies in the case of slender beams, whereas they differ by about 4.5% from the FEM reference solution in the case of $l/a = 5$.

3.5.2 Material gradation along both cross-section directions

Changes in properties along both y and z directions are considered. Fig. 3.1 shows the

$\bar{\omega}$	Mode I ¹ $\times 10^2$	Mode II ² $\times 10^2$	Mode III ³ $\times 1$	Mode IV ⁴ $\times 1$
FEM 3D ^a	3.8627	3.9217	2.4860	4.3247
FEM 3D ^b	3.8635	3.9223	2.4860	4.3247
FEM 3D ^c	3.8665	3.9244	2.4858	4.3247
$N \geq 8$	3.8623	3.9214	2.4861	4.3247
$N = 6, 7$	3.8623	3.9214	2.4868	4.3247
$N = 5$	3.8623	3.9214	2.4876	4.3247
$N = 4$	3.8624	3.9214	2.4877	4.3247
$N = 3$	3.8624	3.9214	2.7011	4.3247
$N = 2$	3.8639	3.9235	2.7080	4.3247
TB	3.8622	3.9215	–	4.3239
EB	3.8626	3.9219	–	4.3248

1: Flexural mode on plane xz. 2: Flexural mode on plane xy.
3: Torsional mode. 4: axial mode.

Table 3.1. Dimensionless natural frequencies, $E(y)$, $\nu(y)$, $\rho(y)$, $l/a = 100$, $n_1 = 1$.

$\bar{\omega}$	Mode I ¹ $\times 1$	Mode II ² $\times 1$	Mode III ³ $\times 10^{-1}$	Mode IV ⁴ $\times 10^{-1}$
FEM 3D ^a	3.8027	3.8568	2.4872	4.3163
FEM 3D ^b	3.8029	3.8568	2.4872	4.3163
FEM 3D ^c	3.8038	3.8569	2.4870	4.3163
$N \geq 10$	3.8026	3.8568	2.4873	4.3163
$N = 8, 9$	3.8026	3.8568	2.4874	4.3163
$N = 6, 7$	3.8026	3.8568	2.4881	4.3163
$N = 5$	3.8026	3.8568	2.4889	4.3163
$N = 4$	3.8027	3.8569	2.4892	4.3163
$N = 3$	3.8027	3.8574	2.7023	4.3163
$N = 2$	3.8099	3.8656	2.7091	4.3174
TB	3.8076	3.8663	–	4.3203
EB	3.8455	3.9060	–	4.3271

1: Flexural mode on plane xz. 2: Flexural mode on plane xy.
3: Torsional mode. 4: axial mode.

Table 3.2. Dimensionless natural frequencies, $E(y)$, $\nu(y)$, $\rho(y)$, $l/a = 10$, $n_1 = 1$.

$\bar{\omega}$	Mode I ¹ $\times 10^{-1}$	Mode II ² $\times 10^{-1}$	Mode III ³ $\times 10^{-1}$	Mode IV ⁴ $\times 10^{-1}$
FEM 3D ^a	1.4563	1.4726	4.9822	8.5820
FEM 3D ^b	1.4563	1.4726	4.9822	8.5821
FEM 3D ^c	1.4566	1.4727	4.9816	8.5826
$N \geq 10$	1.4562	1.4725	4.9824	8.5819
$N = 8, 9$	1.4562	1.4725	4.9825	8.5819
$N = 7$	1.4562	1.4725	4.9839	8.5819
$N = 6$	1.4562	1.4725	4.9840	8.5819
$N = 5$	1.4562	1.4726	4.9856	8.5819
$N = 4$	1.4563	1.4726	4.9873	8.5819
$N = 3$	1.4564	1.4735	5.4117	8.5822
$N = 2$	1.4648	1.4827	5.4251	8.5912
TB	1.4633	1.4861	–	8.6192
EB	1.5179	1.5436	–	8.6680

1: Flexural mode on plane xz. 2: Flexural mode on plane xy.
 3: Torsional mode. 4: axial mode.

Table 3.3. Dimensionless natural frequencies, $E(y)$, $\nu(y)$, $\rho(y)$, $l/a = 5$, $n_1 = 1$.

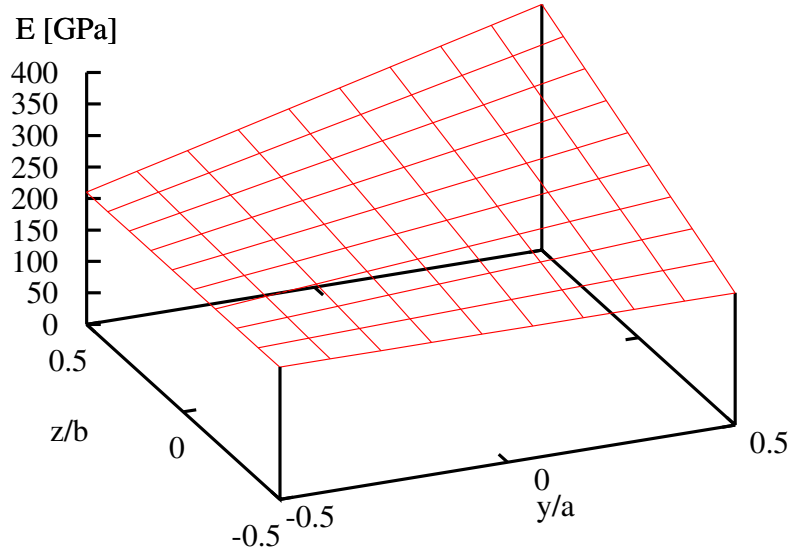


Figure 3.1. Material gradation law.

variation of the Young modulus. Due to the material gradation law, the cross-section is less stiff and heavier than the case of variation along one direction only. Lower natural frequencies are, therefore, expected. Results are presented in Tables 3.4 to 3.6 for slender up to deep beams. Due to the material gradation law, cross-section axes of symmetry y' and z' are identified by a anti clock wise rotation of $\pi/4$ around the positive direction of x -axis. Mode I and II are two flexural modes on planes xz' and xy' , respectively. Mode III is a torsional mode and Mode IV is an axial one. The same comments made in the case of Tables 3.1 to 3.3, are also valid in this case. Figures 3.2 and 3.3 show the effect of the power law exponents n_1 and n_2 on the modal frequencies seen before. The power law exponent plays an important role on the modal frequencies of the FGM beam. For seek of brevity only the case of gradation along both cross-section directions is reported, since a similar behaviour is found considering variation of the material along only a cross-section coordinate. For all the mode analysed is evident that an increase in the value of the power law exponent leads to a decrease in the values of the frequencies. The highest frequency values are obtained for a beam that is almost fully ceramic ($n_1 = n_2 = 0.1$), while the lowest frequency values are obtained for almost fully metallic beam ($n_1 = n_2 = 10$). This is due to the fact that an increase in the value of the power law exponent results in a decrease in the value of elasticity modulus and the value of bending rigidity.

$\bar{\omega}$	Mode I ¹ $\times 10^2$	Mode II ² $\times 10^2$	Mode III ³ $\times 1$	Mode IV ⁴ $\times 1$
FEM 3D ^a	3.2532	3.4149	2.1047	3.6968
FEM 3D ^b	3.2535	3.4155	2.1047	3.6968
FEM 3D ^c	3.2567	3.4165	2.1047	3.6968
$N \geq 8$	3.2520	3.4153	2.1048	3.6968
$N = 6, 7$	3.2520	3.4153	2.1054	3.6968
$N = 4, 5$	3.2520	3.4154	2.1061	3.6968
$N = 3$	3.2522	3.4155	2.2875	3.6968
$N = 2$	3.2526	3.4168	2.2906	3.6970
TB	3.2521	3.4153	–	3.6960
EB	3.2524	3.4157	–	3.6968

1: Flexural mode on plane xz' . 2: Flexural mode on plane xy' .
3: Torsional mode. 4: axial mode.

Table 3.4. Dimensionless natural frequencies, $E(y, z)$, $\nu(y, z)$, $\rho(y, z)$, $l/a = 100$, $n_1 = n_2 = 1$.

$\bar{\omega}$	Mode I ¹ $\times 1$	Mode II ² $\times 1$	Mode III ³ $\times 10^{-1}$	Mode IV ⁴ $\times 10^{-1}$
FEM 3D ^a	3.2021	3.3596	2.1053	3.6916
FEM 3D ^b	3.2024	3.3595	2.1053	3.6916
FEM 3D ^c	3.2039	3.3586	2.1052	3.6916
$N \geq 8$	3.2019	3.3597	2.1053	3.6916
$N = 6, 7$	3.2019	3.3597	2.1059	3.6916
$N = 5$	3.2019	3.3597	2.1066	3.6916
$N = 4$	3.2019	3.3598	2.1068	3.6916
$N = 3$	3.2023	3.3599	2.2880	3.6916
$N = 2$	3.2077	3.3667	2.2911	3.6924
TB	3.2072	3.3654	–	3.6944
EB	3.2386	3.4018	–	3.6978

1: Flexural mode on plane xz' . 2: Flexural mode on plane xy' .
3: Torsional mode. 4: axial mode.

Table 3.5. Dimensionless natural frequencies, $E(y, z)$, $\nu(y, z)$, $\rho(y, z)$, $l/a = 10$, $n_1 = n_2 = 1$.

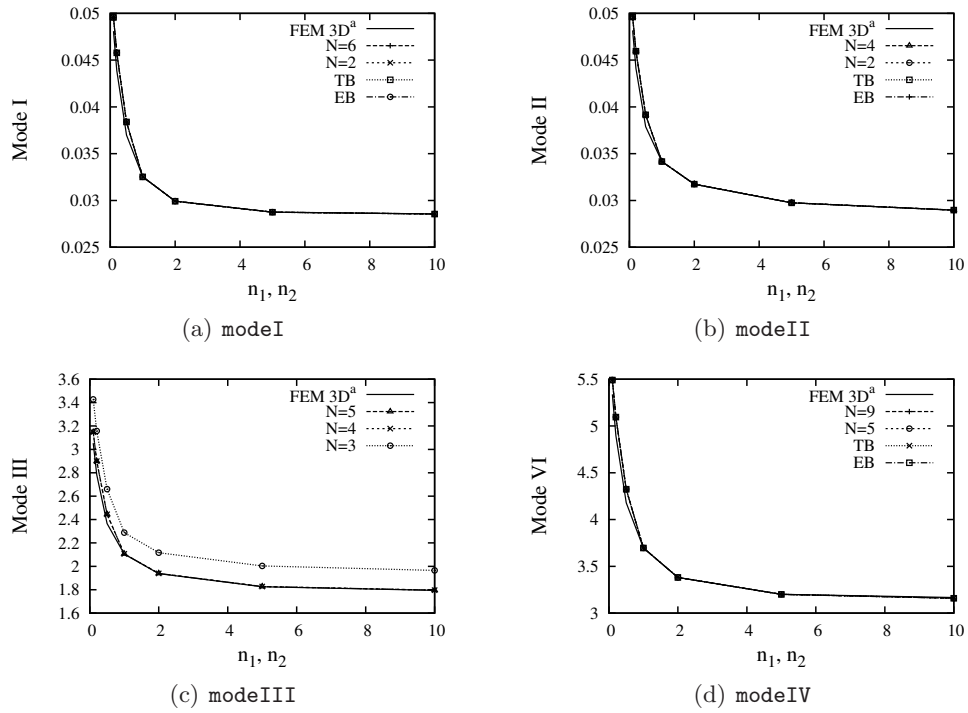


Figure 3.2. Variation of the modal frequencies with power law exponents n_1 and n_2 , $l/a = 100$, $E(y, z)$, $\nu(y, z)$, $\rho(y, z)$.

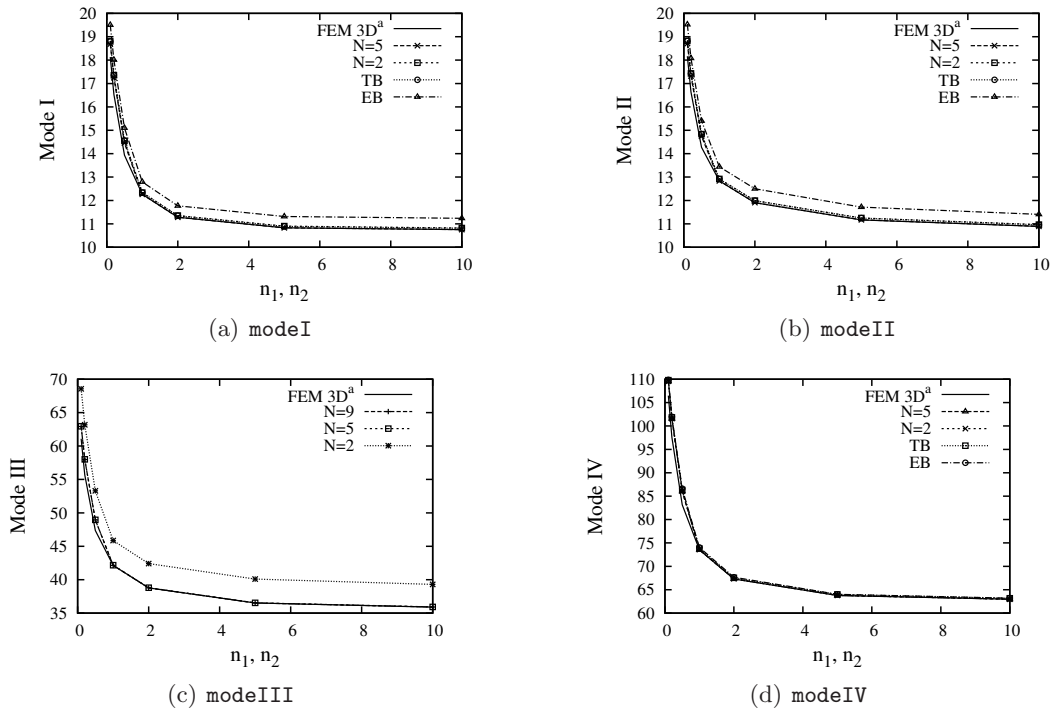


Figure 3.3. Variation of the modal frequencies with power law exponents n_1 and n_2 , $l/a = 5$, $E(y, z)$, $\nu(y, z)$, $\rho(y, z)$.

$\bar{\omega}$	Mode I ¹ $\times 10^{-1}$	Mode II ² $\times 10^{-1}$	Mode III ³ $\times 10^{-1}$	Mode IV ⁴ $\times 10^{-1}$
FEM 3D ^a	1.2263	1.2837	4.2135	7.3520
FEM 3D ^b	1.2264	1.2837	4.2135	7.3520
FEM 3D ^c	1.2269	1.2833	4.2135	7.3523
$N \geq 10$	1.2262	1.2838	4.2136	7.3519
$N = 8, 9$	1.2262	1.2838	4.2137	7.3519
$N = 6, 7$	1.2262	1.2838	4.2149	7.3519
$N = 5$	1.2262	1.2838	4.2163	7.3519
$N = 4$	1.2263	1.2839	4.2178	7.3520
$N = 3$	1.2267	1.2840	4.5790	7.3522
$N = 2$	1.2338	1.2920	4.5850	7.3571
TB	1.2338	1.2917	–	7.3792
EB	1.2791	1.3442	–	7.4018

1: Flexural mode on plane xz' . 2: Flexural mode on plane xy' .
 3: Torsional mode. 4: axial mode.

Table 3.6. Dimensionless natural frequencies, $E(y, z)$, $\nu(y, z)$, $\rho(y, z)$, $l/a = 5$, $n_1 = n_2 = 1$.

3.6 Conclusions

A unified formulation of one-dimensional beam models has been proposed for the free vibration analysis of functionally graded beams. Via this approach, higher order models that account for shear deformations, in- and out-of-plane warping can be formulated straightforwardly. Classical models, such as Euler-Bernoulli's and Timoshenko's, are regarded as particular cases. A closed form, Navier-type solution has been addressed. Material properties (Young's modulus, Poisson's ratio and density) have been supposed to vary above the cross-section according to a power gradation law. Flexural, torsional and axial frequencies and mode shapes have been investigated. Results have been validated through comparison with three-dimensional FEM solutions obtained via the commercial code ANSYS. On the basis of the presented results, it can be concluded that the proposed formulation allows obtaining results as accurate as desired through an appropriate choice of the approximation order, results of one-dimensional CUF models match the three-dimensional FEM solutions. The description of warping does not require any specific warping-function within the proposed formulation. It derives from the formulation itself. The efficiency of the proposed models is very high since the computational time is less than a second for the highest considered approximation order, whereas the three-dimensional FEM solution can require hours.

Chapter 4

Thermo-mechanical analysis of orthotropic and FG beams

4.1 Introduction

Many typical aeronautical and space structures concern beam-like structures that must operate in severe temperature environment. Hence the interest in detailed thermo-mechanical analyses that allow to understand the behaviour of beams subjected to various conditions of thermal loads. Furthermore, the materials with which these structures are made, must be capable of withstanding high temperatures. Functionally graded materials are high-temperature resistant materials, therefore, in the following, the thermal problem will be dealt by referring to these materials. In literature we find several works on the thermo-mechanical problem, dealing with isotropic, composite and fgm beams. Various application of the theory of thermoelasticity can be found in the book of Hetnarski and Eslami [52]. In particular, the thermal stress analysis of beams based on Euler-Bernoulli assumptions was presented. Beams made of functionally graded materials were also investigated. The thermo-elastic stress analysis of multilayered beams was carried out by Carpinteri and Poggi in [16]. Analytical solution were given under the Euler-Bernoulli hypotheses, when rigid interfaces between the layers were taken into account. Functionally graded materials were also investigated, considering a linear variation of material properties along the beam's thickness. A finite element semi-discretisation for composite beams was presented by Ghiringhelli [50]. The temperature distribution within the beam cross-section was computed by a two-dimensional finite element procedure. The structural thermo-elastic problem was discussed and comparison with three-dimensional finite element analysis were presented. Beams with variable thickness and subjected to thermo-mechanical loads were investigated in the work of Xu and Zhou [129]. The non-linear temperature profile along the beam's thickness was computed solving the heat conduction equation. Results were compared with those obtained from the commercial finite element software ANSYS. A three-noded thermomechanical beam finite element for the analysis of laminated beam was derived by Vidal and Polit [120]. Kapuria et al. [59] presented a higher order zigzag theory for thermal stress analysis of laminated beams under thermal loads. The thermal

field is approximated as piecewise linear across the thickness. The governing equations are derived using the principle of virtual work and Fourier series solutions are obtained for simply-supported beams. Tanigawa et al. [114] consider the transient thermal stress analysis of a laminated beam. The heat conduction problem is treated as one-dimensional in the thickness direction. The thermal stress distributions was obtained using the elementary beam theory and Airy's thermal stress function method. Sayman [107] studied the elasto-plastic thermal behavior of steel fiber-reinforced aluminium metal-matrix composite beams. Linear variation of the temperature is taken into account. The problem of thermal stresses in FGMs was addressed by Noda [82]. The optimal gradation profiles to decrease the thermal stresses in FGMs were discussed. The thermoelastic behaviour of functionally graded beams was also studied by Chakraborty et al. [33]. A beam finite element based on Timoshenko's theory was developed, accounting for an exponential and a power law through-the-thickness variation of elastic and thermal properties. A meshless method for thermo-elastic analysis of functionally graded materials combined with radial basis functions was presented by Wang and Qin [124]. Mahi et al. [70] studied the free vibration of FGM beams subjected to initial thermal stress. Exact solutions based on several shear deformation theories were presented considering different boundary conditions. The temperature profile was computed solving a one-dimensional steady-state heat conduction equation. Thermal buckling and thermo-elastic vibration analysis of FGM beams were carried out by Wattanasakulpong et al. [125] by means of a third-order shear deformation theory. Material properties were considered to dependent on the temperature via a non-linear polynomial law [117]. The thermal response of orthotropic laminated plates was investigated by Carrera [20], through the comparison between theories formulated on the basis of the principle of virtual displacements (PVD) and mixed theories based on the Reissner's mixed variational theorem (RMVT). The effect of the through-the-thickness temperature profile on the accuracy of classical and advanced plate theories was studied by Carrera in [24]. The static response of functionally graded plates subjected to thermal loads was addressed by Brischetto et al. [14]. The temperature field was determined by solving Fourier's equation. Different volume fractions of the material constituents were considered to evaluate the temperature, displacement and stress distributions.

4.2 Unified formulation for thermo-mechanical analysis of beams: overview

The Unified Formulation (UF) seen in Sec.2, is extended in order to cover also the thermal analysis of composite and FGM beams. The temperature field is obtained by solving Fourier's heat conduction equation. Material gradation along the beam cross-section is concerned for functionally graded materials. The numerical investigations are carried out considering a power law variation along the beam thickness direction of the elastic and thermal material properties.

4.2.1 Constitutive equations for thermo-mechanical problems

In the case of thermo-mechanical problems, the constitutive equations (2.9) are:

$$\begin{aligned}\boldsymbol{\sigma}_p &= \boldsymbol{\sigma}_{pe} - \boldsymbol{\sigma}_{pt} = \mathbf{C}_{pp}\boldsymbol{\varepsilon}_p + \mathbf{C}_{pn}\boldsymbol{\varepsilon}_n - \lambda_p T \\ \boldsymbol{\sigma}_n &= \boldsymbol{\sigma}_{ne} - \boldsymbol{\sigma}_{nt} = \mathbf{C}_{np}\boldsymbol{\varepsilon}_p + \mathbf{C}_{nn}\boldsymbol{\varepsilon}_n - \lambda_n T\end{aligned}\quad (4.1)$$

where subscripts ‘*e*’ and ‘*t*’ refer to the elastic and the thermal contributions, respectively. The coefficients λ_n and λ_p :

$$\boldsymbol{\lambda}_n^T = \{ \lambda_1 \quad 0 \quad 0 \} \quad \boldsymbol{\lambda}_p^T = \{ \lambda_2 \quad \lambda_3 \quad 0 \} \quad (4.2)$$

are related to the thermal expansion coefficients α_n and α_p :

$$\boldsymbol{\alpha}_n^T = \{ \alpha_1 \quad 0 \quad 0 \} \quad \boldsymbol{\alpha}_p^T = \{ \alpha_2 \quad \alpha_3 \quad 0 \} \quad (4.3)$$

through the following equations:

$$\begin{aligned}\boldsymbol{\lambda}_p &= \mathbf{C}_{pp}\boldsymbol{\alpha}_p + \mathbf{C}_{pn}\boldsymbol{\alpha}_n \\ \boldsymbol{\lambda}_n &= \mathbf{C}_{np}\boldsymbol{\alpha}_p + \mathbf{C}_{nn}\boldsymbol{\alpha}_n\end{aligned}\quad (4.4)$$

A Lagrange approximation on N_p Chebyshev points along y and z cross-section coordinates based on Newton series expansion is assumed for the material stiffness coefficients C_{ij} and thermal coefficients λ_i :

$$\begin{aligned}C_{ij}(y, z) &\approx \omega_\xi(y)\omega_\eta(z)C_{ij}[y_0, y_1, \dots, y_\xi; z_0, z_1, \dots, z_\eta] \\ \lambda_i(y, z) &\approx \omega_\xi(y)\omega_\eta(z)\lambda_i[y_0, y_1, \dots, y_\xi; z_0, z_1, \dots, z_\eta]\end{aligned}\quad \text{with } \xi, \eta = 0, 1, \dots, N_p \quad (4.5)$$

being:

$$\omega_m(\zeta) = \begin{cases} 1 & m = 0 \\ \prod_{n=0}^{m-1} (\zeta - \zeta_n) & m \in [1, N_p] \end{cases} \quad (4.6)$$

and $C_{ij}[\dots; \dots]$ and $\lambda_i[\dots; \dots]$ the divided difference of the approximated function, see Philips [86]. Chebyshev’s points are defined on the domain $[-1, +1]$ via the following equation:

$$\zeta_m = \cos\left(\frac{m\pi}{N_p}\right) \quad \text{with } m = 0, 1, \dots, N_p \quad (4.7)$$

These points are then mapped into the cross-section domain via a variable transformation. In this manner the software implementation of the proposed models is general and does not depend upon a specific gradation law that, once defined, will be approximated via a Newton series expansion.

The beam models are derived considering the temperature (T) as an external loading resulting from the internal thermal stresses. This requires that temperature profile is known over the whole beam domain. Fourier’s heat conduction equation is solved in order to obtain T . The temperature is written as follows:

$$T(x, y, z) = \Theta_n(x)\Theta_\Omega(y, z) \quad (4.8)$$

4.2.2 Fourier’s heat conduction equation

A solution of Fourier’s heat conduction equation for FGM beams can be obtained by ideally dividing the cross-section Ω into N_{Ω^k} non-overlapping sub-domains (or layers) along the through-the-thickness direction z :

$$\Omega = \bigcup_{k=1}^{N_{\Omega^k}} \Omega^k \quad (4.9)$$

Each sub-domain is, then, supposed to be homogeneous, being the elastic and material properties constant and equal to the value at sub-domain’s centre. For a k^{th} homogeneous and isotropic layer, the Fourier differential equation becomes:

$$\frac{\partial^2 T^k}{\partial x^2} + \frac{\partial^2 T^k}{\partial y^2} + \frac{\partial^2 T^k}{\partial z^2} = 0 \quad (4.10)$$

In order to obtain a closed form analytical solution, it is further assumed that the temperature does not depend upon the through-the-width co-ordinate y . This also implies that the material gradation law should be independent from y . The continuity of the temperature and the through-the-thickness heat flux q_z hold at each interface between two consecutive sub-domains:

$$\begin{aligned} T_t^k &= T_b^{k+1} \\ q_{zt}^k &= q_{zb}^{k+1} \end{aligned} \quad (4.11)$$

Subscript ‘t’ and ‘b’ stand for sub-domain top and bottom, respectively. The through-the-thickness heat flux is proportional to the temperature derivative versus z :

$$q_z^k = K^k \frac{\partial T^k}{\partial z} \quad (4.12)$$

being K^k the thermal conductivity. The following temperatures are imposed at cross-section through-the-thickness top and bottom:

$$\begin{aligned} T &= T_t \sin(\alpha x) \\ T &= T_b \sin(\alpha x) \end{aligned} \quad (4.13)$$

T_t and T_b are the maximal amplitudes and α has been introduced in Eq. 2.34. The following temperature field:

$$T^k(x, z) = \Theta_{\Omega}^k(z) \sin(\alpha x) = T_0^k \exp(sz) \sin(\alpha x) \quad (4.14)$$

represents a solution of the considered heat conduction problem. T_0^k is an unknown constant obtained by imposing the boundary condition, whereas s is obtained by replacing Eq. 4.14 into Eq. 4.10:

$$s_{1,2} = \pm \alpha \quad (4.15)$$

$\Theta_{\Omega}^k(z)$, therefore, becomes:

$$\Theta_{\Omega}^k(z) = T_{01}^k \exp(+\alpha z) + T_{02}^k \exp(-\alpha z) \quad (4.16)$$

or, equivalently:

$$\Theta_{\Omega}^k(z) = C_1^k \cosh(\alpha z) + C_2^k \sinh(\alpha z) \quad (4.17)$$

The solution can be written as:

$$T(x, z) = \left[C_1^k \cosh\left(s_1^k z\right) + C_2^k \sinh\left(s_1^k z\right) \right] \sin\left(\frac{m\pi x}{l}\right) \quad (4.18)$$

where the unknown coefficients C_1^k and C_2^k are constant for each layer k . If N_l is the number of layer, we have $2N_l$ unknowns and we need $2N_l$ equations to determine them. The temperature at the top and bottom surfaces is known and therefore we have the following two conditions:

$$\begin{aligned} T_b &= C_1^1 \cosh\left(s_1^1 z_b\right) + C_2^1 \sinh\left(s_1^1 z_b\right) \\ T_t &= C_1^{N_l} \cosh\left(s_1^{N_l} z_t\right) + C_2^{N_l} \sinh\left(s_1^{N_l} z_t\right) \end{aligned} \quad (4.19)$$

Others $N_l - 1$ equations can be obtained from the continuity of temperature at each interface, whereas $N_l - 1$ equations result from the continuity of the heat flux through the interfaces, as written in Equation (4.11). We can write:

$$\begin{aligned} C_1^k \cosh\left(s_1^k z_t^k\right) + C_2^k \sinh\left(s_1^k z_t^k\right) - C_1^{k+1} \cosh\left(s_1^{k+1} z_b^{k+1}\right) + C_2^{k+1} \sinh\left(s_1^{k+1} z_b^{k+1}\right) &= 0 \\ K_3^k C_1^k s_1^k \sinh\left(s_1^k z_t^k\right) + K_3^k C_2^k s_1^k \cosh\left(s_1^k z_t^k\right) - K_3^{k+1} C_1^{k+1} s_1^{k+1} \sinh\left(s_1^{k+1} z_b^{k+1}\right) + \\ -K_3^{k+1} C_2^{k+1} s_1^{k+1} \cosh\left(s_1^{k+1} z_b^{k+1}\right) &= 0 \end{aligned} \quad (4.20)$$

In Equation 4.20, z_t^k and z_b^{k+1} represent the top of the k -th layer and the bottom of the $(k + 1)$ -th layer, respectively. Solving the system given by Equations 4.19 and 4.20 we obtain the N_l coefficients C_1^k and C_2^k . Therefore we can compute the temperature at different values of z and x coordinates.

4.3 Governing Equations

The governing equations and the boundary conditions are derived through the PVD:

$$\delta L_i = 0 \quad (4.21)$$

where δ stands for a virtual variation and L_i represents the strain energy. According to the grouping of the stress and strain components in Eqs. (2.4) and (2.5), the virtual variation of the strain energy for a thermo-mechanical case is:

$$\delta L_i = \int_l \int_{\Omega} [\delta \epsilon_n^T (\sigma_{ne} - \sigma_{nt}) + \delta \epsilon_p^T (\sigma_{pe} - \sigma_{pt})] d\Omega dx \quad (4.22)$$

By substitution of the geometrical relations, Eqs. (2.7), the constitutive equations, Eqs. (4.1), and the unified hierarchical approximation of the displacements, Eq. (2.12), Eq. (4.22) becomes:

$$\begin{aligned} \delta L_i = & \int_l \delta \mathbf{u}_\tau^T \int_\Omega \left[(\mathbf{D}_{np} F_\tau)^T \mathbf{C}_{np} (\mathbf{D}_p F_s) + (\mathbf{D}_{np} F_\tau)^T \mathbf{C}_{nn} (\mathbf{D}_{np} F_s) + (\mathbf{D}_{np} F_\tau)^T \mathbf{C}_{nn} F_s \mathbf{D}_{nx} \right. \\ & + (\mathbf{D}_p F_\tau)^T \mathbf{C}_{pp} (\mathbf{D}_p F_s) + (\mathbf{D}_p F_\tau)^T \mathbf{C}_{pn} (\mathbf{D}_{np} F_s) + (\mathbf{D}_p F_\tau)^T \mathbf{C}_{pn} F_s \mathbf{D}_{nx} \\ & \left. + \mathbf{D}_{nx}^T \mathbf{C}_{np} F_\tau (\mathbf{D}_p F_s) + \mathbf{D}_{nx}^T \mathbf{C}_{nn} F_\tau (\mathbf{D}_{np} F_s) + \mathbf{D}_{nx}^T \mathbf{C}_{nn} F_\tau F_s \mathbf{D}_{nx} \right] d\Omega \mathbf{u}_s dx \\ & - \int_l \delta \mathbf{u}_\tau^T \int_\Omega \left[(\mathbf{D}_{np} F_\tau)^T (\lambda_n \Theta_\Omega \mathbf{I}) + (\mathbf{D}_p F_\tau)^T (\lambda_p \Theta_\Omega \mathbf{I}) + \mathbf{D}_{nx}^T F_\tau (\lambda_n \Theta_\Omega \mathbf{I}) \right] d\Omega \Theta_n dx \end{aligned} \quad (4.23)$$

After integration by parts, Eq. (4.23) reads:

$$\begin{aligned} \delta L_i = & \int_l \delta \mathbf{u}_\tau^T \int_\Omega \left[(\mathbf{D}_{np} F_\tau)^T \mathbf{C}_{np} (\mathbf{D}_p F_s) + (\mathbf{D}_{np} F_\tau)^T \mathbf{C}_{nn} (\mathbf{D}_{np} F_s) + (\mathbf{D}_{np} F_\tau)^T \mathbf{C}_{nn} F_s \mathbf{D}_{nx} \right. \\ & + (\mathbf{D}_p F_\tau)^T \mathbf{C}_{pp} (\mathbf{D}_p F_s) + (\mathbf{D}_p F_\tau)^T \mathbf{C}_{pn} (\mathbf{D}_{np} F_s) + (\mathbf{D}_p F_\tau)^T \mathbf{C}_{pn} F_s \mathbf{D}_{nx} \\ & \left. - \mathbf{D}_{nx}^T \mathbf{C}_{np} F_\tau (\mathbf{D}_p F_s) - \mathbf{D}_{nx}^T \mathbf{C}_{nn} F_\tau (\mathbf{D}_{np} F_s) - \mathbf{D}_{nx}^T \mathbf{C}_{nn} F_\tau F_s \mathbf{D}_{nx} \right] d\Omega \mathbf{u}_s dx \\ & - \int_l \delta \mathbf{u}_\tau^T \int_\Omega \left[(\mathbf{D}_{np} F_\tau)^T (\lambda_n \Theta_\Omega \mathbf{I}) + (\mathbf{D}_p F_\tau)^T (\lambda_p \Theta_\Omega \mathbf{I}) - \mathbf{D}_{nx}^T F_\tau (\lambda_n \Theta_\Omega \mathbf{I}) \right] d\Omega \Theta_n dx \\ & + \delta \mathbf{u}_\tau^T \int_\Omega F_\tau [\mathbf{C}_{np} (\mathbf{D}_p F_s) + \mathbf{C}_{nn} (\mathbf{D}_{np} F_s) + \mathbf{C}_{nn} F_s \mathbf{D}_{nx}] d\Omega \mathbf{u}_s \Big|_{x=0}^{x=l} \\ & - \delta \mathbf{u}_\tau^T \int_\Omega F_\tau (\lambda_n \Theta_\Omega \mathbf{I}) d\Omega \Theta_n \Big|_{x=0}^{x=l} \end{aligned} \quad (4.24)$$

In a compact vectorial form:

$$\delta L_i = \int_l \delta \mathbf{u}_\tau^T \bar{\mathbf{K}}_{uu}^{\tau s} \mathbf{u}_s dx - \int_l \delta \mathbf{u}_\tau^T \bar{\mathbf{K}}_{u\theta}^{\tau} \Theta_n dx + [\delta \mathbf{u}_\tau^T \bar{\mathbf{\Pi}}_{uu}^{\tau s} \mathbf{u}_s]_{x=0}^{x=l} - [\delta \mathbf{u}_\tau^T \bar{\mathbf{\Pi}}_{u\theta}^{\tau} \Theta_n]_{x=0}^{x=l} \quad (4.25)$$

The components of the differential stiffness matrix $\bar{\mathbf{K}}_{uu}^{\tau s}$ are:

$$\begin{aligned} \bar{K}_{uu_{xx}}^{\tau s} &= J_{\tau, y^s, y}^{66} + J_{\tau, z^s, z}^{55} - J_{\tau s}^{11} \frac{\partial^2}{\partial x^2} & \bar{K}_{uu_{xy}}^{\tau s} &= \left(J_{\tau, y^s}^{66} - J_{\tau s, y}^{12} \right) \frac{\partial}{\partial x} & \bar{K}_{uu_{xz}}^{\tau s} &= \left(J_{\tau, z^s}^{55} - J_{\tau s, z}^{13} \right) \frac{\partial}{\partial x} \\ \bar{K}_{uu_{yy}}^{\tau s} &= J_{\tau, y^s, y}^{22} + J_{\tau, z^s, z}^{44} - J_{\tau s}^{66} \frac{\partial^2}{\partial x^2} & \bar{K}_{uu_{yx}}^{\tau s} &= \left(J_{\tau, y^s}^{12} - J_{\tau s, y}^{66} \right) \frac{\partial}{\partial x} & \bar{K}_{uu_{yz}}^{\tau s} &= J_{\tau, y^s, z}^{23} + J_{\tau, z^s, y}^{44} \\ \bar{K}_{uu_{zz}}^{\tau s} &= J_{\tau, y^s, y}^{44} + J_{\tau, z^s, z}^{33} - J_{\tau s}^{55} \frac{\partial^2}{\partial x^2} & \bar{K}_{uu_{zx}}^{\tau s} &= \left(J_{\tau, z^s}^{13} - J_{\tau s, z}^{55} \right) \frac{\partial}{\partial x} & \bar{K}_{uu_{zy}}^{\tau s} &= J_{\tau, z^s, y}^{23} + J_{\tau, y^s, z}^{44} \end{aligned} \quad (4.26)$$

The generic term $J_{\tau(\cdot, \phi)^s(\cdot, \xi)}^{gh}$ is a cross-section moment:

$$J_{\tau(\cdot, \phi)^s(\cdot, \xi)}^{gh} = \int_\Omega C_{gh} F_{\tau(\cdot, \phi)} F_{s(\cdot, \xi)} d\Omega \quad (4.27)$$

The components of the differential thermo-mechanical coupling matrix $\overline{\mathbf{K}}_{u\theta}^\tau$ are:

$$\overline{K}_{u\theta_{xx}}^\tau = -J_\tau^1 \frac{\partial}{\partial x} \quad \overline{K}_{u\theta_{yy}}^\tau = J_{\tau,y}^2 \quad \overline{K}_{u\theta_{zz}}^\tau = J_{\tau,z}^3 \quad (4.28)$$

The generic term $J_{\tau(\cdot,\phi)}^g$ is:

$$J_{\tau(\cdot,\phi)}^g = \int_{\Omega} F_{\tau(\cdot,\phi)} \lambda_g \Theta_\Omega \, d\Omega \quad (4.29)$$

As far as the boundary conditions are concerned, the components of $\overline{\mathbf{\Pi}}_{uu}^{\tau s}$ are:

$$\begin{aligned} \overline{\Pi}_{uu_{xx}}^{\tau s} &= J_{\tau s}^{11} \frac{\partial}{\partial x} & \overline{\Pi}_{uu_{xy}}^{\tau s} &= J_{\tau s,y}^{12} & \overline{\Pi}_{uu_{xz}}^{\tau s} &= J_{\tau s,z}^{13} \\ \overline{\Pi}_{uu_{yy}}^{\tau s} &= J_{\tau s}^{66} \frac{\partial}{\partial x} & \overline{\Pi}_{uu_{yx}}^{\tau s} &= J_{\tau s,y}^{66} & \overline{\Pi}_{uu_{yz}}^{\tau s} &= 0 \\ \overline{\Pi}_{uu_{zz}}^{\tau s} &= J_{\tau s}^{55} \frac{\partial}{\partial x} & \overline{\Pi}_{uu_{zx}}^{\tau s} &= J_{\tau s,z}^{55} & \overline{\Pi}_{uu_{zy}}^{\tau s} &= 0 \end{aligned} \quad (4.30)$$

and the components of $\overline{\mathbf{\Pi}}_{u\theta}^\tau$ are:

$$\overline{\Pi}_{u\theta_{xx}}^\tau = J_\tau^1 \quad \overline{\Pi}_{u\theta_{yy}}^\tau = 0 \quad \overline{\Pi}_{u\theta_{zz}}^\tau = 0 \quad (4.31)$$

The fundamental nucleo of the governing equations in a compact vectorial form is:

$$\delta \mathbf{u}_\tau^T : \quad \overline{\mathbf{K}}_{uu}^{\tau s} \mathbf{u}_s = \overline{\mathbf{K}}_{u\theta}^\tau \Theta_n \quad (4.32)$$

In explicit form:

$$\delta u_{x\tau} : \quad -J_{\tau s}^{11} u_{xs,xx} + \left(J_{\tau,zs,z}^{55} + J_{\tau,y s,y}^{66} \right) u_{xs} + \left(J_{\tau,y s}^{66} - J_{\tau s,y}^{12} \right) u_{ys,x} + \left(J_{\tau,zs}^{55} - J_{\tau s,z}^{13} \right) u_{zs,x} = -J_\tau^1 \Theta_{n,x}$$

$$\delta u_{y\tau} : \quad \left(J_{\tau,y s}^{12} - J_{\tau s,y}^{66} \right) u_{xs,x} - J_{\tau s}^{66} u_{ys,xx} + \left(J_{\tau,y s,y}^{22} + J_{\tau,zs,z}^{44} \right) u_{ys} + \left(J_{\tau,y s,z}^{23} + J_{\tau,zs,y}^{44} \right) u_{zs} = J_\tau^2 \Theta_n$$

$$\delta u_{z\tau} : \quad \left(J_{\tau,zs}^{13} - J_{\tau s,z}^{55} \right) u_{xs,x} + \left(J_{\tau,zs,y}^{23} + J_{\tau,y s,z}^{44} \right) u_{ys} - J_{\tau s}^{55} u_{zs,xx} + \left(J_{\tau,zs,z}^{33} + J_{\tau,y s,y}^{44} \right) u_{zs} = J_{\tau,z}^3 \Theta_n \quad (4.33)$$

The fundamental nucleo of the natural and mechanical boundary conditions at $x = 0$ and l are:

$$\begin{aligned} \text{either } u_{x\tau} &= \overline{u}_{x\tau} \quad \text{or } J_{\tau s}^{11} u_{xs,x} + J_{\tau s,y}^{12} u_{ys} + J_{\tau s,z}^{13} u_{zs} - J_\tau^1 \Theta_n = 0 \\ \text{either } u_{y\tau} &= \overline{u}_{y\tau} \quad \text{or } J_{\tau s,y}^{66} u_{xs} + J_{\tau s}^{66} u_{ys,x} = 0 \\ \text{either } u_{z\tau} &= \overline{u}_{z\tau} \quad \text{or } J_{\tau s,z}^{55} u_{xs} + J_{\tau s}^{55} u_{zs,x} = 0 \end{aligned} \quad (4.34)$$

For a fixed approximation order, the nucleo has to be expanded versus the indexes τ and s in order to obtain the governing equations and the boundary conditions of the desired model.

4.4 Closed Form Analytical Solution

The differential equations are solved via a Navier-type solution. Simply supported beams are, therefore, investigated. The following harmonic form for the axial variation of the displacement and temperature fields is adopted:

$$\begin{aligned}
 u_x &= U_{x\tau} F_\tau(y, z) \cos(\alpha x) \\
 u_y &= U_{y\tau} F_\tau(y, z) \sin(\alpha x) \\
 u_z &= U_{z\tau} F_\tau(y, z) \sin(\alpha x) \\
 T &= \Theta_\Omega(y, z) \Theta_n(x) = \Theta_\Omega \sin(\alpha x)
 \end{aligned} \tag{4.35}$$

where α is:

$$\alpha = \frac{m\pi}{l} \tag{4.36}$$

$m \in \mathbf{N}^+$ represents the half-wave number along the beam axis. $\{U_{i\tau} : i = x, y, z\}$ are the maximal amplitudes of the displacement components. Upon substitution of Eqs. (4.35) into Eqs. (4.33), the algebraic fundamental nucleo is obtained:

$$\begin{aligned}
 \delta U_{x\tau} : \\
 \left(\alpha^2 J_{\tau s}^{11} + J_{\tau, z s, z}^{55} + J_{\tau, y s, y}^{66} \right) U_{xs} + \alpha \left(J_{\tau, y s}^{66} - J_{\tau s, y}^{12} \right) U_{ys} + \alpha \left(J_{\tau, z s}^{55} - J_{\tau s, z}^{13} \right) U_{zs} &= -\alpha J_\tau^1 \\
 \delta U_{y\tau} : \\
 \alpha \left(J_{\tau s, y}^{66} - J_{\tau, y s}^{12} \right) U_{xs} + \left(\alpha^2 J_{\tau s}^{66} + J_{\tau, y s, y}^{22} + J_{\tau, z s, z}^{44} \right) U_{ys} + \left(J_{\tau, y s, z}^{23} + J_{\tau, z s, y}^{44} \right) U_{zs} &= J_\tau^2 \\
 \delta U_{z\tau} : \\
 \alpha \left(J_{\tau s, z}^{55} - J_{\tau, z s}^{13} \right) U_{xs} + \left(J_{\tau, z s, y}^{23} + J_{\tau, y s, z}^{44} \right) U_{ys} + \left(\alpha^2 J_{\tau s}^{55} + J_{\tau, z s, z}^{33} + J_{\tau, y s, y}^{44} \right) U_{zs} &= J_\tau^3
 \end{aligned} \tag{4.37}$$

4.5 Numerical Results and Discussion

4.5.1 Isotropic material

Isotropic beams made of an aluminium alloy are first considered. The mechanical properties are: $E = 72$ GPa, $\nu = 0.3$, $K = 121$ W/m°C, $\tilde{\alpha} = 23 \cdot 10^{-6}$ °C⁻¹. Square cross-sections are considered. The sides of the cross-section are $a = b = 0.1$ m. The length-to-side ratio l/b is equal to 100, ten and five. Slender and deep beams are, therefore, investigated. The half-wave number m in Equation 4.36 is assumed equal to one. The thermal boundary conditions are: $T_b = 25^\circ\text{C}$ and $T_t = 500^\circ\text{C}$. Displacements and stresses are evaluated in the following points:

$$\begin{aligned}
 u_x \text{ at } (l, -a/2, b/2) \quad u_y \text{ at } (l/2, 0, b/2) \quad u_z \text{ at } (l/2, a/2, b/2) \\
 \sigma_{xx} \text{ at } (l/2, 0, a/2) \quad \sigma_{xz} \text{ at } (0, -a/2, 0) \quad \sigma_{zz} \text{ at } (l/2, -a/2, 0)
 \end{aligned} \tag{4.38}$$

Results are reported in Tables 4.1- 4.6 and in Figures 4.1- 4.6.

	u_z	$u_x \times -10^2$	$u_y \times 10^4$
FEM 3D ^a	1.1074	3.6608	5.7491
FEM 3D ^b	1.1074	3.6608	5.7480
$N \geq 6$	1.1074	3.6608	5.7499
$N = 3 - 5$	1.1074	3.6608	5.7498
$N = 2$	1.1074	3.6607	5.7496
TB	2.4480	8.0953	–
EB	2.4480	8.0951	–

a: mesh 50x20x20
b: mesh 50x10x10

Table 4.1. Displacements ([m]), isotropic beam, $l/b = 100$

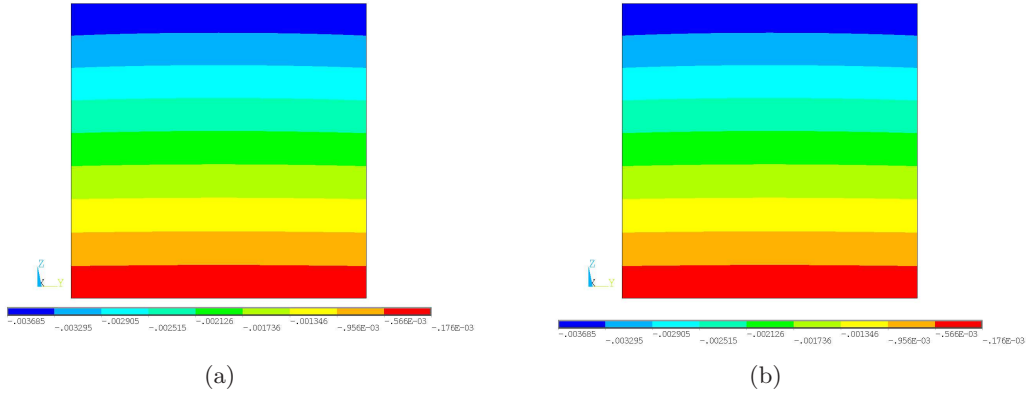


Figure 4.1. Axial displacement u_x ([m]), isotropic beam, $l/b = 10$ via (a) FEM 3-D solution and (b) $N = 8$ model

As far as validation is concerned, results are compared with three-dimensional FEM solutions obtained via the commercial code ANSYS[®]. The accuracy of the three-dimensional FEM solution depends upon the FEM numerical approximation. In order to present the convergence of the three-dimensional reference solution, for each case two different meshes are considered. Acronym FEM 3D^a stand for a three-dimensional FEM model with 50 elements along the axial direction and 20 elements along y and z directions. A coarser solution FEM 3D^b ($50 \times 10 \times 10$ elements) is also considered. Although the three-dimensional FEM solution and the analytical one are different in nature, some considerations about computational time and effort can be addressed. For the reference FEM simulations, the

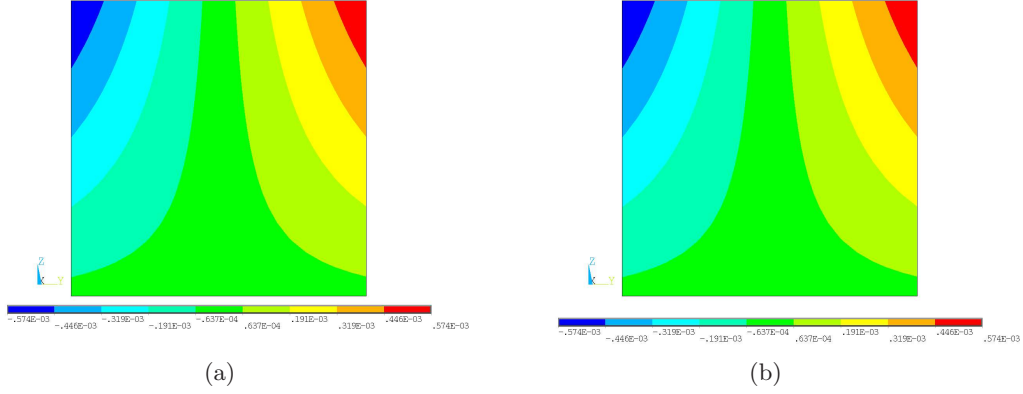


Figure 4.2. Transverse displacement u_y ([m]), isotropic beam, $l/b = 10$ via (a) FEM 3-D solution and (b) $N = 8$ model

	$\sigma_{xx} \times -10^{-4}$	$\sigma_{xz} \times -10^{-6}$	$\sigma_{zz} \times -10^{-4}$
FEM 3D ^a	3.4121	1.4966	1.6846
FEM 3D ^b	3.2153	1.4851	1.6603
$N = 13$	3.1923	1.5003	1.6930
$N = 12$	3.1984	1.5025	1.6963
$N = 11$	3.2027	1.5025	1.6963
$N = 10$	3.1989	1.4917	1.7028
$N = 9$	3.2007	1.4917	1.7028
$N = 8$	3.1705	1.4963	1.7114
$N = 7$	3.1473	1.4963	1.7114
$N = 6$	3.2616	1.5951	1.5673
$N = 5$	3.0066	1.5951	1.5672
$N = 4$	3.3814	1.3200	1.0693
$N = 3$	4.1457	1.3200	1.0693
$N = 2$	8.1480	1.1880	-5.4997
TB	-1.0031E+9	3.0745E-6	—
EB	-1.0031E+9	—	—

a: mesh 50x20x20

b: mesh 50x10x10

Table 4.2. Stresses ([Gpa]), isotropic beam, $l/b = 100$

	$u_z \times 10^2$	$u_x \times -10^3$	$u_y \times 10^4$
FEM 3D ^a	1.1511	3.6847	5.7362
FEM 3D ^b	1.1511	3.6847	5.7362
$N \geq 9$	1.1511	3.6847	5.7362
$N = 8$	1.1511	3.6848	5.7362
$N = 7$	1.1511	3.6848	5.7361
$N = 6$	1.1511	3.6845	5.7356
$N = 5$	1.1511	3.6845	5.7349
$N = 4$	1.1513	3.6868	5.7337
$N = 3$	1.1513	3.6868	5.7330
$N = 2$	1.1501	3.6757	5.7111
TB	2.4440	8.0546	–
EB	2.4440	8.0546	–

a: mesh 50x20x20

b: mesh 50x10x10

Table 4.3. Displacements ([m]), isotropic beam, $l/b = 10$

	$\sigma_{xx} \times -10^{-6}$	$\sigma_{xz} \times -10^{-7}$	$\sigma_{zz} \times -10^{-6}$
FEM 3D ^a	3.1717	1.4860	1.6574
FEM 3D ^b	3.2093	1.4745	1.6333
$N = 13$	3.1560	1.4898	1.6657
$N = 12$	3.1620	1.4920	1.6690
$N = 11$	3.1664	1.4920	1.6690
$N = 10$	3.1627	1.4812	1.6753
$N = 9$	3.1642	1.4813	1.6755
$N = 8$	3.1342	1.4859	1.6844
$N = 7$	3.1106	1.4860	1.6841
$N = 6$	3.2221	1.5843	1.5441
$N = 5$	2.9749	1.5841	1.5398
$N = 4$	3.3527	1.3100	1.0496
$N = 3$	4.1150	1.3100	1.0518
$N = 2$	8.0406	1.1822	–5.4328
TB	–993.90	–	–
EB	–993.90	–	–

a: mesh 50x20x20

b: mesh 50x10x10

Table 4.4. Stresses ([Gpa]), isotropic beam, $l/b = 10$

	$u_z \times 10^3$	$u_x \times -10^3$	$u_y \times 10^4$
FEM 3D ^a	3.2029	1.8774	5.6949
FEM 3D ^b	3.2029	1.8774	5.6949
$N \geq 11$	3.2029	1.8774	5.6949
$N = 10$	3.2029	1.8774	5.6948
$N = 9$	3.2029	1.8774	5.6948
$N = 8$	3.2029	1.8775	5.6946
$N = 7$	3.2029	1.8775	5.6942
$N = 6$	3.2029	1.8770	5.6922
$N = 5$	3.2030	1.8770	5.6894
$N = 4$	3.2044	1.8813	5.6846
$N = 3$	3.2046	1.8813	5.6818
$N = 2$	3.1910	1.8599	5.5971
TB	6.0802	3.9679	–
EB	6.0802	3.9679	–

a: mesh 50x20x20

b: mesh 50x10x10

Table 4.5. Displacements ([m]), isotropic beam, $l/b = 5$

	$\sigma_{xx} \times 10^{-7}$	$\sigma_{xz} \times 10^{-7}$	$\sigma_{zz} \times 10^{-6}$
FEM 3D ^a	1.2257	2.9092	6.3141
FEM 3D ^b	1.2401	2.8857	6.2204
$N = 13$	1.2197	2.9168	6.3462
$N = 12$	1.2221	2.9214	6.3588
$N = 11$	1.2239	2.9214	6.3587
$N = 10$	1.2225	2.8999	6.3826
$N = 9$	1.2228	2.9000	6.3859
$N = 8$	1.2111	2.9096	6.4232
$N = 7$	1.2012	2.9102	6.4186
$N = 6$	1.2425	3.1042	5.9066
$N = 5$	1.1526	3.1025	5.8409
$N = 4$	1.3072	2.5603	3.9693
$N = 3$	1.6096	2.5605	4.0041
$N = 2$	3.0914	2.3297	–20.949
TB	96.706	–	–
EB	96.706	–	–

a: mesh 50x20x20

b: mesh 50x10x10

Table 4.6. Stresses ([Gpa]), isotropic beam, $l/b = 5$

computational time is as high as about 20 minutes (refined mesh) and as low as 5 minutes (coarsest mesh). In the case of the proposed analytical solutions, the computational time is few second regardless the considered approximation order. For slender beams, low expansion orders results match already the FEM solutions for displacements, whereas for stresses, higher expansion orders are required. This behaviour becomes more evident for deep beams. $N = 9$ or 11 is necessary to obtain good results for displacements when l/b is 10 and 5. For stresses, the higher expansion orders are necessary even for deep beams. Classical theories provide very poor results if compared with those obtained via higher-order models.

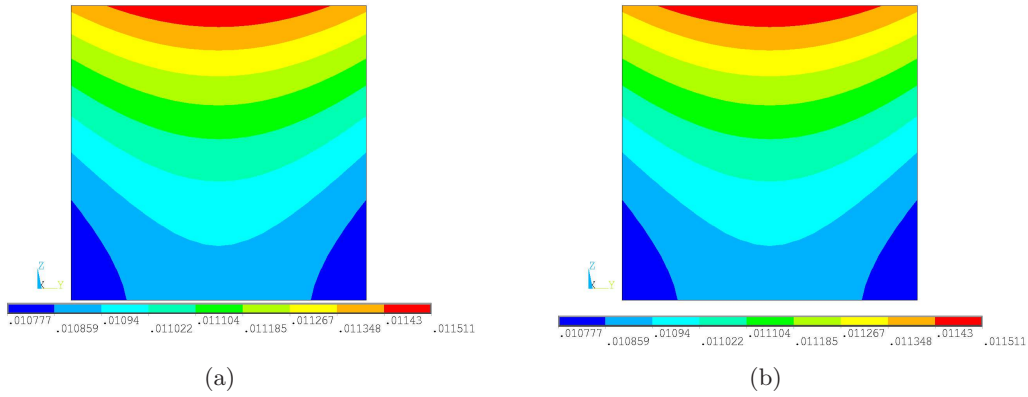


Figure 4.3. Transverse displacement u_z ([m]), isotropic beam, $l/b = 10$ via (a) FEM 3-D solution and (b) $N = 8$ model

Figures 4.1- 4.6 show the displacements and stresses fields at the beam cross-section in $x = 0$ or $x = l/2$. The considered expansion order is $N = 8$ and the slenderness ratio is $l/b = 10$. In general, $N = 8$ is sufficient to achieve a good overall solution along the cross-section of the beam, while in tables there is a set set of punctual values, and then higher orders of expansion are necessary to reduce the error.

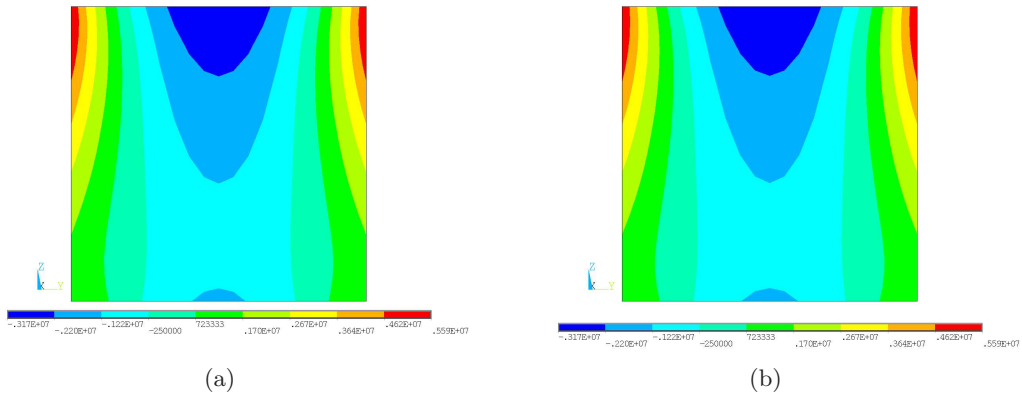


Figure 4.4. Axial stress σ_{xx} ([GPa]), isotropic beam, $l/b = 10$ via (a) FEM 3-D solution and (b) $N = 8$ model

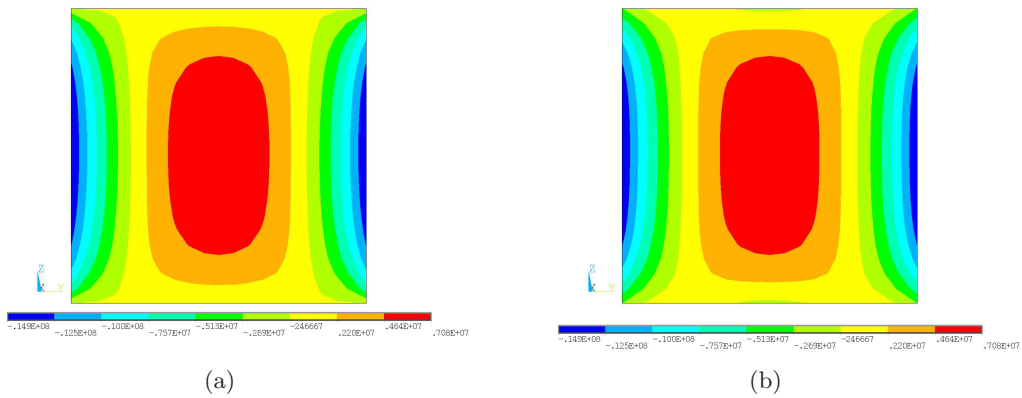


Figure 4.5. Shear stress σ_{xz} ([GPa]), isotropic beam, $l/b = 10$ via (a) FEM 3-D solution and (b) $N = 8$ model

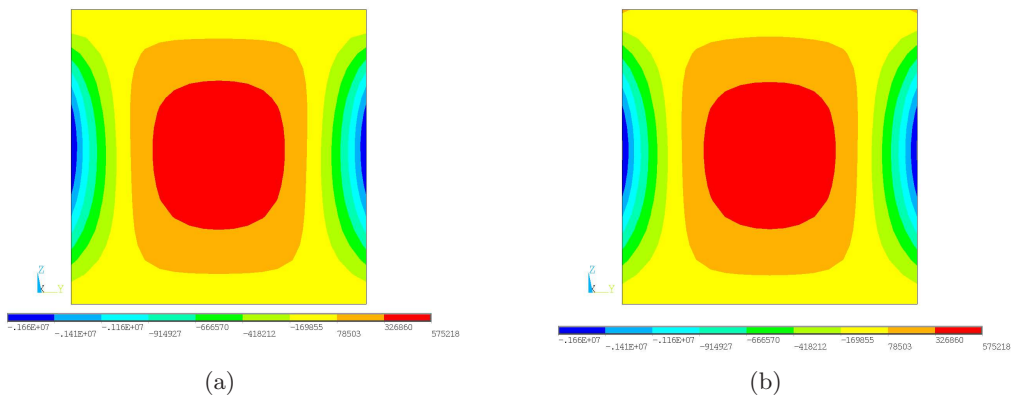


Figure 4.6. Out-of-plane Ω stress σ_{zz} ([GPa]), isotropic beam, $l/b = 10$ via (a) FEM 3-D solution and (b) $N = 8$ model

4.5.2 Orthotropic material

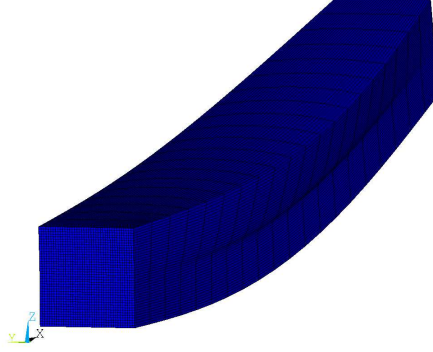


Figure 4.7. Deformation of the beam, $l/b = 10$

Composite beams are considered in this section. The mechanical properties are: $E_L = 172.72 \times 10^9$ Pa, $E_T = 6.91 \times 10^9$ Pa, $G_{LT} = 3.45 \times 10^9$ Pa, $G_{TT} = 1.38 \times 10^9$ Pa, $\nu_{LT} = \nu_{TT} = 0.25$, $K_L = 36.42$ W/mK, $K_T = 0.96$ W/mK, $\tilde{\alpha}_L = 0.57 \cdot 10^{-6} \text{K}^{-1}$, $\tilde{\alpha}_T = 35.60 \cdot 10^{-6} \text{K}^{-1}$. A two layers $[0/90]$ lamination, starting from the bottom, is considered. Square cross-sections are considered. The sides of the cross-section are $a = b = 1$ m. The length-to-side ratio l/b is equal to ten. The thermal boundary conditions are: $T_b = 0$ K and $T_t = 1$ K. In Figure 4.7 is reported the deformed shape of the beam. The behaviour after deformation is due to the 90° layer that is on the top of the beam and has a small value of $\tilde{\alpha}_L$. Results for displacements and stresses are presented in Figure 4.8. Higher-order models result necessary when we consider composite beams. From the pictures we notice that at the interface of the two layers we have the higher errors, compared to the FEM3D solution. A layer-wise approach could better identify the behaviour of the beam.

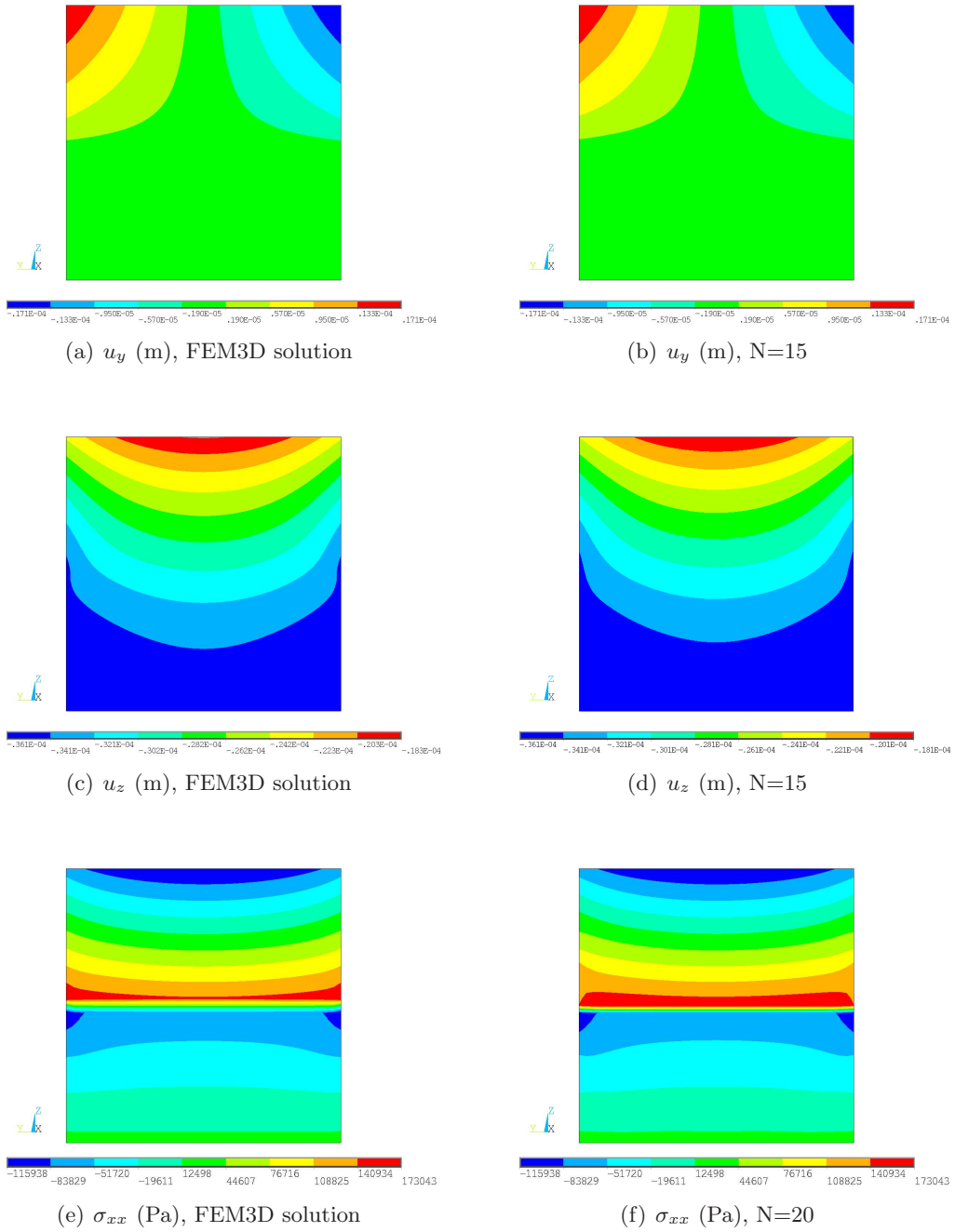


Figure 4.8. Composite beam, $l/b = 10$

4.5.3 Functionally Graded Materials

Beams made of ceramic metal Functionally Graded Materials (FGMs) are able to combine temperature resistance and a continuous stress distribution because of the smooth variation of material properties along some preferred directions.

A ceramic-metallic gradation along the thickness direction is considered. The ceramic phase is made of Zirconia (ZrO_2), whereas Monel (70Ni-30Cu), a nickel-based alloy, is considered as metallic phase. Materials properties are presented in Table. 4.7. The generic

	E [GPa]	ν	K [W/mK]	α [10^{-6} K $^{-1}$]
Zirconia	151.01	0.300	2.09	10.
Monel	179.40	0.368	25.00	15.

Table 4.7. FGM constituents elastic and thermal properties.

material property, f , is assumed to vary versus the thickness coordinate z according to the power law distribution of Eq. 3.1.

$$f = (f_1 - f_2) (\alpha_z z + \beta_z)^{n_z} + f_2 \quad (4.39)$$

n_z is the power law exponent and it is equal to the unit, f_i is the generic material property of each constituent and α_z and β_z are two constant coefficients that depend upon the through-the-thickness extension of the FGM layer and the through-the-thickness position of the center of the reference system, which is centred at the cross-section bottom left corner. A mono-layer and a sandwich FGM cross-section configuration are investigated. In the case of the mono-layer FGM cross-section and for the assumed reference system, $\alpha_z = 1/b$ and $\beta_z = 0$. The half-wave number m in Eq. (4.36) is equal to one. The thermal boundary conditions (see Eq. 4.13) are: $T_t = +400$ K and $T_b = +300$ K. Square cross-sections with sides length $a = b = 1$ m are considered. The length-to-side ratio l/a is equal 100 and 10. Slender and deep beams are, therefore, investigated. As far as tabular results are concerned, the displacements and stresses evaluated at the following points are considered:

$$\begin{aligned} \bar{u}_x &= u_x(0, a/2, b) & \bar{u}_y &= u_y(l/2, a, b) & \bar{u}_z &= u_z(l/2, a/2, b/2) \\ \bar{\sigma}_{xx} &= \sigma_{xx}(l/2, a/2, b/2) & \bar{\sigma}_{xz} &= \sigma_{xz}(0, 0, b/2) & \bar{\sigma}_{zz} &= \sigma_{zz}(l/2, a/2, b/2) \end{aligned} \quad (4.40)$$

Results obtained using the proposed higher-order models are compared with three-dimensional FEM solutions obtained via the commercial code ANSYS[®]. The three-dimensional quadratic element “Solid90” is used for the thermal analysis, whereas the 20-node element “Solid186” is considered for the mechanical problem. For a FGM layer, each element is considered as homogeneous by referring to the material properties at its centre. The accuracy of the three-dimensional FEM solution depends upon both the FEM numerical approximation and the approximation of the gradation law. In order to present the convergence of the three-dimensional reference solution, two different meshes are considered for each analysis. The acronym FEM 3D^a stands for a three-dimensional FEM model with a $30 \times 30 \times 30$

elements mesh, whereas the coarser $20 \times 20 \times 20$ mesh solution is addressed by FEM 3D^b. Although the three-dimensional FEM solution and the analytical one are different in nature, some considerations about computational effort can be addressed. The degrees of freedom (DOFs) of the three-dimensional FEM mechanical problem over a beam cross-section as function of the number of elements for each side, n , are $3(3n + 1)(n + 1)$. n is as low as 20 (DOFs = 3843) and as high as 30 (DOFs = 8463). For a fixed approximation order N , the DOFs of the proposed solutions are $3(N + 1)(N + 2)/2$. In the case of the highest considered expansion order ($N = 13$) they are 315.

Mono-layer FGM beam

Beams made of a single FGM layer, see Fig. 4.9, are first investigated. The temperature

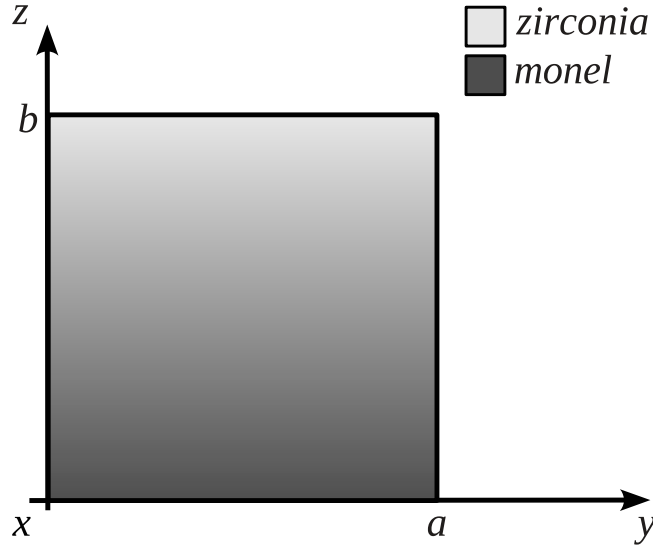
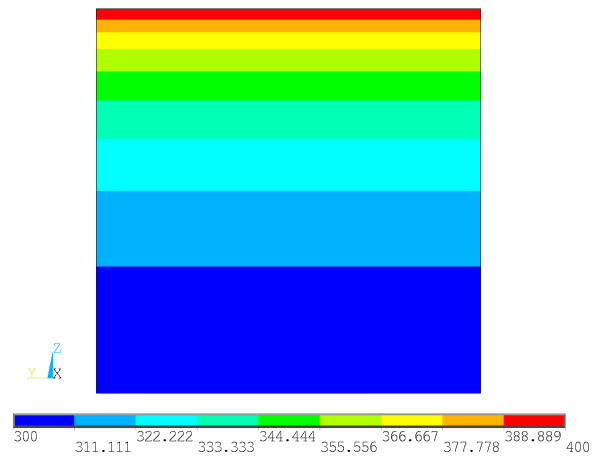
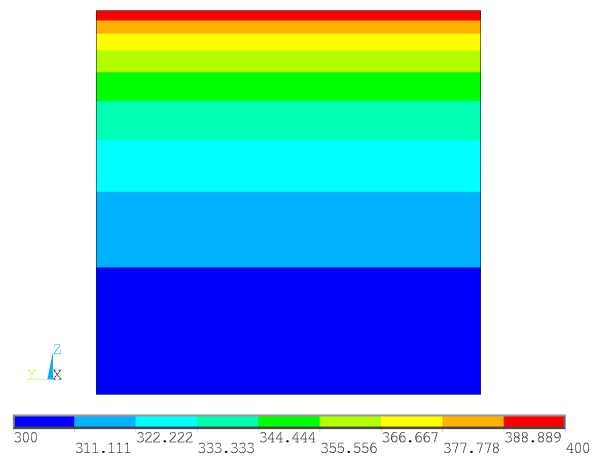


Figure 4.9. Mono-layer FGM beam.

variation over the cross-section at mid-span is presented in Figs. 4.10. The solution of Fourier's equation via the procedure presented in the Sec.4.2.2 has been obtained considering 16 fictitious layers. It matches the FEM 3D^a solution. Table 4.8 to 4.11 present the displacements and the stresses in Eqs. 4.40 for slender and thick beams. Differently from a bending mechanical load, a thermal load results in axial and through-the-thickness displacement components as well as normal stress components of comparable order of magnitude. This is due to the fact that in the former case the mechanics is mainly governed by bending (and shear, for thick beams), whereas the normal stresses along the other two directions are mainly due to the coupling governed by the Poisson effect. In the thermo-mechanical case, the deformations are governed by the thermal expansion coefficients. Classical theories yield a zero through-the-width displacement since, according to their kinematic hypotheses (see Eqs. 2.15 and 2.16), the cross-section is rigid on its



(a)



(b)

Figure 4.10. Mono-layer FGM beam temperature profile [K] at $x/l = 1/2$ via (a) Fourier's equation solution and (b) FEM $3D^a$, $l/a = 10$.

	$-10 \cdot \bar{u}_z$	$-10 \cdot \bar{u}_x$	$10^3 \cdot \bar{u}_y$
FEM 3D ^a	6.583	1.204	1.972
FEM 3D ^b	6.527	1.205	1.967
$N = 9 - 13$	6.533	1.205	1.961
$N = 8$	6.533	1.205	1.960
$N = 7$	6.533	1.205	1.958
$N = 6$	6.534	1.205	1.955
$N = 5$	6.534	1.205	1.950
$N = 4$	6.538	1.205	1.948
$N = 3$	6.537	1.205	1.937
$N = 2$	6.697	1.202	1.889
TBT	6.522	1.205	0.000
EBT	6.521	1.205	0.000

a: mesh $30 \times 30 \times 30$.

b: mesh $20 \times 20 \times 20$.

Table 4.8. Mono-layer FGM beam, displacements [m], $l/a = 100$.

	$10^{-7} \cdot \bar{\sigma}_{xx}$	$10^{-5} \cdot \bar{\sigma}_{xz}$	$10^{-6} \cdot \bar{\sigma}_{zz}$
FEM 3D ^a	1.088	2.247	5.522
FEM 3D ^b	1.098	2.239	5.590
$N = 13$	1.109	2.232	5.582
$N = 12$	1.119	2.235	5.778
$N = 11$	1.119	2.240	5.770
$N = 10$	1.121	2.231	5.804
$N = 9$	1.120	2.225	5.800
$N = 8$	1.115	2.218	5.736
$N = 7$	1.117	2.191	5.772
$N = 6$	1.171	2.293	6.618
$N = 5$	1.156	2.289	6.333
$N = 4$	0.885	1.892	1.516
$N = 3$	0.945	2.020	2.451
$N = 2$	2.351	1.573	23.55
TBT	0.793	4.135 ^c	– ^d
EBT	0.787	–	–

a: mesh $30 \times 30 \times 30$.

b: mesh $20 \times 20 \times 20$.

c: scale factor -10^5 (instead of 10^{-5}).

d: result not provided by the theory.

Table 4.9. Mono-layer FGM beam, stresses [Pa], $l/a = 100$.

	$-10^3 \cdot u_z$	$-10^2 \cdot u_x$	$10^3 \cdot u_y$
FEM 3D ^a	6.704	1.195	1.953
FEM 3D ^b	6.644	1.196	1.958
$N = 12, 13$	6.648	1.197	1.955
$N = 9 - 11$	6.648	1.197	1.954
$N = 8$	6.648	1.197	1.953
$N = 7$	6.648	1.197	1.952
$N = 6$	6.648	1.197	1.947
$N = 5$	6.648	1.197	1.943
$N = 4$	6.653	1.197	1.940
$N = 3$	6.655	1.197	1.929
$N = 2$	6.854	1.194	1.866
TBT	6.649	1.191	0.000
EBT	6.648	1.191	0.000

a: mesh $30 \times 30 \times 30$.

b: mesh $20 \times 20 \times 20$.

Table 4.10. Mono-layer FGM beam, displacements [m], $l/a = 10$.

	$10^{-6} \cdot \bar{\sigma}_{xx}$	$10^{-6} \cdot \bar{\sigma}_{xz}$	$10^{-6} \cdot \bar{\sigma}_{zz}$
FEM 3D ^a	8.635	2.292	6.459
FEM 3D ^b	8.738	2.284	6.535
$N = 13$	8.865	2.276	6.521
$N = 12$	8.968	2.279	6.722
$N = 11$	8.964	2.285	6.714
$N = 10$	8.980	2.276	6.740
$N = 9$	8.977	2.270	6.735
$N = 8$	8.915	2.261	6.663
$N = 7$	8.942	2.232	6.703
$N = 6$	9.540	2.335	7.648
$N = 5$	9.374	2.331	7.330
$N = 4$	6.383	1.925	2.011
$N = 3$	7.024	2.058	3.020
$N = 2$	23.19	1.601	27.53
TBT	10.62	4.090 ^c	– ^d
EBT	10.57	–	–

a: mesh $30 \times 30 \times 30$.

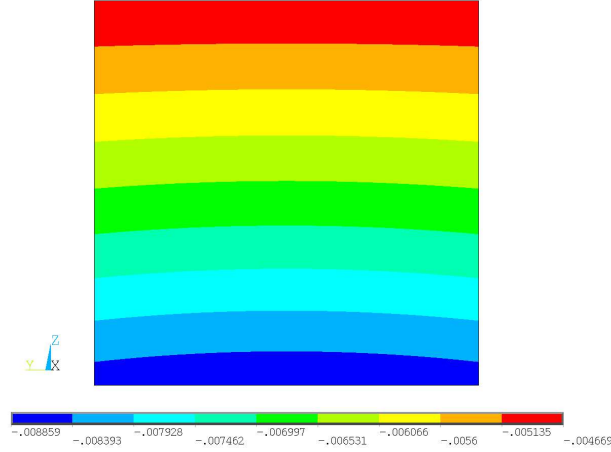
b: mesh $20 \times 20 \times 20$.

c: scale factor -10^5 (instead of 10^{-6}).

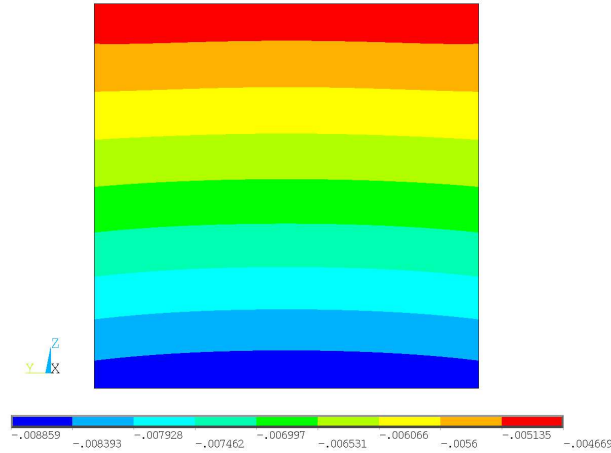
d: result not provided by the theory.

Table 4.11. Mono-layer FGM beam, stresses [Pa], $l/a = 10$.

own plane and the problem is symmetric versus a plane parallel to Oxz and passing at mid-width. Nevertheless, they provide a well globally estimated displacement field. As



(a)



(b)

Figure 4.11. Mono-layer FGM beam, u_z [m] at $x/l = 1/2$ via (a) $N = 4$ and (b) FEM $3D^a$, $l/a = 10$.

shown in Figs. 4.11 to 4.13, where the variation of the displacement components over the cross-section is presented, lower-order theories match the reference solution FEM $3D^a$. For instance, a fourth-order model is able to predict the trough-the-width variation of the axial displacement component, which it is constant in the case of TBT. As far as the stresses are concerned, higher-order models (e.g., N as low as eight) are required

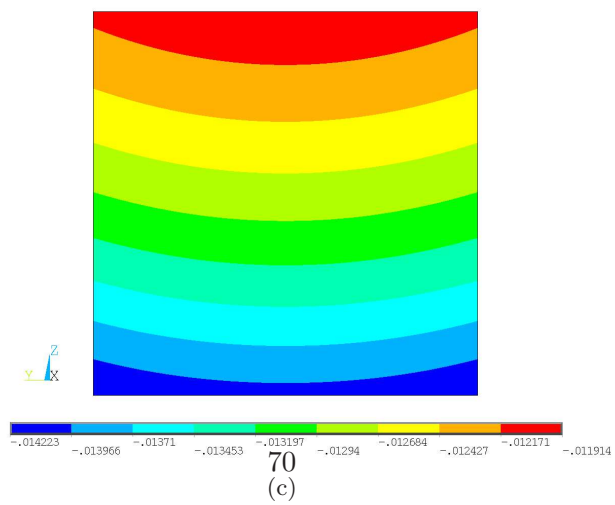
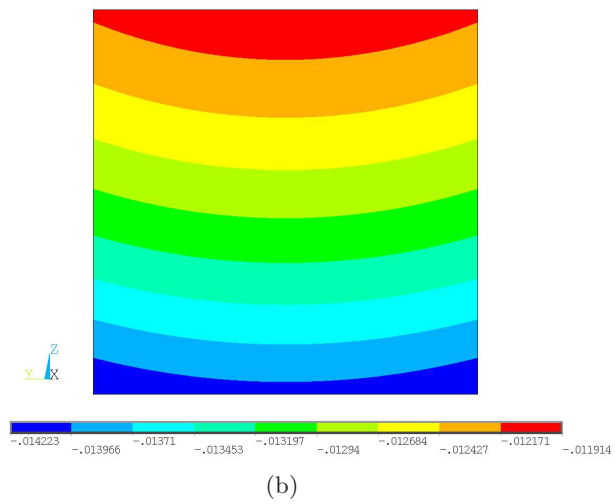
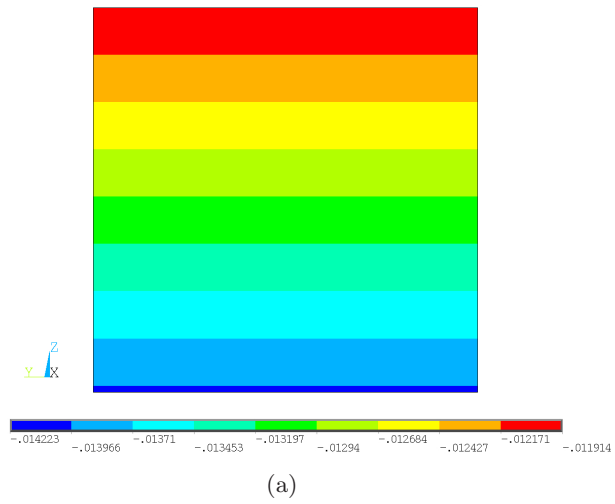
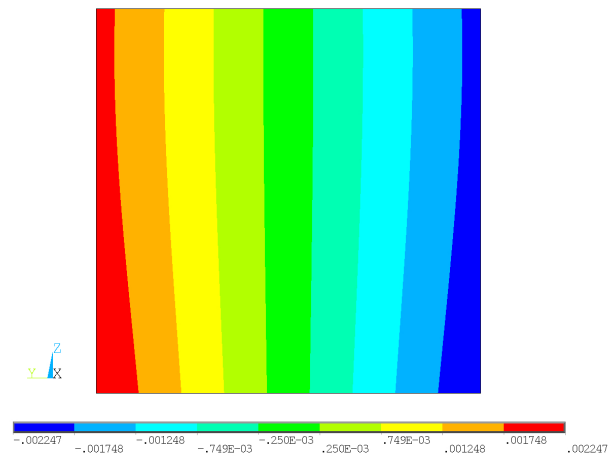
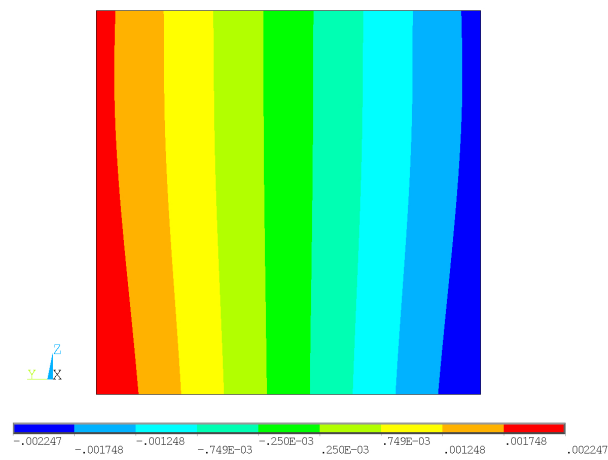


Figure 4.12. Mono-layer FGM beam, u_x [m] at $x/l = 0$ via (a) TBT, (b) $N = 4$ and (c) FEM $3D^a$, $l/a = 10$.



(a)



(b)

Figure 4.13. Mono-layer FGM beam, u_y [m] at $x/l = 1/2$ via (a) $N = 4$ and (b) FEM 3D^a, $l/a = 10$.

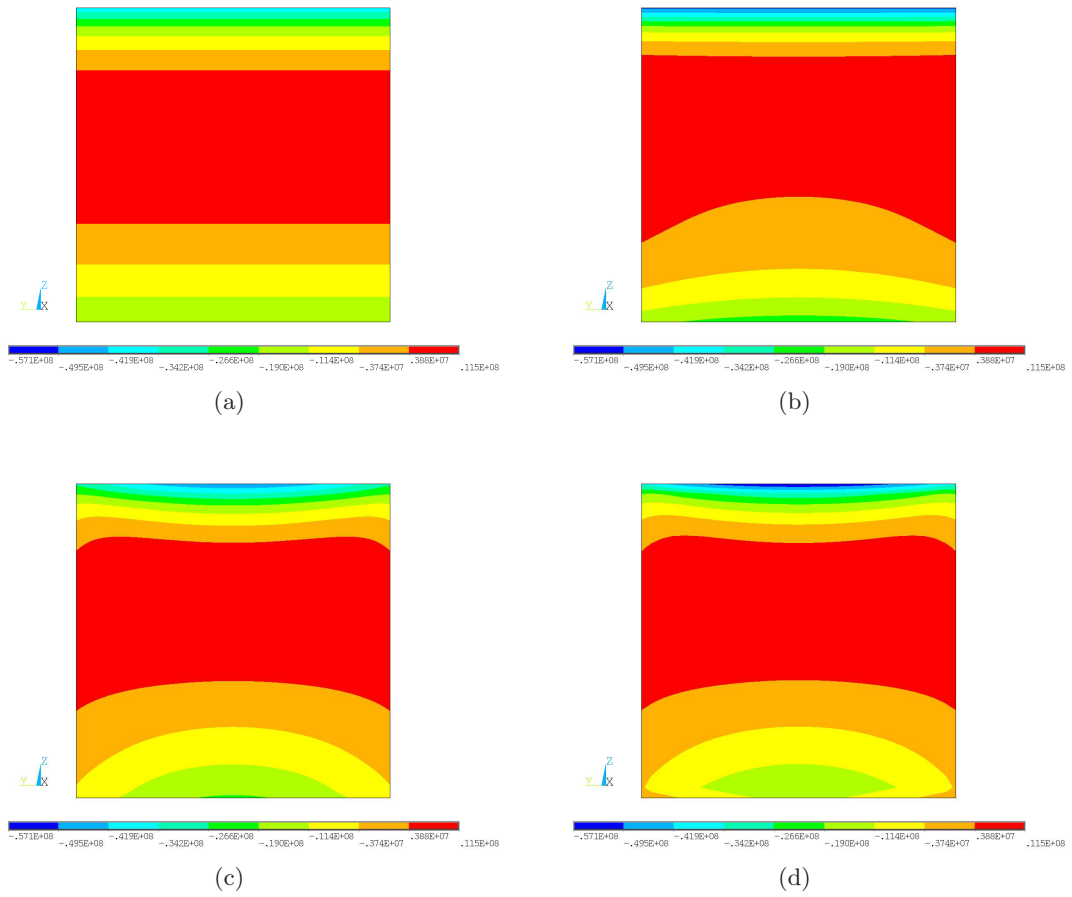


Figure 4.14. Mono-layer FGM beam, σ_{xx} [Pa] at $x/l = 1/2$ via (a) TBT, (b) $N = 4$, (c) $N = 13$ and (d) FEM $3D^a$, $l/a = 10$.

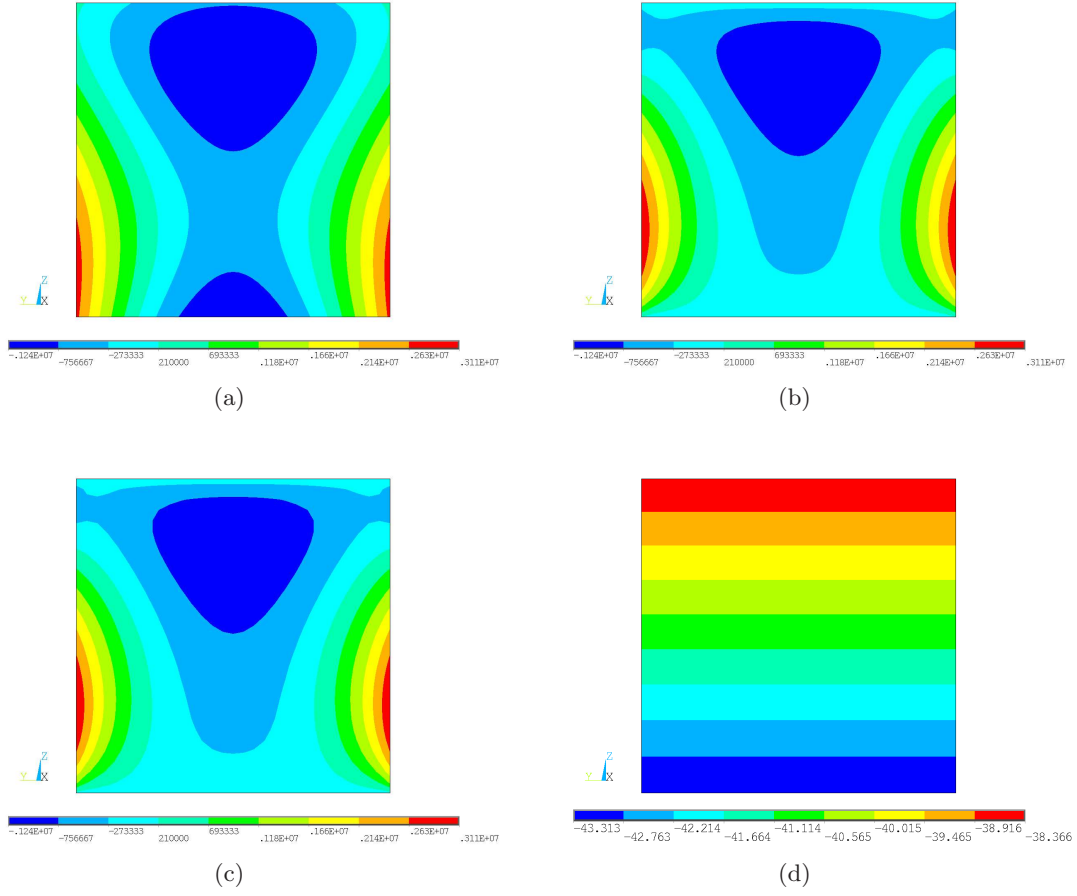
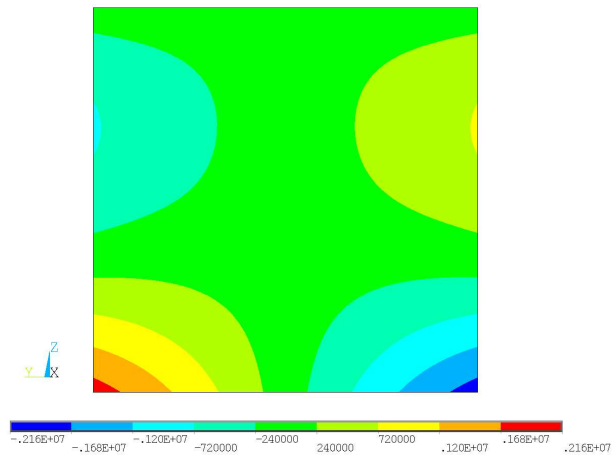
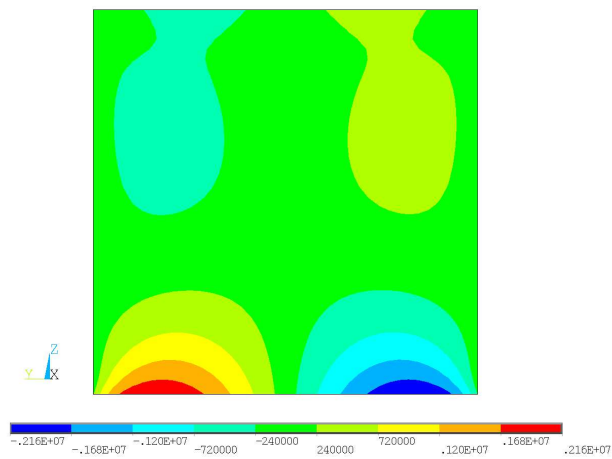


Figure 4.15. Mono-layer FGM beam, σ_{xz} [Pa] at $x/l = 0$ via (a) $N = 4$, (b) $N = 13$, (c) FEM $3D^a$ and (d) TBT, $l/a = 10$.

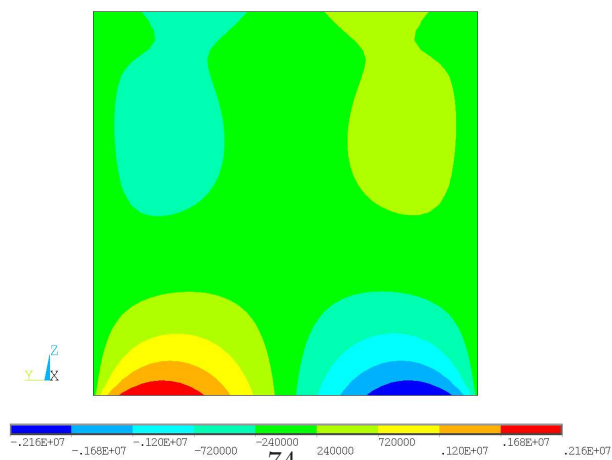
for an accurate solution. The stress field is three-dimensional. Figs. 4.14 show the axial stress component at mid-span cross-section. Results are obtained via, TBT, fourth- and 13th-order model and FEM $3D^a$. The latter presents a relevant through-the-width variation and a high through-the-thickness gradient, especially at cross-section top. This is very different from a typical mechanical problem of global bending. The solution for $N = 13$ compares globally well with the reference solution. The shear component σ_{xz} is presented in Figs. 4.15. TBT yields a solution several order of magnitude smaller than the reference solution. A different scale has been used in the figure and the tables for this reason. A steep stress gradient is present at both cross-section sides. $N = 13$ solution matches the reference one. Figs. 4.16 present σ_{xy} computed via $N = 4$ and 13 and FEM $3D^a$. The fourth-order theory yields an acceptable estimation in the neighbourhood of cross-section's centre. The last two solutions compare very well. This is also true for the shear component σ_{yz} presented in Figs. 4.17. The normal stress component σ_{yy} is shown



(a)

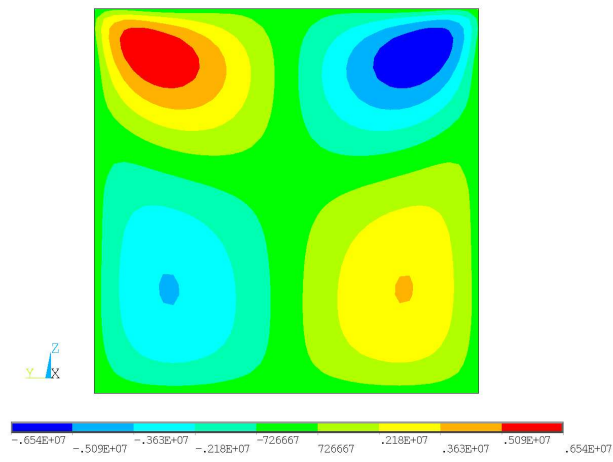


(b)

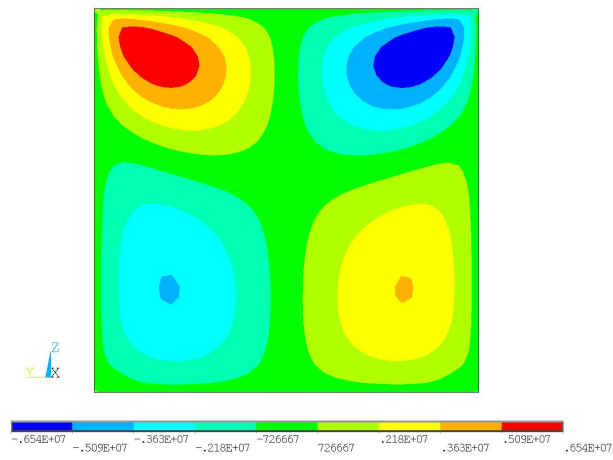


(c)

Figure 4.16. Mono-layer FGM beam, σ_{xy} [Pa] at $x/l = 0$ via (a) $N = 4$, (b) $N = 13$ and (c) FEM $3D^a$, $l/a = 10$.

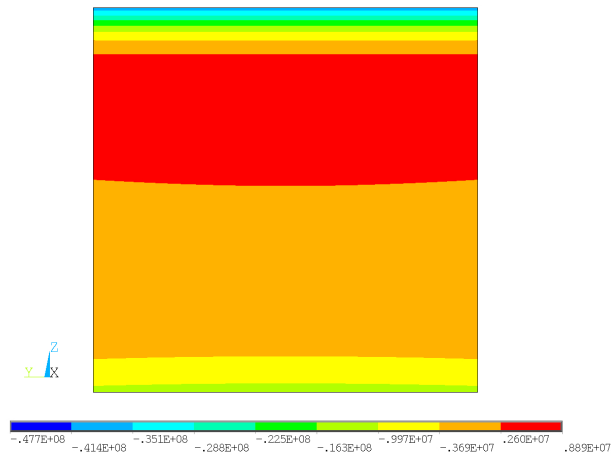


(a)

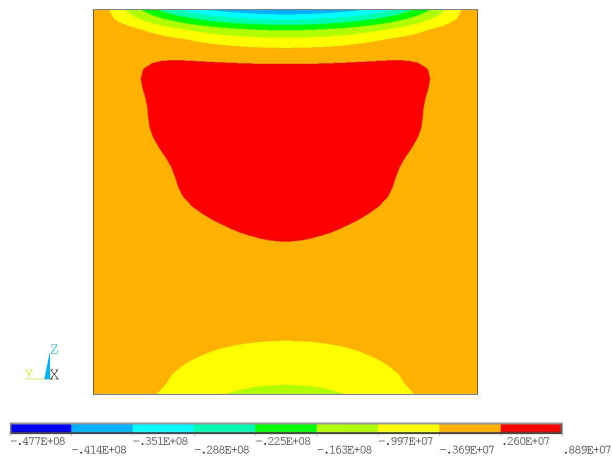


(b)

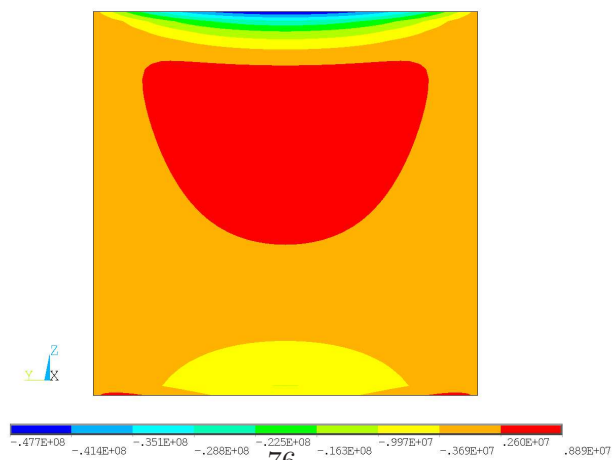
Figure 4.17. Mono-layer FGM beam, σ_{yz} [Pa] at $x/l = 1/2$ via (a) $N = 13$ and (c) FEM 3D^a, $l/a = 10$.



(a)

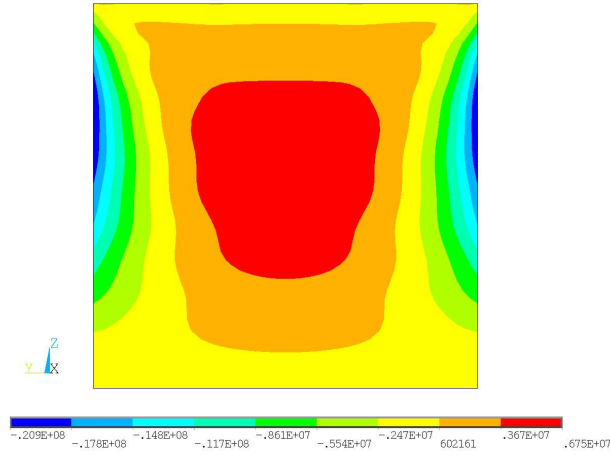


(b)

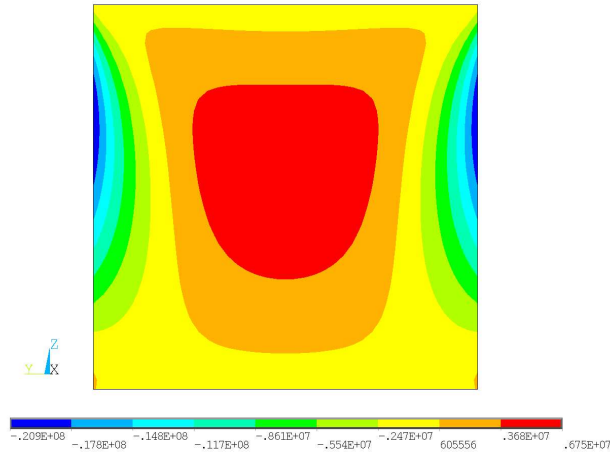


(c)

Figure 4.18. Mono-layer FGM beam, σ_{yy} [Pa] at $x/l = 1/2$ via (a) $N = 4$, (b) $N = 13$ and (c) FEM $3D^a$, $l/a = 10$.



(a)



(b)

Figure 4.19. Mono-layer FGM beam, σ_{zz} [Pa] at $x/l = 1/2$ via (a) $N = 13$ and (c) FEM $3D^a$, $l/a = 10$.

in Figs. 4.18. $N = 13$ and FEM $3D^a$ solutions compare fairly well. This stress component presents a relevant thought-the-width variation and localised stress zones. A fourth-order approximation is obviously not sufficient to describe it. $N = 13$ yields also a fairly accurate prediction of σ_{zz} as demonstrated by Figs. 4.19. The results presented in a graphical form have been all obtained for $l/a = 10$. The case of slender beams is very similar and it is not presented here for the sake of brevity.

4.5.4 Sandwich FGM beam

A FGM sandwich configuration is investigated, see Fig. 4.20. A FGM core connects the top

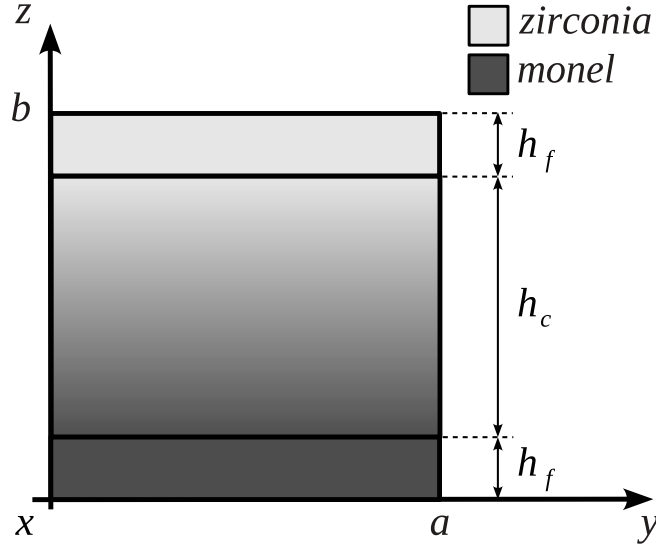


Figure 4.20. Sandwich FGM beam.

and bottom layers that are entirely made of zirconia and monel. The thickness, h_f , of the top and bottom faces is 0.1 times the cross-section side length. The solution of Fourier's equation is accurate when compared to the FEM 3D^a solution. It is not presented here for the sake of brevity. The main difference versus the mono-layer configuration is in a globally slightly cooler bottom part of the cross-section since the ceramic layer acts as a further thermal barrier. Displacements and stresses for slender and thick beams are presented in Table 4.12 to 4.15. Higher-order models match the reference three-dimensional FEM results. Lower-order and classical theories yield good displacements but are not capable of predicting the stress field properly. When compared with the mono-layer configuration, a higher transverse displacement (resulting in higher stresses) is observed. The temperature profile for the sandwich FGM beam is showed in fig. 4.21.

	$-1 \cdot u_z$	$-10 \cdot u_x$	$10^3 \cdot u_y$
FEM 3D ^a	1.022	1.126	1.919
FEM 3D ^b	1.019	1.127	1.902
$N = 11 - 13$	1.023	1.126	1.900
$N = 9, 10$	1.023	1.126	1.899
$N = 8$	1.023	1.126	1.898
$N = 7$	1.023	1.126	1.890
$N = 6$	1.024	1.126	1.883
$N = 5$	1.024	1.126	1.868
$N = 4$	1.024	1.126	1.865
$N = 3$	1.024	1.126	1.827
$N = 2$	1.047	1.122	1.763
TBT, EBT	1.021	1.126	0.000

a: mesh 30x30x30.

b: mesh 20x20x20.

Table 4.12. Sandwich FGM beam, displacements [m], $l/a = 100$.

	$10^{-7} \cdot \sigma_{xx}$	$10^{-5} \cdot \sigma_{xz}$	$10^{-6} \cdot \sigma_{zz}$
FEM 3D ^a	1.457	3.881	7.721
FEM 3D ^b	1.460	3.871	7.737
$N = 13$	1.465	3.870	7.828
$N = 12$	1.462	3.883	7.739
$N = 11$	1.449	3.911	7.479
$N = 10$	1.444	3.919	7.416
$N = 9$	1.463	3.912	7.811
$N = 8$	1.487	3.852	8.293
$N = 7$	1.502	3.749	8.528
$N = 6$	1.533	3.883	8.843
$N = 5$	1.422	3.826	6.777
$N = 4$	1.036	3.285	-0.090
$N = 3$	1.300	3.721	3.897
$N = 2$	3.118	2.459	31.22
TBT	1.037	4.869 ^c	- ^d
EBT	1.032	-	-

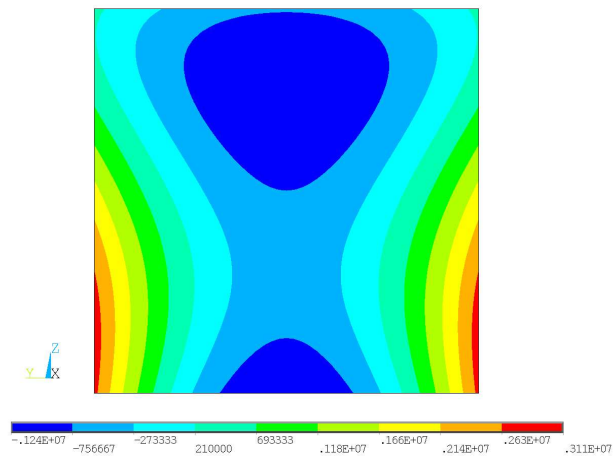
a: mesh 30x30x30.

b: mesh 20x20x20.

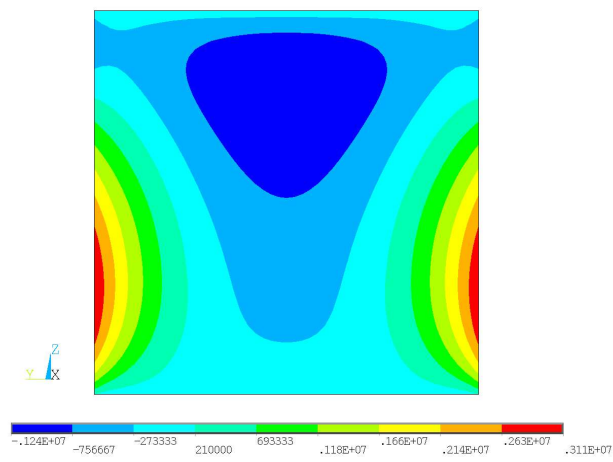
c: scale factor -10^5 (instead of 10^{-5}).

d: result not provided by the theory.

Table 4.13. Sandwich FGM beam, stresses [Pa], $l/a = 100$.



(a) FEM-3D



(b) N=13

Figure 4.21. Sandwich FGM beam temperature profile [K] at $x/l = 1/2$ via (a) Fourier's equation solution and (b) FEM 3D^a, $l/a = 10$.

	$-10^2 \cdot u_z$	$-10^2 \cdot u_x$	$10^3 \cdot u_y$
FEM 3D ^a	1.033	1.118	1.894
FEM 3D ^b	1.029	1.119	1.895
$N = 12, 13$	1.034	1.118	1.894
$N = 10, 11$	1.034	1.118	1.893
$N = 8, 9$	1.034	1.118	1.892
$N = 7$	1.034	1.118	1.883
$N = 6$	1.034	1.118	1.877
$N = 5$	1.033	1.118	1.861
$N = 4$	1.034	1.118	1.858
$N = 3$	1.034	1.118	1.818
$N = 2$	1.063	1.114	1.741
TBT	1.033	1.113	0.000
EBT	1.033	1.112	0.000

a: mesh 30x30x30.

b: mesh 20x20x20.

Table 4.14. Sandwich FGM beam, displacements [m], $l/a = 10$.

For the sake of brevity, only a 13th-order model is considered for the plots over the cross-section of displacements and stresses. Figs. 4.22 shows the displacement components. Results are practically identical. The stress components σ_n are presented in Figs. 4.23. The proposed results and the reference solutions match. The presence of an inner and outer homogeneous layer changes the profile of the axial stress increasing the maximum and minimum values and introducing a stress gradient also at the cross-section bottom. Finally, Figs. 4.24 present the stress components σ_p . The normal stress components also present localised stress areas that make them difficult to be correctly predicted, especially in the case of σ_{zz} . Nevertheless, fairly good results are obtained. A future work perspective consists in a the formulation of higher-order theories by means of a layer-wise approach that should enhance the accuracy of the approximation.

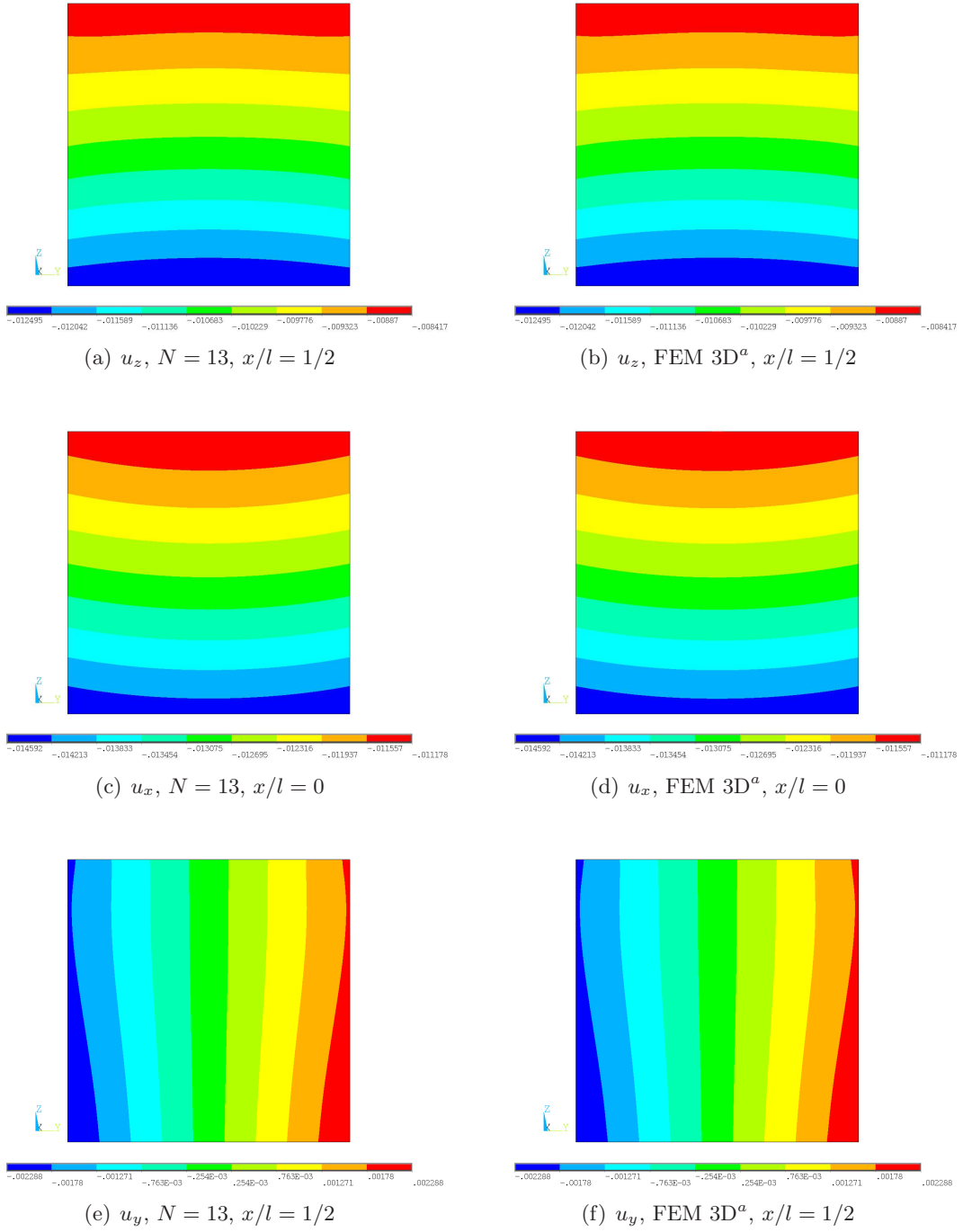


Figure 4.22. Sandwich FGM beam, displacements components [m] via $N = 13$ and FEM $3D^a$, $l/a = 10$.

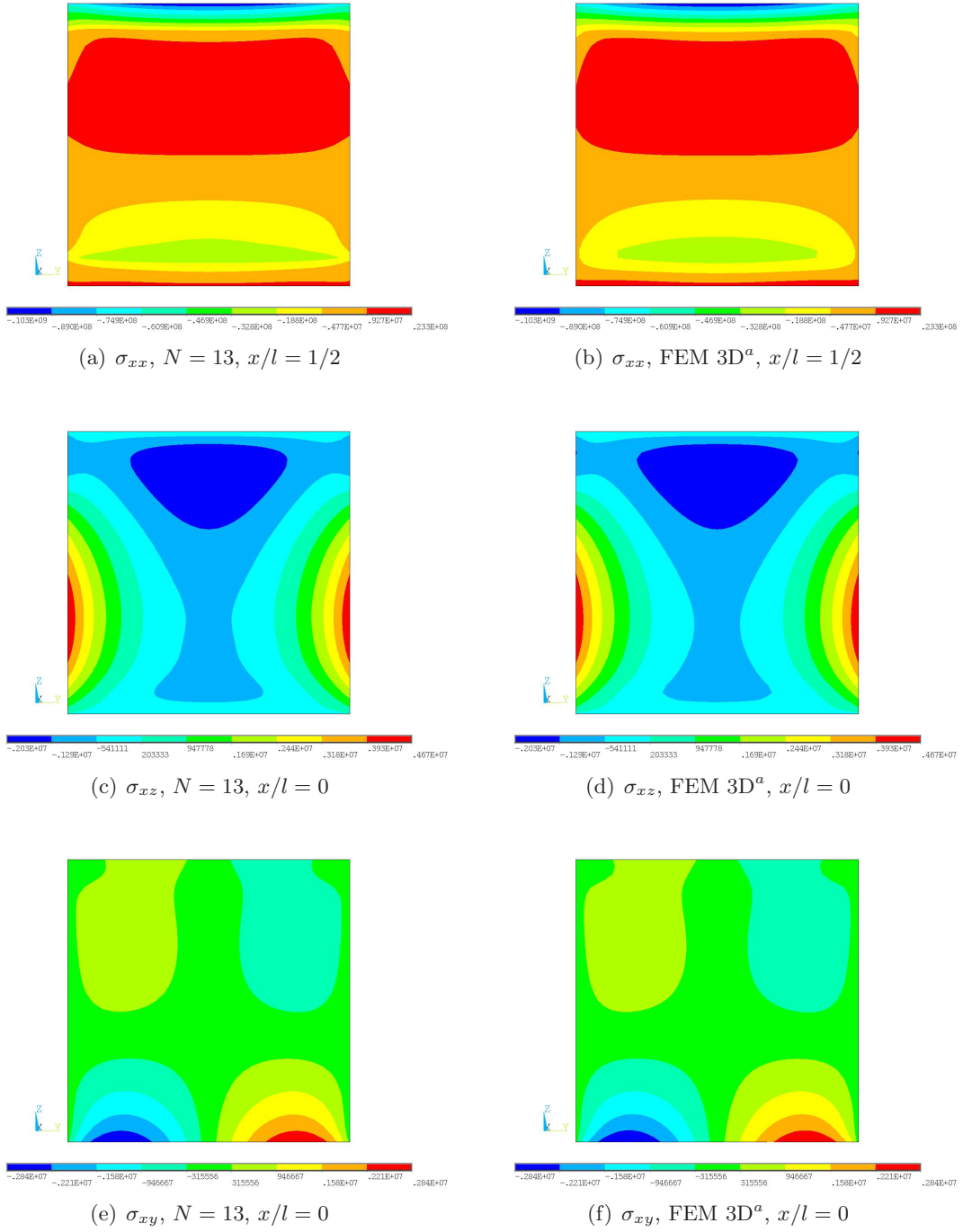


Figure 4.23. Sandwich FGM beam, σ_n stress components [Pa] via $N = 13$ and FEM $3D^a$, $l/a = 10$.

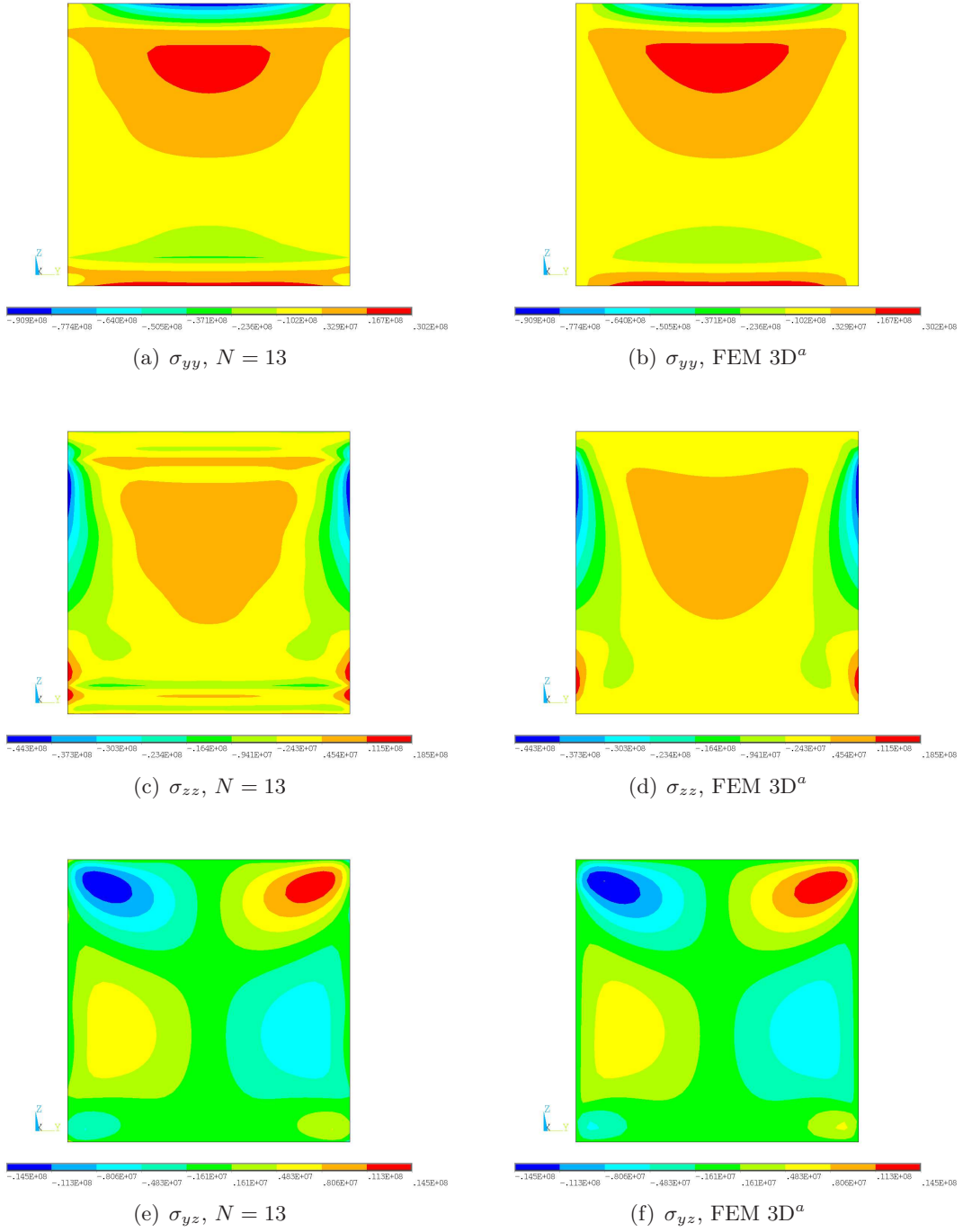


Figure 4.24. Sandwich FGM beam, σ_n stress components at $x/l = 1/2$ via $N = 13$ and FEM $3D^a$, $l/a = 10$.

	$10^{-7} \cdot \sigma_{xx}$	$10^{-6} \cdot \sigma_{xz}$	$10^{-6} \cdot \sigma_{zz}$
FEM 3D ^a	1.237	3.921	8.701
FEM 3D ^b	1.239	3.910	8.721
$N = 13$	1.245	3.910	8.802
$N = 12$	1.242	3.922	8.700
$N = 11$	1.229	3.951	8.441
$N = 10$	1.222	3.959	8.358
$N = 9$	1.242	3.951	8.757
$N = 8$	1.269	3.891	9.299
$N = 7$	1.284	3.785	9.526
$N = 6$	1.317	3.920	9.888
$N = 5$	1.206	3.863	7.790
$N = 4$	0.783	3.311	0.269
$N = 3$	1.053	3.752	4.346
$N = 2$	3.080	2.483	35.13
TBT	1.303	4.816 ^c	– ^d
EBT	1.297	–	–

a: mesh 30x30x30.

b: mesh 20x20x20.

c: scale factor -0.1 (instead of 10^{-6}).

d: result not provided by the theory.

Table 4.15. Sandwich FGM beam, stresses [Pa], $l/a = 10$.

4.6 Conclusions

A unified formulation of one-dimensional beam models has been proposed for the thermal analysis of isotropic, composite and functionally graded beams. The temperature field has been obtained by solving Fourier's heat conduction equation and it has been accounted for in the mechanical analysis as an external load. Results have been validated through comparison with three-dimensional FEM solutions obtained via the commercial code ANSYS[®]. It has been shown that the considered thermo-mechanical problems, although presenting a global bending deformation, are governed by three-dimensional stress fields that call for very accurate models. Through an appropriate choice of the approximation order over the cross-section, the proposed formulation yields accurate results with reduced computational costs.

Chapter 5

Refined shell's and plate's theories via Unified Formulation

5.1 Introduction

The development of appropriate shell theories is a well established topic in structural analysis of shell panels that are used to build significant structural parts of automotive, ship and aerospace vehicles, and shell-made civil constructions. Carrera Unified Formulation for the modelling of composite shell and plate structures is presented in the following. Via this approach, higher order, zig-zag, layer-wise and mixed theories can be easily formulated. As a particular case, the equations related to Love's approximations and Donnell's approximations and as well as of the corresponding classical lamination and shear deformation theories (CLT and FSDT) are derived. Classical theories (Classical Lamination Theory, CLT) developed for thin elastic shells are based on Love-Kirchhoff's [66] assumptions: (1) the shell is thin, (2) the deflections of the shell are small, (3) normal stresses that are perpendicular to the middle surface can be neglected in comparison with other stresses, and (4) straight lines that are normal to the undeformed middle surface remain straight and normal to the deformed middle surface. The last assumption leads to neglect the transverse shear strains. Over the last years, curved shell structures made of composite laminae have gained widespread acceptance for primary structural components due to high value of strength- and stiffness-to-weight ratios. Love-Kirchhoff's kinematic assumptions applied to layered anisotropic composite shells may not yield a correct prediction of displacement and stress fields. An elastic shell theory in which the thinness assumption is delayed has independently been derived by Flügge [48], Lur'E [67], and Byrne [15]. The introduction of transverse shear and normal stress represents an improvement to classical theories. The effects of transverse shear deformations (SDT-Shear Deformation Theory) and normal stresses have been considered by Hildebrand, Reissner and Thomas [53] and Reissner [100]. Non-linear theories were considered by Sanders [106]. Moreover, other approximations on curvature terms for shallow shell analysis have been introduced by Donnell [41] and Mushtari [79]. A survey of various classical shell theories can be found in the works of Naghdi [80] and Leissa [62].

The analysis of the vibration characteristics for shells and plates is a fundamental topic at the early design stage of these structures. The open literature offers several works concerning free vibration analysis of shell. Some of these are reviewed in the following text. A review of the recent researches (2000-2009) done on the dynamic behaviour of composite shells is presented by Qatu et al. [95]. This review includes about 200 references that are organized according to the following criteria: 1- shell theories, 2- shell geometries, 3- type of dynamic analysis, 4- material complexity, and 5- structural complexity. Laminated composite deep thick shells are investigated in the works of Qatu [89] and [90]. In [90] accurate stress resultant equations are derived including initial pre-twist and, further, the term $(1 + z/R)$. Free vibration analysis yielded frequencies that are close to those obtained by 3-D theory of elasticity. Homogeneous and composite thick barrel shells were investigated by Qatu in [93]. Several natural frequencies analyses are carried out, taking into account the curvature and thickness effects. Reddy and Liu [99] investigated the statics and the free vibrations of shallow thick cylindrical and spherical shells made of orthotropic layers via a cubic through-the-thickness approximation of the displacement components laying on shell surface and a constant transverse displacement. Governing equations were solved through a Navier-type solution. Chaudhuri and Kabir [34] used four classical shallow shell theories - Donnell, Sanders, Reissner and modified Sanders - to obtain Fourier series solutions for cross-ply doubly curved panels with simply supported boundary conditions. They extended CLT-based analytical solutions for cross-ply curved panels to other types of boundary conditions. A boundary-discontinuous double Fourier series approach was used to solve a system of three partial differential equations (one fourth-order and two second-order, in terms of the transverse displacement). In the work of Ferreira et al. [47], Reddy's higher-order shear deformation theory of laminated orthotropic elastic shells was implemented through a multiquadrics discretization of equations of motion and boundary conditions. Static and free vibration analyses of doubly curved laminated elastic shells were carried out by the use of third-order theory in combination with a meshless technique based on the multiquadric Radial Basis Function (RBF) method. Another mesh-free approach for vibration analysis of laminated composite cylindrical panels was presented by Zhao and Liew [132].

Some studies of vibration response of composite shells included the presence of a cut-out. In the work of Poore et al. [87] a semi-analytical solution method is presented for determining the natural frequencies and mode shapes of laminated cylindrical shells containing a circular cut-out. Sai Ram and Sreedhar Babu [105] investigated the free vibration of composite spherical shell caps with and without a cut-out. The analysis is carried out using the finite element method based on a higher-order shear deformation theory that accounts for rotary inertia and parabolic variation of transverse shear strain across the thickness. The transverse displacement of the shell is assumed constant through the thickness. Narasimhan and Alwar [81] studied the free vibration of orthotropic annular spherical shells with clamped boundary conditions at both the edges using Chebyshev-Galerkin spectral method. Fundamental frequencies were presented for cross-ply laminated shells with fibres oriented in circumferential and meridian directions. Xavier et al. [127] modelled the vibration of thick orthotropic laminated composite shells using a simple higher-order

layer-wise theory. The theory accounts for a cubic variation of both the in-plane displacements and the transverse shear stresses within each layer. They defined the General Performance Index (GPI) as a measure of the natural frequency and stress predicting capability of a theory. Composite cylindrical shells and their applications concerning free vibration analysis have been analysed by Yadav and Verma in [130], while Liew et al. presented a three-dimensional vibration analysis for spherical shells subjected to different boundary conditions in [65]. Matsunaga [73] presented a two-dimensional global higher-order theory of cross-ply laminated composite circular cylindrical shells, able to accurately predict natural frequencies and buckling stresses. The effects of both shear deformations with thickness changes and rotatory inertia were considered.

Approximated three-dimensional solutions can be obtained assuming that the ratio between the panel thickness and its middle surface radii is negligible as compared to unity. Bhimaraddi [13] analysed the free vibration of homogeneous and laminated doubly curved shells on rectangular planform and made of orthotropic material using the three-dimensional elasticity equations. Ye and Soldatos [131] studied the three-dimensional flexural vibration response of laminated cylindrical shell panels of symmetric and antisymmetric cross-ply material. Recently, static and free vibration characteristics of anisotropic laminated cylindrical shell were analyzed applying the differential quadrature method (DQM) by Alibeigloo [1].

Nowadays, the use of composite materials is well established since these materials exhibit high transverse shear deformation and discontinuous material properties in the thickness direction. Both of these features require the development of refined theories, [23, 25] for an accurate and effective design. Soldatos [112] presented a good survey of the theories adopted in the dynamic analysis of composite laminated shells, while a review of equivalent-single-layer and layerwise laminate theories is presented by Reddy [98]. In the first survey, governing equations and numerical results are quoted for Donnell's, Love's, Sanders' and Flügge's theories based on CLT approximations, and for Donnell's, Love's and Sanders' theories based on SDT approximations. In [17] the first author investigated of CLT and SDT assumptions and Donnell, Love and Flügge theories on buckling and vibrations of cross-ply laminated composite shells. More recent analyses are reported in the articles by Qatu [91, 92] and more extensively in the book by the same author [94] that documents some of the latest research in the field of vibration of composite shells and plates, presenting also deep thick shells. To the best of the authors' knowledge, no exhaustive results are known in which the approximation related to refined models, including transverse normal strain effects, are compared with those introduced by curvature (Love, Donnell).

The Unified Formulation (UF) [18, 26] allows formulating several two-dimensional models on the basis of the choice of the a-priori main unknowns (displacements or mixed models), the approximation level (laminate or lamina level), the through-the-thickness polynomial approximation order. As a result, an exhaustive variable kinematic model has been obtained: models that account for the transverse normal and shear deformability, the continuity of the transverse stress components and the zig-zag variation along the thickness of displacement and transverse normal stresses can be formulated straightforwardly. The use of the refined theory has made it possible to conduct a quite comprehensive analysis

of the thickness locking phenomenon (also known as Poisson locking) in the bending and vibration of metallic shells [29].

5.2 Geometry

Shells are bi-dimensional structures with one dimension, in general the thickness along z direction, negligible with respect to the others two on the reference surface directions. The main features of shell geometry are shown in Fig. 5.1.

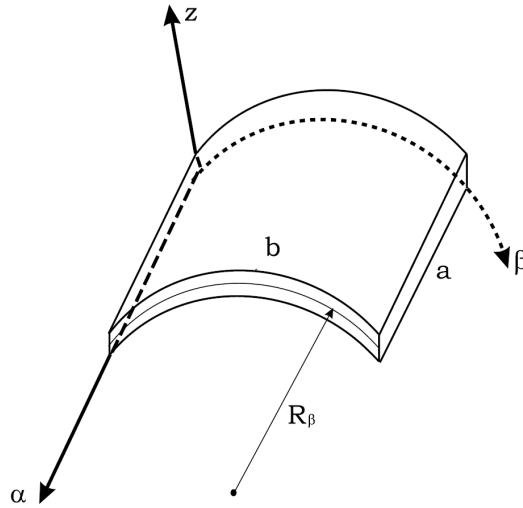


Figure 5.1. Geometry and reference system for cylindrical shell.

A laminated shell composed of N_l layers is considered. The integer k , used as superscript or subscript, indicates each layer starting from the shell bottom. The layer geometry is denoted by the same symbols as those used for the whole multilayered shell and vice-versa. α_k and β_k are the curvilinear orthogonal co-ordinates (coinciding with lines of principal curvature) on the layer reference surface Ω_k (middle surface of the k -layer). z_k denotes the rectilinear co-ordinate measured along the normal direction to Ω_k .

The following relations hold in the orthogonal system of coordinates above described:

$$\begin{aligned} ds_k^2 &= H_\alpha^k d\alpha^2 + H_\beta^k d\beta^2 + H_z^k dz^2 \\ d\Omega_k &= H_\alpha^k H_\beta^k d\alpha_k d\beta_k \\ dV &= H_\alpha^k H_\beta^k H_z^k d\alpha_k d\beta_k dz_k \end{aligned} \quad (5.1)$$

where ds_k^2 is the square of line element, $d\Omega_k$ is the area of an infinitesimal rectangle on Ω_k and dV is an infinitesimal volume. Here

$$\begin{aligned} H_\alpha^k &= A^k \left(1 + z_k/R_\alpha^k\right) \\ H_\beta^k &= A^k \left(1 + z_k/R_\beta^k\right), H_z^k = 1. \end{aligned} \quad (5.2)$$

R_α^k and R_β^k are the radii of curvature along the two in-plane directions α_k and β_k respectively. A^k and B^k are the coefficients of the first fundamental form of Ω_k [61]. For shells with constant curvature these coefficients are equal to unity.

5.3 Overview of the considered Shell Theories

Since a large variety of two-dimensional theories can be formulated on the basis of different kinematic assumptions, it may be useful to recall some details of the theories considered in this chapter.

5.3.1 Classical theories

Classical Lamination Theory

Shells' Classical Lamination Theory (CLT) is based on Love-Kirchhoff's kinematic assumptions [66]. The relative displacements model can be written as follow:

$$\begin{aligned} u_q(\alpha, \beta, z) &= u_{q0}(\alpha, \beta) - z u_{z0,q} \quad q = \alpha, \beta \\ u_z(\alpha, \beta, z) &= u_{z0}(\alpha, \beta) \end{aligned} \quad (5.3)$$

that is, normals to the reference surface remain normal, straight and unstrained after deformation. Subscript '0' denotes the variable value in correspondence to the reference surface Ω . Subscripts preceded by comma represent spatial derivation. The transverse shear and the through-the-thickness deformations are discarded. The corresponding stresses can be obtained 'a posteriori' upon integration of the indefinite equilibrium equations, see Carrera [22]. Poisson's locking is corrected via the assumption of reduced stiffness coefficients in Hooke's law as derived from the assumption of a plane stress state (see Carrera and Brischetto [29, 28]).

First Order Shear Deformation Theory

Mindlin [74] postulated a kinematic field that accounts for constant transverse shear strain components along the thickness, whereas the normal deformation is neglected. Such a

model is known as First Order Shear Deformation Theory (FSDT):

$$\begin{aligned} u_q(\alpha, \beta, z) &= u_{q0}(\alpha, \beta) + zu_{q1}(\alpha, \beta) \quad q = \alpha, \beta \\ u_z(\alpha, \beta, z) &= u_{z0}(\alpha, \beta) \end{aligned} \quad (5.4)$$

As for CLT, more accurate results can be obtained upon ‘a posteriori’ integration of the indefinite equilibrium equations.

5.3.2 Higher Order Theories

According to Koiter [60] statement: “... a refinement of Love’s first approximation theory is indeed meaningless, in general, unless the effects of transverse shear and normal stresses are taken into account at the same time”, Higher Order Theories (HOTs) can be formulated adopting the following expansion for displacements variables \mathbf{u} :

$$\begin{aligned} u_q(\alpha, \beta, z) &= u_{q0}(\alpha, \beta) + z^r u_{qr}(\alpha, \beta) \\ q &= \alpha, \beta, z \quad r = 1, 2, \dots, N \end{aligned} \quad (5.5)$$

The summing convention for repeated indexes has been adopted. N is the order of expansion and it is a free parameter. In the following, an approximation order as high as 4 is considered. A N -order theory based upon Eq. 5.5 is addressed as ‘EDN’. Letter ‘E’ denotes that the kinematic is preserved for the whole layers of the shell, as in the so-called Equivalent Single Layer (ESL) approach. ‘D’ indicates that only displacement unknowns are used. ‘N’ stands for the expansion order of the through-the-thickness polynomial approximation. For instance, the displacement field of an ED3 model is:

$$\begin{aligned} u_\alpha &= u_{\alpha0} + zu_{\alpha1} + z^2 u_{\alpha2} + z^3 u_{\alpha3} \\ u_\beta &= u_{\beta0} + zu_{\beta1} + z^2 u_{\beta2} + z^3 u_{\beta3} \\ u_z &= u_{z0} + zu_{z1} + z^2 u_{z2} + z^3 u_{z3} \end{aligned} \quad (5.6)$$

This theory accounts for a parabolic and cubic variation along the thickness of transverse normal and shear strains, respectively. If transverse normal strain is discarded the previous theory becomes:

$$\begin{aligned} u_q(\alpha, \beta, z) &= u_{q0}(\alpha, \beta) + z^r u_{qr}(\alpha, \beta) \\ q &= \alpha, \beta \quad r = 1, 2, \dots, N \\ u_z(\alpha, \beta, z) &= u_{z0}(\alpha, \beta) \end{aligned} \quad (5.7)$$

and is denoted as ‘EDNd’.

HOTs including Zig-Zag Effect

Laminate structures are characterized by a change in slope of displacements and transverse normal and shear stresses at layer interfaces. These quantities are C^0 class function of the transverse coordinate. EDN and EDNd models are based on C^∞ functions in z and, therefore, are intrinsically incapable to describe this zig-zag variation. This latter can be accounted for within an ESL approach via Murakami’s function $M(\zeta_k)$ (see Murakami [76] and Carrera [27]):

$$M(\zeta_k) = (-1)^k \zeta_k \quad (5.8)$$

where k counts the laminae, h_k stands for the thickness of a k -layer and $\zeta_k = z_k/2h_k$ such that $-1 \leq \zeta_k \leq 1$, being z_k a k -layer local coordinate. The following properties hold: a) $M(\zeta_k)$ is a piece-wise linear function of the local coordinate z_k , b) its slope assumes opposite sign between two adjacent layers. The kinematic field including Murakami's function is:

$$\begin{aligned} u_q(\alpha, \beta, z) &= u_{q0}(\alpha, \beta) + z^r u_{qr}(\alpha, \beta) + \\ &+ (-1)^k \zeta_k u_{qN+1}(\alpha, \beta) \end{aligned} \quad (5.9)$$

$$q = \alpha, \beta, z \quad r = 1, 2, \dots, N$$

A model based on Murakami's function is addressed as 'EDZN'. Other possible manners of modeling the zig-zag variation are reported in Carrera [25].

5.3.3 Layer-Wise Theories

Multi-layered shells can be analyzed by independent kinematic assumptions for each layer. According to Reddy [97], this approach is stated as Layer-Wise (LW). In order to satisfy the compatibility of the displacement field, a MacLaurin's expansion across the thickness, typical of ESL models, is not convenient. Interface values should be rather assumed as unknown variables. The following expansion is, therefore, adopted:

$$\begin{aligned} u_q^k &= F_t u_{qt}^k + F_b u_{qb}^k + F_r u_{qr}^k \\ q &= \alpha, \beta, z \quad r = 2, 3, \dots, N \quad k = 1, 2, \dots, N_l \end{aligned} \quad (5.10)$$

N_l represents the total number of layers. Subscripts 't' and 'b' denote values evaluated at top and bottom surface of a k -layer, respectively. The thickness functions F_t , F_b and F_r depend on ζ_k . They are defined as follows:

$$\begin{aligned} F_t &= \frac{P_0 + P_1}{2} \quad F_b = \frac{P_0 - P_1}{2} \quad F_r = P_r - P_{r-2} \\ r &= 2, 3, \dots, N \end{aligned} \quad (5.11)$$

$P_j = P_j(\zeta_k)$ is a Legendre's polynomials of order j . The first four Legendre's polynomials are:

$$\begin{aligned} P_0 &= 1 \quad P_1 = \zeta_k \quad P_2 = \frac{3\zeta_k^2 - 1}{2} \\ P_3 &= \frac{5\zeta_k^3}{2} - \frac{3\zeta_k}{2} \quad P_4 = \frac{35\zeta_k^4}{8} - \frac{15\zeta_k^2}{4} + \frac{3}{8} \end{aligned} \quad (5.12)$$

The following properties hold:

$$\begin{aligned} \zeta_k = 1 : \quad &F_t = 1, \quad F_b = 0, \quad F_r = 0 \\ \zeta_k = -1 : \quad &F_t = 0, \quad F_b = 1, \quad F_r = 0 \end{aligned} \quad (5.13)$$

Top and bottom displacements of each lamina are assumed as unknown variable. Inter-laminar compatibility of displacements can be easily linked:

$$u_{qt}^k = u_{qb}^{(k+1)} \quad q = \alpha, \beta, z \quad k = 1, 2, \dots, N_l - 1 \quad (5.14)$$

The acronym used for these theories is 'LDN', where 'L' stands for the LW approach. For all the models that has been previously described, the governing equations and the boundary conditions are derived via the Principle of Virtual Displacement (PVD) in Sec. 5.4.

5.3.4 Mixed Theories based on Reissner's Mixed Variational Theorem

The kinematics described previously does not satisfy the interlaminar continuity of transverse shear and normal stresses. It can be fulfilled 'a priori' assuming transverse shear and normal stresses together with displacements as primary variables by means of Reissner's Mixed Variational Theorem [101, 102] (RMVT). Transverse stresses $\sigma_{\alpha z}^k$, $\sigma_{\beta z}^k$ and $\sigma_{\alpha z}^k$ are approximated via the same model as that addressed in Eq. 5.10:

$$\begin{aligned} \sigma_{qz}^k &= F_t \sigma_{qzt}^k + F_b \sigma_{qzb}^k + F_r \sigma_{qzr}^k \\ q &= \alpha, \beta, z \quad r = 2, 3, \dots, N \quad k = 1, 2, \dots, N_l \end{aligned} \quad (5.15)$$

The interlaminar continuity is imposed straightforwardly:

$$\sigma_{qzt}^k = \sigma_{qzb}^{(k+1)} \quad q = \alpha, \beta, z \quad k = 1, 2, \dots, N_l - 1 \quad (5.16)$$

This group of models is denoted by 'LMN'. 'M' means mixed models based on RMVT.

5.3.5 Carrera Unified Formulation

Carrera's Unified Formulation (UF) allows several two dimensional models to be obtained for shells, thanks to the separation of the unknown variables into a set of thickness functions only depending on the thickness coordinate z , and the correspondent unknowns depending on the in-plane coordinates (α, β) . In force of that the considered theories can be all unified considering that CLT and FSDT are a peculiar case of ESL higher order models. These latter models can be regarded as a particular case of LW models in which the number of layers is equal to one and the through-the-thickness polynomial approximation is performed via the classical base $\{z^r : r = 0, 1, \dots, N\}$. In the case of EDZN models, Murakami's function is also considered. Eqs. 5.3, 5.4, 5.5, 5.9, and 5.10 can be unified into the following compact notation:

$$\begin{aligned} u_q^k &= F_\tau u_{q\tau}^k \quad q = \alpha, \beta, z \quad \tau = t, b, r, \\ \sigma_{qz}^k &= F_\tau \sigma_{qz\tau}^k \quad r = 2, 3, \dots, N \\ k &= 1, 2, \dots, N_l \end{aligned} \quad (5.17)$$

The governing equations are derived according to the chosen variational statement (either PVD or RMVT) in a general way that does not depend upon the approximation approach (ESL or LW) and the polynomial expansion order.

5.4 Governing Equations

The displacement approach is formulated in terms of \mathbf{u}^k by variational imposing the equilibrium via PVD. In the dynamic case, this establishes:

$$\begin{aligned} \sum_{k=1}^{N_l} \int \int_{\Omega_k h_k} (\delta \epsilon_p^{kT} \sigma_p^k + \delta \epsilon_n^{kT} \sigma_n^k) dz_k d\Omega_k &= \\ = \sum_{k=1}^{N_l} \int \int_{\Omega_k h_k} \rho^k \delta \mathbf{u}^k \ddot{\mathbf{u}}^k dV & \end{aligned} \quad (5.18)$$

$$\begin{aligned} \boldsymbol{\epsilon}_p &= \begin{Bmatrix} \epsilon_{\alpha\alpha} \\ \epsilon_{\beta\beta} \\ \epsilon_{\alpha\beta} \end{Bmatrix} & \boldsymbol{\epsilon}_n &= \begin{Bmatrix} \epsilon_{\alpha z} \\ \epsilon_{\beta z} \\ \epsilon_{zz} \end{Bmatrix} \\ \boldsymbol{\sigma}_p &= \begin{Bmatrix} \sigma_{\alpha\alpha} \\ \sigma_{\beta\beta} \\ \sigma_{\alpha\beta} \end{Bmatrix} & \boldsymbol{\sigma}_n &= \begin{Bmatrix} \sigma_{\alpha z} \\ \sigma_{\beta z} \\ \sigma_{zz} \end{Bmatrix} \end{aligned} \quad (5.19)$$

‘T’ as superscript stands for the transposition operator. δ signifies virtual variations and ρ^k denotes mass density. The variation of the internal work has been split into in-plane and out-of-plane parts and involves the stress obtained from Hooke’s Law and the strain from the geometrical relations. Geometrical relations link strains $\boldsymbol{\epsilon}$ and displacements \mathbf{u} . Strains are conveniently grouped into in-plane and normal components denoted by the subscripts p and n, respectively. The geometric relations are:

$$\begin{aligned} \boldsymbol{\epsilon}_p^k &= \mathbf{D}_p \mathbf{u}^k + \mathbf{A}_p \mathbf{u}^k \\ \boldsymbol{\epsilon}_n^k &= \mathbf{D}_{n\Omega} \mathbf{u}^k + \lambda_D \mathbf{A}_n \mathbf{u}^k + \mathbf{D}_{nz} \mathbf{u}^k \end{aligned} \quad (5.20)$$

in which \mathbf{D}_p , $\mathbf{D}_{n\Omega}$, and \mathbf{D}_{nz} are differential matrix operators and \mathbf{A}_p and \mathbf{A}_n are geometrical terms accounting for the through-the-thickness variation of the curvature:

$$\begin{aligned} \mathbf{D}_p &= \begin{bmatrix} \frac{1}{H_\alpha^k} \frac{\partial}{\partial \alpha} & 0 & 0 \\ 0 & \frac{1}{H_\beta^k} \frac{\partial}{\partial \beta} & 0 \\ \frac{1}{H_\beta^k} \frac{\partial}{\partial \beta} & \frac{1}{H_\alpha^k} \frac{\partial}{\partial \alpha} & 0 \end{bmatrix}, & \mathbf{A}_p &= \begin{bmatrix} 0 & 0 & \frac{1}{H_\alpha^k R_\alpha^k} \\ 0 & 0 & \frac{1}{H_\beta^k R_\beta^k} \\ 0 & 0 & 0 \end{bmatrix} \\ \mathbf{D}_{n\Omega} &= \begin{bmatrix} 0 & 0 & \frac{1}{H_\alpha^k} \frac{\partial}{\partial \alpha} \\ 0 & 0 & \frac{1}{H_\beta^k} \frac{\partial}{\partial \beta} \\ 0 & 0 & 0 \end{bmatrix}, & \mathbf{A}_n &= \begin{bmatrix} -\frac{1}{H_\alpha^k R_\alpha^k} & 0 & 0 \\ 0 & -\frac{1}{H_\beta^k R_\beta^k} & 0 \\ 0 & 0 & 0 \end{bmatrix} \\ \mathbf{D}_{nz} &= \begin{bmatrix} \frac{\partial}{\partial z} & 0 & 0 \\ 0 & \frac{\partial}{\partial z} & 0 \\ 0 & 0 & \frac{\partial}{\partial z} \end{bmatrix} \end{aligned} \quad (5.21)$$

H_α^k and H_β^k account for the change in length of a k -layer segment due to the curvature. λ_D is a trace operator, it has been introduced to identify terms that are neglected in the Donnell-type shallow shell theories.

The aim of this part is to evaluate the effect of a second class of shell theories derived from approximations on curvature terms in the strain-displacement relations. It can be shown, see Kraus [61] that by putting $\lambda_D = 0$, the shell curvature becomes that of the

corresponding plate as it is in Donnell- type approximation theory. Donnell's approximation is strongly related to the geometrical parameter a/R_α and b/R_β .

Love's shell theory is instead related to the following approximation for the coefficients of the second fundamental form (see Eq. 5.1) of the shell:

$$H_\alpha = H_\beta = 1 \quad (5.22)$$

It appears evident that Love's approximation is related to the shell parameter h/R_α and h/R_β , where h is the shell thickness.

In the case of linear elastic material, stresses and strains are related via Hooke's generalized law:

$$\begin{aligned} \boldsymbol{\sigma}_p^k &= \tilde{\mathbf{C}}_{pp}^k \boldsymbol{\epsilon}_p^k + \tilde{\mathbf{C}}_{pn}^k \boldsymbol{\epsilon}_n^k \\ \boldsymbol{\sigma}_n^k &= \tilde{\mathbf{C}}_{np}^k \boldsymbol{\epsilon}_p^k + \tilde{\mathbf{C}}_{nn}^k \boldsymbol{\epsilon}_n^k \end{aligned} \quad (5.23)$$

Terms $\tilde{\mathbf{C}}_{pp}^k$, $\tilde{\mathbf{C}}_{pn}^k$, $\tilde{\mathbf{C}}_{np}^k$ and $\tilde{\mathbf{C}}_{nn}^k$ are the material stiffness matrices for a k -layer in the global reference system, see Carrera [26]. By replacing Eqs. 5.23, 5.20 and the unified displacement field in Eq. 5.17. into Eq. 5.18, PVD reads:

$$\begin{aligned} & \sum_{k=1}^{N_l} \int_{\Omega_k} \delta \mathbf{u}_\tau^{kT} \int_{h_k} \{ (-F_\tau \mathbf{D}_p^T + F_\tau \mathbf{A}_p^T) [\tilde{\mathbf{C}}_{pp}^k (F_s \mathbf{D}_p + \\ & + F_s \mathbf{A}_p) + \tilde{\mathbf{C}}_{pn}^k (F_s \mathbf{D}_{n\Omega} + F_s \mathbf{A}_n + F_{s,z})] + \\ & + (-F_\tau \mathbf{D}_{n\Omega}^T + F_\tau \mathbf{A}_n^T + F_{\tau,z}) [\tilde{\mathbf{C}}_{np}^k (F_s \mathbf{D}_p + F_s \mathbf{A}_p) + \\ & + \tilde{\mathbf{C}}_{nn}^k (F_s \mathbf{D}_{n\Omega} + F_s \mathbf{A}_n + F_{s,z})] \} H_\alpha^k H_\beta^k dz_k \mathbf{u}_s^k d\Omega_k + \\ & + \sum_{k=1}^{N_l} \int_{\Gamma_k} \delta \mathbf{u}_\tau^{kT} \int_{h_k} \{ F_\tau \mathbf{I}_p^T [\tilde{\mathbf{C}}_{pp}^k (F_s \mathbf{D}_p + F_s \mathbf{A}_p) + \\ & + \tilde{\mathbf{C}}_{pn}^k (F_s \mathbf{D}_{n\Omega} + F_s \mathbf{A}_n + F_{s,z})] + \\ & + F_\tau \mathbf{I}_{n\Omega}^T [\tilde{\mathbf{C}}_{np}^k (F_s \mathbf{D}_p + F_s \mathbf{A}_p) + \tilde{\mathbf{C}}_{nn}^k (F_s \mathbf{D}_{n\Omega} \\ & + F_s \mathbf{A}_n + F_{s,z})] \} H_\alpha^k H_\beta^k dz_k \mathbf{u}_s^k d\Gamma_k = \\ & = \sum_{k=1}^{N_l} \int_{\Omega_k} \delta \mathbf{u}_\tau^{kT} \rho^k F_\tau F_s \ddot{\mathbf{u}}^k \end{aligned} \quad (5.24)$$

being:

$$\mathbf{I}_p = \begin{bmatrix} \frac{1}{H_\alpha^k} & 0 & 0 \\ 0 & \frac{1}{H_\beta^k} & 0 \\ \frac{1}{H_\beta^k} & \frac{1}{H_\alpha^k} & 0 \end{bmatrix} \quad \mathbf{I}_{n\Omega} = \begin{bmatrix} 0 & 0 & \frac{1}{H_\alpha^k} \\ 0 & 0 & \frac{1}{H_\beta^k} \\ 0 & 0 & 0 \end{bmatrix} \quad (5.25)$$

By assigning the definition of virtual variations for the unknown displacement variables, the differential system of governing equations and related boundary conditions for the N_l

k -layers in each Ω_k domain are found. The equilibrium and compatibility equations are:

$$\mathbf{K}_d^{k\tau s} \mathbf{u}_s^k = \mathbf{M}^{k\tau s} \ddot{\mathbf{u}}_s^k \quad (5.26)$$

with boundary conditions

$$\begin{aligned} \mathbf{u}_\tau^k &= \bar{\mathbf{u}}_\tau^k && \text{geometrical on } \Gamma_k^g \\ \mathbf{\Pi}_d^{k\tau s} \mathbf{u}_s^k &= \mathbf{\Pi}_d^{k\tau s} \bar{\mathbf{u}}_s^k && \text{mechanical on } \Gamma_k^m \end{aligned} \quad (5.27)$$

Differential stiffness, inertia and mechanical boundary conditions matrices are:

$$\begin{aligned} \mathbf{K}_d^{k\tau s} &= \int_{h_k} \{(-F_\tau \mathbf{D}_p^T + F_\tau \mathbf{A}_p^T) [\tilde{\mathbf{C}}_{pp}^k (F_s \mathbf{D}_p + \\ &+ F_s \mathbf{A}_p) + \tilde{\mathbf{C}}_{pn}^k (F_s \mathbf{D}_{n\Omega} + F_s \mathbf{A}_n + F_{s,z})] + \\ &+ (-F_\tau \mathbf{D}_{n\Omega}^T + F_\tau \mathbf{A}_n^T + F_{\tau,z}) [\tilde{\mathbf{C}}_{np}^k (F_s \mathbf{D}_p + \\ &+ F_s \mathbf{A}_p) + \tilde{\mathbf{C}}_{nn}^k (F_s \mathbf{D}_{n\Omega} + F_s \mathbf{A}_n + F_{s,z})]\} H_\alpha^k H_\beta^k dz_k \end{aligned} \quad (5.28)$$

$$\mathbf{M}^{k\tau s} = \int_{h_k} \rho^k F_\tau F_s \mathbf{I} H_\alpha^k H_\beta^k dz_k \quad (5.29)$$

$$\begin{aligned} \mathbf{\Pi}_d^{k\tau s} &= \int_{h_k} \{F_\tau \mathbf{I}_p^T [\tilde{\mathbf{C}}_{pp}^k (F_s \mathbf{D}_p + F_s \mathbf{A}_p) + \\ &+ \tilde{\mathbf{C}}_{pn}^k (F_s \mathbf{D}_{n\Omega} + F_s \mathbf{A}_n + F_{s,z})] + \\ &+ F_\tau \mathbf{I}_{n\Omega}^T [\tilde{\mathbf{C}}_{np}^k (F_s \mathbf{D}_p + F_s \mathbf{A}_p) + \\ &+ \tilde{\mathbf{C}}_{nn}^k (F_s \mathbf{D}_{n\Omega} + F_s \mathbf{A}_n + F_{s,z})]\} H_\alpha^k H_\beta^k dz_k \end{aligned} \quad (5.30)$$

\mathbf{I} is the unit array. Eq. 5.26 is solved via a Navier-type solution upon assumption of the following harmonic form for the unknown displacements:

$$\begin{aligned} (u_\alpha^k) &= \sum_{m=1}^{\bar{m}} \sum_{n=1}^{\bar{n}} (U_\alpha^k(z)) \cos\left(\frac{m\pi}{a}\alpha\right) \sin\left(\frac{n\pi}{b}\beta\right) e^{i\omega_{mn}t} \\ (u_\beta^k) &= \sum_{m=1}^{\bar{m}} \sum_{n=1}^{\bar{n}} (U_\beta^k(z)) \sin\left(\frac{m\pi}{a}\alpha\right) \cos\left(\frac{n\pi}{b}\beta\right) e^{i\omega_{mn}t} \\ (u_z^k) &= \sum_{m=1}^{\bar{m}} \sum_{n=1}^{\bar{n}} (U_z^k(z)) \sin\left(\frac{m\pi}{a}\alpha\right) \sin\left(\frac{n\pi}{b}\beta\right) e^{i\omega_{mn}t} \end{aligned} \quad (5.31)$$

where a and b are the lengths of the shell along the two coordinates α and β . m and n represent the number of half-waves in α and β direction, respectively. These numbers characterize the vibration mode associated to the circular frequency ω_{mn} . $i = \sqrt{-1}$ is the imaginary unit and t the time. Capital letters indicate maximal amplitudes. These assumptions correspond to the simply-supported boundary conditions. Upon substitution

of Eq. 5.31, the governing equations assume the form of a linear system of algebraic equations in the time domain:

$$\mathbf{K}^* \hat{\mathbf{U}} = -\omega_{mn}^2 \mathbf{M} \hat{\mathbf{U}} \quad (5.32)$$

where \mathbf{K}^* is the equivalent stiffness matrix obtained by means of static condensation (for further details see Carrera [19, 21]), \mathbf{M} is the inertial matrix and $\hat{\mathbf{U}}$ is the vector of unknown variables. By defining $\lambda_{mn} = -\omega_{mn}^2$, the solution of the associated eigenvalue problem becomes:

$$||\mathbf{K}^* - \lambda_{mn} \mathbf{M}|| = 0 \quad (5.33)$$

The eigenvectors $\hat{\mathbf{U}}$ associated to the eigenvalues λ_{mn} (or to circular frequencies ω_{mn}) define the vibration modes of the structure in terms of primary variables. Once the wave numbers (m, n) have been defined in the in-plane directions, the number of obtained frequencies becomes equal to the degrees of freedom of the employed two-dimensional model. It is possible to obtain the relative eigenvector, in terms of primary variables, for each value of frequency, in order to plot the modes in the thickness direction.

5.5 Results

The free vibration response and the effect of various through the thickness and curvature approximations in multilayered orthotropic cylindrical composite shells are evaluated through a comparison of several, significant shell theories. Refined theories with up to fourth-order displacement field for both in-plane and transverse displacements, and two approaches for modelling variables (ESL, equivalent single layer and LW, Layer Wise) are compared to evaluate the free vibration response of cylindrical and spherical shells. The UF is employed to derive shell equations that are solved for the case of simply supported boundary conditions and doubly curved shells with constant curvatures. Navier-type closed form solution are obtained. Love's and Donnell's approximations are compared in the framework of higher order theories and classical ones. Parametric analysis have been carried out since the behaviour of laminated composite shells made of high-modulus and low-density materials are strongly dependent of the degree of orthotropy of the individual layer, the stacking sequence of laminates and the thickness parameter of the shells. Unless otherwise specified, the mechanical material properties of the lamina are those used by Pagano [84]: $E_L = 25E_T$, $G_{LT} = 0.5E_T$, $G_{TT} = 0.2E_T$, $\nu_{LT} = \nu_{TT} = 0.25$, $\rho = 1.0$, $\chi = 1.0$. Subscript 'L' stands for direction parallel to the fibres, 'T' identifies the transverse direction, ν_{LT} is the major Poisson ratio, ρ denotes the density, and χ the shear correction factor. $\chi = 5/6$ is adopted in $FSDT^{5/6}$ theory. The fibre orientation of the different laminae alternate between 0 and 90 *deg* with respect to the α -axis. Both symmetric and antisymmetric laminations with respect to the middle surface are considered. Cylindrical shell geometry have been studied using the side-to-thickness parameter $a/h = 10$, whereas the other geometric features are specified in each case. All the numerical results are shown as the dimensionless quantity:

$$\bar{\omega} = \omega \times a^2 \sqrt{\rho/h^2 E_T} \quad (5.34)$$

The analysis were carried out in order to investigate the effects on the natural frequencies and the accuracy of the UF two-dimensional models with respect to Love's and Donnell's approximation theories.

5.5.1 Assessment

Firstly, an assessment of the present solutions with results from literature is presented. A comparison with the exact solution by Ye and Soldatos [131] has been provided in Table 5.1. The superscript accompanying exact numerical results in Table 5.1 indicates

R_β/a	5	10	50	100
<i>Exact</i>	10.305 ¹⁴	10.027 ²²	9.834 ²⁴	9.815 ²
— <i>Present analysis</i>				
<i>LM4</i>	10.305	10.027	9.834	9.815
<i>LM3</i>	10.305	10.027	9.834	9.815
<i>LM2</i>	10.306	10.027	9.835	9.816
<i>LM1</i>	10.324	10.046	9.855	9.836
<i>LD4</i>	10.305	10.027	9.834	9.815
<i>LD3</i>	10.305	10.027	9.834	9.815
<i>LD2</i>	10.307	10.028	9.835	9.816
<i>LD1</i>	10.368	10.091	9.899	9.880
<i>ED4</i>	10.453	10.178	9.987	9.969
<i>ED3</i>	10.453	10.179	9.988	9.969
<i>ED2</i>	11.291	11.040	10.86	10.84
<i>ED1</i>	11.294	11.043	10.86	10.85
<i>EDZ3</i>	10.307	10.030	9.837	9.819
<i>EDZ2</i>	10.367	10.090	9.898	9.879
<i>EDZ1</i>	10.383	10.104	9.908	9.890
<i>FSDT</i> ^{5/6}	10.958	10.698	10.51	10.50
<i>FSDT</i>	11.295	11.044	10.86	10.85
<i>CLT</i>	13.708	13.507	13.35	13.33

Table 5.1. Comparison of present analysis with available reference solution for $[0/90_{2t}/0]$ cylindrical shell. Values of $\bar{\omega}$ for $a/h = 10$, $m = 1$, n given in superscripts.

the circumferential wave number, n , for which the fundamental frequency was detected. In the case that corresponding results values were obtained for the same value of n such a superscript is omitted. A three-layered, moderately thick cylindrical ringed shell $[0/90_{2t}/0]$ has been considered, where the subscript $2t$ means $h_1 = h_3 = h_2/2$ (h_i is the thickness of each lamina, $i = 1, 2, 3$). Mixed theories solutions match the exact one and accordance is still verified even for the lowest order theory LM1. Furthermore, LW4 accuracy is confirmed. Concerning ESLM, it should be noted that the higher-order theory ED4 can

R_β/a	1	2	5	10	20	∞
<i>YS</i> [131]	10.697	9.4951	9.4951	8.9778	8.9778	8.9248
<i>B</i> [13]	10.409	9.3627	9.0200	8.9564	8.9341	8.9179
<i>Q</i> [93]	10.666	9.4577	9.0286	8.9479	8.9199	8.9001
— <i>Present analysis</i>						
<i>LM4</i>	10.698	9.4936	9.0598	8.9759	8.9460	8.9241
<i>LM3</i>	10.698	9.4936	9.0598	8.9759	8.9460	8.9241
<i>LM2</i>	10.714	9.5123	9.0791	8.9953	8.9653	8.9434
<i>LM1</i>	10.734	9.5230	9.0841	8.9986	8.9679	8.9452
<i>LD4</i>	10.698	9.4936	9.0598	8.9759	8.9460	8.9241
<i>LD3</i>	10.698	9.4937	9.0598	8.9759	8.9460	8.9241
<i>LD2</i>	10.735	9.5384	9.1066	9.0229	8.9929	8.9709
<i>LD1</i>	10.785	9.5920	9.1612	9.0774	9.0474	9.0252
<i>ED4</i>	10.721	9.5219	9.0892	9.0054	8.9755	8.9536
<i>ED3</i>	10.765	9.5656	9.1322	9.0479	9.0177	8.9955
<i>ED2</i>	10.785	9.5920	9.1612	9.0774	9.0474	9.0252
<i>ED1</i>	10.721	9.5190	9.0857	9.0019	8.9719	8.9500
<i>EDZ3</i>	10.729	9.5275	9.0946	9.0109	8.9810	8.9592
<i>EDZ2</i>	10.769	9.5705	9.1379	9.0540	9.0239	9.0018
<i>EDZ1</i>	10.744	9.5529	9.1302	9.0500	9.0219	9.0017
<i>FSDT</i> ^{5/6}	10.668	9.4582	9.0287	8.9479	8.9199	8.9001
<i>FSDT</i>	10.751	9.5564	9.1309	9.0502	9.0219	9.0017
<i>CLT</i>	11.225	10.105	9.6992	9.6184	9.5887	9.5661

Table 5.2. Comparison of present analysis with available reference solution for [90/0] cylindrical shell. Values of $\bar{\omega}$ for $a/h = 10$, $a/b = 1$, $m = n = 1$, $\nu_{12} = 0.25$, $\nu_{13} = 0.03$, $\nu_{23} = 0.4$.

lead to poorer results than EDZ3 and EDZ2. Because of the different continuity conditions of displacement components at the interface between the layers the layer-wise theories results always more accurate then the equivalent single-layer theories. Fine results with respect to standard classical displacement formulation are found. Refined theories lead to lower values of $\bar{\omega}$ according to the related reduction in stiffness. A second assessment analysis is carried out considering a two layer [90/0] cylindrical shell. The fundamental frequency parameter $\bar{\omega}$ is shown in Table 5.2 and compared with corresponding results by Ye and Soldatos [131], Bhimaraddi [13] and Qatu [93]. The shell has equal axial and circumferential lengths and 0 *deg* outer layer. Similar consideration to that made for Table 5.1 about the accuracy of the proposed theories are valid also in this case.

5.5.2 Influence of the degree of orthotropy

Fundamental frequencies parameters computed via the UF two-dimensional models are presented in Table 5.3 for several values of the degree of orthotropy of the single layer.

E_L/E_T	3	10	25	40
$R_\beta/h = 4$				
<i>CLT</i>	18.095	20.896	25.447	29.202
<i>FSDT</i>	16.680	18.841	21.741	23.729
<i>FSDT</i> ^{5/6}	16.437	18.505	21.201	23.009
<i>ED1</i>	17.167	18.792	21.691	23.670
<i>ED4</i>	16.520	18.494	20.974	22.575
<i>EDZ1</i>	16.906	18.765	21.134	22.649
<i>EDZ3</i>	16.348	18.335	20.779	22.323
<i>LD2</i>	16.352	18.345	20.799	22.351
<i>LD4</i>	16.345	18.317	20.690	22.151
<i>LM2</i>	16.350	18.329	20.718	22.193
<i>LM4</i>	16.345	18.317	20.690	22.151
$R_\beta/h = 100$				
<i>CLT</i>	5.0841	9.0638	14.205	17.864
<i>FSDT</i>	4.9462	8.3217	11.748	13.576
<i>FSDT</i> ^{5/6}	4.9200	8.1951	11.400	13.051
<i>ED1</i>	4.9387	8.3177	11.746	13.574
<i>ED4</i>	4.8851	8.0322	10.989	12.471
<i>EDZ1</i>	4.9394	7.9805	10.819	12.240
<i>EDZ3</i>	4.8548	7.9065	10.700	12.084
<i>LD2</i>	4.8548	7.9070	10.702	12.089
<i>LD4</i>	4.8546	7.9059	10.698	12.081
<i>LM2</i>	4.8548	7.9065	10.700	12.085
<i>LM4</i>	4.8546	7.9059	10.698	12.081

Table 5.3. Effect of degree of orthotropy of the individual layers E_L/E_T on $\bar{\omega}$ of three layers [0/90/0] symmetric cylindrical shells. $\gamma = \pi/3$, $m = 1$, $n = 1$.

E_L/E_T is considered to be as low as 3 and as high as 40. A symmetric [0/90/0] cross-ply laminated composite cylindrical shell is considered, with equal thickness of each lamina and $\gamma = \pi/3$. A deep moderately thick shell and a shallow thin one are considered, depending on the radii-to-thickness parameter $R_\beta/h = 4$ or $R_\beta/h = 100$, respectively. Considering the UF-two dimensional models, similar consideration made for the assessment can be done also for each analysis once the parameters are fixed. Results for $R_\beta/h = 100$ and $E_L/E_T = 3$ show that in this case classical theories lead to a good accuracy respect to the refined UF-two dimensional theories. The hypotheses at the base of classical theories are quite verified in this case. As E_L/E_T increases, the difference between classical theories

and higher-order ones becomes more significant. Analogous consideration can be done for the case $R_\beta/h = 4$, but here the error between classical theories and HOTs increases, as the thickness assumption is not verified. *CLT* gives higher values of $\bar{\omega}$ than *FSDT*s, whereas these last theories agree with HOTs, and this effect is more evident when the ratio E_L/E_T is low. The extreme case of highest degree of orthotropy and deep moderately thick shell yields to the most significant differences between classical theories and refined models.

5.5.3 Effect of the lamination sequence

The influence of the lamination sequence on the fundamental frequencies parameter $\bar{\omega}$ of cross-ply laminated composite shells with simply supported edges is presented in Tables 5.4 and 5.5.

	[0/90]	[0/90] ₂	[0/90] ₃	[0/90] ₄	[0/90] ₅
<i>CLT</i>	6.984	9.922	10.376	10.530	10.60
<i>FSDT</i>	6.714	8.987	9.299	9.402	9.449
<i>FSDT</i> ^{5/6}	6.665	8.834	9.127	9.223	9.266
<i>ED2</i>	6.707	8.956	9.283	9.393	9.443
<i>ED3</i>	6.686	8.687	9.050	9.181	9.242
<i>ED4</i>	6.675	8.571	9.038	9.179	9.241
<i>EDZ2</i>	6.703	8.758	9.076	9.184	9.233
<i>EDZ3</i>	6.686	8.441	8.831	8.972	9.037
<i>LD1</i>	6.714	8.448	8.812	8.944	9.005
<i>LD2</i>	6.694	8.397	8.785	8.928	8.995
<i>LD4</i>	6.665	8.395	8.785	8.927	8.995
<i>LM1</i>	6.671	8.407	8.791	8.931	8.997
<i>LM3</i>	6.665	8.395	8.785	8.927	8.995
<i>LM4</i>	6.665	8.395	8.785	8.927	8.995

Table 5.4. Effect of the stacking sequence of laminates on $\bar{\omega}$ of cross-ply anti-symmetric cylindrical shells. $\gamma = \pi/3$, $R_\beta/h = 100$, $m = 1$, $n = 1$.

All the layers have the same thickness. Both symmetric and anti-symmetric laminations with respect to the middle plane are considered. Compact notation is adopted to indicate the lamination sequence [55]. The first value in the sequence refers to the first layer of the laminate, starting from the bottom of the shell. In the symmetric laminates having an odd number of layers, the 0 *deg* layers are at the outer surfaces of the laminate. As the number of layer increases, results obtained via HOTs theories move away from those that come by classical theories. To remark the result obtained with *FSDT*^{5/6} and [0/90], that is practically the same achieved using refined theories, as LD4 and LM4. In fact a shear correction factor $\chi = 5/6$ means to correct the deficiencies of *FSDT* theory (non-parabolic variation of shear stresses and non-vanishing of the shear stresses at the

	$[0/90]_s$	$[0/90/0]_s$	$[0/90/0/90]_s$	$[0/90/0/90/0]_s$
<i>CLT</i>	14.205	13.030	12.437	12.084
<i>FSDT</i>	11.748	11.028	10.655	10.430
<i>FSDT</i> ^{5/6}	11.400	10.735	10.389	10.180
<i>ED1</i>	11.746	11.026	10.653	10.427
<i>ED2</i>	11.746	11.027	10.654	10.429
<i>ED3</i>	10.990	10.709	10.413	10.214
<i>ED4</i>	10.989	10.709	10.413	10.214
<i>EDZ1</i>	10.819	10.422	10.182	10.027
<i>EDZ2</i>	10.808	10.408	10.167	10.011
<i>EDZ3</i>	10.700	10.328	10.075	9.9084
<i>LD1</i>	10.810	10.362	10.087	9.9072
<i>LD2</i>	10.702	10.318	10.063	9.8930
<i>LD3</i>	10.698	10.317	10.063	9.8930
<i>LD4</i>	10.698	10.317	10.063	9.8930
<i>LM1</i>	10.751	10.334	10.071	9.8973
<i>LM2</i>	10.700	10.318	10.063	9.8930
<i>LM3</i>	10.698	10.317	10.063	9.8930
<i>LM4</i>	10.698	10.317	10.063	9.8930

Table 5.5. Effect of the stacking sequence of laminates on $\bar{\omega}$ of cross-ply symmetric cylindrical shells. $\gamma = \pi/3$, $R_\beta/h = 100$, $m = 1$, $n = 1$.

top and bottom surfaces of the shell), but still violates continuity requirement of the inter-laminar shear stresses. Usually a comparison between *EDZ3* and *ED4* theories, bring to better results for the first one. This trend is not verified in the case of $[0/90]$ lamination. When the number of layers is not high, for instance $N_L = 2$, *ED4* model yields more accurate results then *EDZ3* do. On the contrary, when the number of layer is high, the results achieved with *EDZ3* theory are definitively finer than the same obtained with higher-order theory *ED4*.

5.5.4 Influence of the Radius-to-Thickness ratio and Love's approximation

A three layers $[0/90_{2t}/0]$ composite shell with variable thickness parameter R_β/h is considered. An effective comparison of the effect of shear deformation, higher order shear deformation, through-the-thickness strain and Love's approximation could be conveniently built for such shell geometry. Fundamental frequency parameter $\bar{\omega}$ are compared in Tables 5.6 and 5.7.

R_β/h is considered to be as low as 2 and as high as 1000, going from a deep moderately thick shell to a shallow thin one. Two values of the number of waves n along the circumferential β direction are considered, whereas the axial wave number m is fixed to 1.

R_β/h	2	4	10	100	1000
<i>CLT</i>	107.22	31.879	15.493	13.678	13.330
<i>CLT</i> _{LOVE}	155.75	124.96	57.377	13.695	13.330
<i>FSDT</i>	63.693	25.841	13.367	11.289	10.846
<i>FSDT</i> _{LOVE}	63.384	25.818	13.372	11.289	10.846
<i>FSDT</i> ^{5/6}	59.855	25.011	13.077	10.956	10.496
<i>FSDT</i> _{LOVE} ^{5/6}	59.584	24.989	13.082	10.956	10.496
<i>ED4</i>	58.534	24.435	12.660	10.455	9.9688
<i>ED4</i> _{LOVE}	58.197	24.409	12.663	10.455	9.9688
<i>EDZ3</i>	58.658	24.362	12.545	10.313	9.8187
<i>EDZ3</i> _{LOVE}	58.261	24.334	12.548	10.313	9.8187
<i>LD4</i>	57.713	24.104	12.535	10.309	9.8154
<i>LD4</i> _{LOVE}	57.340	24.063	12.536	10.309	9.8154
<i>LM4</i>	57.688	24.103	12.535	10.309	9.8154
<i>LM4</i> _{LOVE}	57.312	24.062	12.536	10.309	9.8154

Table 5.6. Evaluation of Love effects in refined theories. Comparison on $\bar{\omega}$ of 0/90/0 multilayer composite shell. $E_L/E_T = 25$, $\gamma = \pi/3$, $m = 1$, $n = 1$.

R_β/h	2	4	10	100	1000
<i>CLT</i>	1078.0	543.64	240.53	14.877	13.336
<i>CLT</i> _{LOVE}	1076.2	543.43	240.52	16.491	13.336
<i>FSDT</i>	890.37	439.66	167.71	12.366	10.850
<i>FSDT</i> _{LOVE}	888.47	439.41	167.68	12.366	10.850
<i>FSDT</i> ^{5/6}	813.17	402.09	154.66	12.014	10.500
<i>FSDT</i> _{LOVE} ^{5/6}	811.44	401.86	154.65	12.014	10.500
<i>ED4</i>	686.84	402.27	154.46	11.519	9.9724
<i>ED4</i> _{LOVE}	701.12	404.69	154.44	11.519	9.9724
<i>EDZ3</i>	705.85	410.38	155.54	11.377	9.8222
<i>EDZ3</i> _{LOVE}	722.30	412.92	155.52	11.377	9.8222
<i>LD4</i>	640.58	394.39	153.67	11.367	9.8190
<i>LD4</i> _{LOVE}	651.53	396.45	153.65	11.367	9.8190
<i>LM4</i>	639.66	393.23	153.37	11.367	9.8190
<i>LM4</i> _{LOVE}	649.27	394.97	153.35	11.367	9.8190

Table 5.7. Evaluation of Love effects in refined theories. Comparison on $\bar{\omega}$ of 0/90/0 multilayer composite shell. $E_L/E_T = 25$, $\gamma = \pi/3$, $m = 1$, $n = 10$.

It is confirmed that the error of CLT increases as the thickness increases. Larger absolute errors are obtained from an increase of the circumferential wave number n . All the theories

match in the case of thin shells. Slight differences between LD4 and LM4 theories can be noticed for lower values of R_β/h , while the results agree when the radius-to-thickness parameter rises. This effect becomes more evident when the number of waves n increases. Love type approximations are significantly subordinate to the thickness parameter R_β/h . Tables 5.6 and 5.7 compares Love's approximation results with the exact (Flügge type ones). CLT, FSDT and fourth-order shell theories are considered for $n = 1$ and $n = 10$ waves numbers. Love's results match to exact solutions for high values of the thickness parameter. In fact in such cases the term H_β is almost equal to the unit.

5.5.5 Analysis of curvature parameter and Donnell effect

A three layer [0/90/0] deep moderately thick cylindrical shell with a variable span angle γ is considered. A comparison on $\bar{\omega}$ of curvature approximation through UF two-dimensional models is presented in Table 5.8.

γ	CLT	FSDT	ED1	ED4	EDZ1	EDZ3	LD2	LD4	LM2	LM4
$\pi/12$	248.90	147.36	147.36	140.36	144.40	140.81	140.61	138.72	138.95	138.66
$\pi/10$	202.31	117.94	117.93	112.46	115.42	112.76	112.79	111.15	111.40	111.12
$\pi/9$	169.54	103.16	103.14	98.476	100.93	98.689	98.784	97.307	97.555	97.290
$\pi/8$	138.38	88.387	88.352	84.509	86.488	84.631	84.764	83.483	83.715	83.473
$\pi/6$	82.756	59.240	59.174	56.921	58.056	56.882	57.010	56.209	56.374	56.206
$\pi/5$	59.380	45.292	45.219	43.650	44.423	43.548	43.645	43.105	43.224	43.105
$\pi/4$	39.898	32.400	32.332	31.294	31.744	31.142	31.199	30.903	30.972	30.902
$\pi/3$	25.447	21.741	21.691	20.974	21.134	20.779	20.799	20.690	20.718	20.690
$\pi/2$	17.963	15.891	15.871	15.320	15.270	15.121	15.120	15.104	15.109	15.104

Table 5.8. Evaluation of curvature approximation through Classical Vs Refined theories comparison on $\bar{\omega}$ of [0/90/0] cylindrical shells. $R_\beta/h = 4$, $m = 1$, $n = 1$.

As the span angle γ ranges from $\pi/12$ to $\pi/2$ the frequency parameter decreases, depending on the reduction in stiffness and the augment in mass of the structure analysed. Lower errors are found in the case of higher span angle γ , comparing classical theories with refined ones. In the case of $\gamma = \pi/12$, the aspect ratio of the shell is $a/b \approx 10$ and, therefore, the structure can be considered nearly one-dimensional. For this reason CLT, leads to relative errors of about 80% respect the higher-order theories reported in Table 5.8. Using a First Order Shear Deformation Theory this error falls to about 6%. Rather it cannot be notice any improvement from FSDT when a ED1 model is adopted. When $\gamma = \pi/2$ the aspect ratio of the shell is about 1.6 and therefore the error between classical theories and refined ones decrease significantly, due to the best two-dimensional approximation of the problem. Layer-wise second-order models provide good results, which are even better in the case of mixed formulation. Notable results are obtained adopting a EDZ3 model. In Tab 5.9 a comparison between Donnell type approximations and exact solutions (Flügge type ones), for Classical and Higher-Order shells theories is presented.

Two values of the radius-to-thickness parameter are reported considering a thin shallow

γ	CLT		FSDT		EDZ3		LD4		LM4	
	<i>Exact</i>	<i>Donnell</i>	<i>Exact</i>	<i>Donnell</i>	<i>Exact</i>	<i>Donnell</i>	<i>Exact</i>	<i>Donnell</i>	<i>Exact</i>	<i>Donnell</i>
$R_\beta/h = 100$										
$\pi/12$	14.116	14.975	11.605	11.605	10.530	10.531	10.528	10.529	10.528	10.529
$\pi/10$	14.101	14.703	11.600	11.601	10.530	10.530	10.528	10.529	10.528	10.529
$\pi/9$	14.099	14.589	11.605	11.605	10.537	10.538	10.535	10.536	10.535	10.536
$\pi/8$	14.102	14.491	11.615	11.615	10.550	10.551	10.548	10.549	10.548	10.549
$\pi/6$	14.126	14.345	11.652	11.652	10.594	10.595	10.592	10.593	10.592	10.593
$\pi/5$	14.147	14.299	11.680	11.680	10.625	10.626	10.624	10.624	10.624	10.624
$\pi/4$	14.174	14.271	11.713	11.713	10.662	10.662	10.660	10.660	10.660	10.660
$\pi/3$	14.205	14.260	11.748	11.748	10.700	10.700	10.698	10.698	10.698	10.698
$R_\beta/h = 4$										
$\pi/12$	248.90	248.98	147.36	148.48	140.81	141.88	138.72	139.72	138.66	139.67
$\pi/10$	202.31	219.47	117.94	119.20	112.76	113.98	111.15	112.31	111.12	112.28
$\pi/9$	169.54	205.42	103.16	104.52	98.689	99.995	97.307	98.558	97.290	98.540
$\pi/8$	138.38	191.98	88.387	89.844	84.631	86.031	83.483	84.832	83.473	84.821
$\pi/6$	82.756	167.51	59.240	60.925	56.882	58.489	56.209	57.776	56.206	57.773
$\pi/5$	59.380	156.84	45.292	47.090	43.548	45.261	43.105	44.785	43.105	44.784
$\pi/4$	39.898	147.53	32.400	34.272	31.142	32.929	30.903	32.664	30.902	32.663
$\pi/3$	25.447	139.82	21.741	23.510	20.779	22.486	20.690	22.379	20.690	22.379

Table 5.9. Evaluation of Donnell effect in Classical Vs Refined theories comparison on $\bar{\omega}$ of [0/90/0] cylindrical shells. $m = 1$, $n = 1$.

shell when $R_\beta/h = 100$ and a deep moderately thick shell when $R_\beta/h = 4$. In the first case the curvature parameter γ is irrelevant on the values of $\bar{\omega}$. The stiffness and the mass of the structure do not vary significantly and the frequency parameter remains almost the same. The aspect ratio a/b ranges from 0.4 to 0.01, then the shell is more like a ring. Donnell's approximation results in such case are nearly identical to the exact ones and are not influenced by the variation of γ . This is due to the radius-to-thickness parameter $R_\beta/h = 100$, and, in such case, the structure correspond to a thin shallow shell.

On the contrary, when $R_\beta/h = 4$, it can be noticed that the Donnell's approximation is meaningful respect to the curvature parameter γ . As γ increases, the error between exact solution and Donnell's one is becoming more important. To conclude, considering high-order effect in shell theories can result meaningless unless an accurate description of the curvatures term related to γ is made at the same time.

5.5.6 Natural frequencies versus wave mode number curves

The first two natural frequencies without axial stress are plotted in Figure 5.2. A symmetric [0/90/0] cross-ply laminated composite cylindrical shell is considered, with equal thickness of each lamina and $\gamma = \pi/3$. A shallow thin shell is considered, since the radius-to-thickness parameter $R_\beta/h = 100$. Only results obtained using a LD4 model are plotted, as the same trend can be found also for all higher-order theories. The dominant first two

eigenvalues that correspond to the lowest two natural frequencies are of most concern. The lower natural frequency $\bar{\omega}_1$ is a flexural mode with some shear deformations, whereas the upper frequency $\bar{\omega}_2$ is an extensional mode with thickness changes. Figures 5.3 to 5.5 show the variation of the first two natural frequencies for $m = 1 - 3$ with respect to $n = 0 - 10$. Although, in general, the natural frequencies increase as the circumferential wave number n grows, the lowest frequencies occur at specific higher modes in the case of the first natural frequencies for $m = 1, 2$, as shown in detail in Figures 5.3, 5.4. When $m = 3$ also the first natural frequency increases as n goes from 0 – 10 (see Figure 5.5).

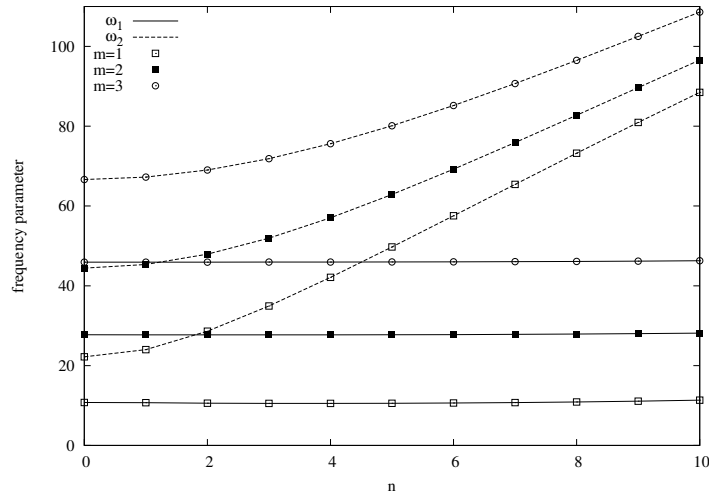


Figure 5.2. Natural frequency parameter versus circumferential mode number curves of a [0/90/0] cylindrical shell. $a/h = 10$, $\gamma = \pi/3$, $R_\beta/h = 100$.

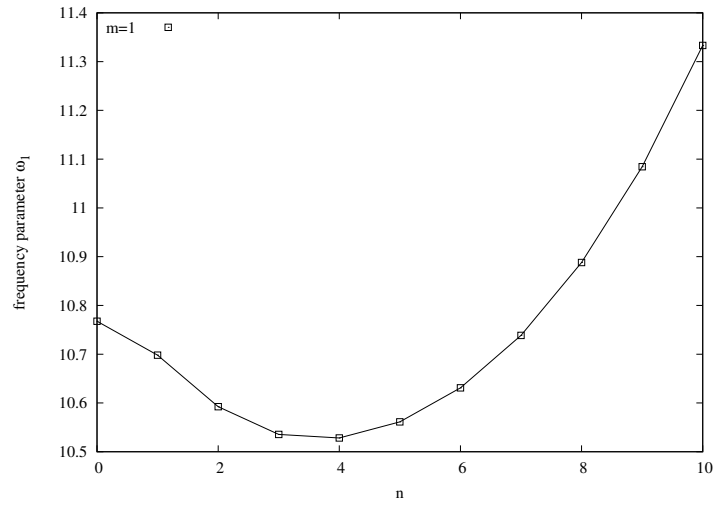


Figure 5.3. Detail for $\bar{\omega}_1$ with axial wave number $m=1$.

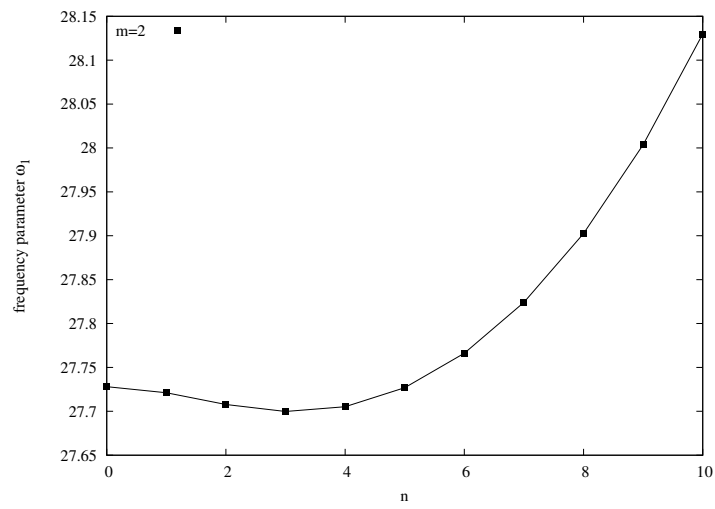


Figure 5.4. Detail for $\bar{\omega}_1$ with axial wave number $m=2$.

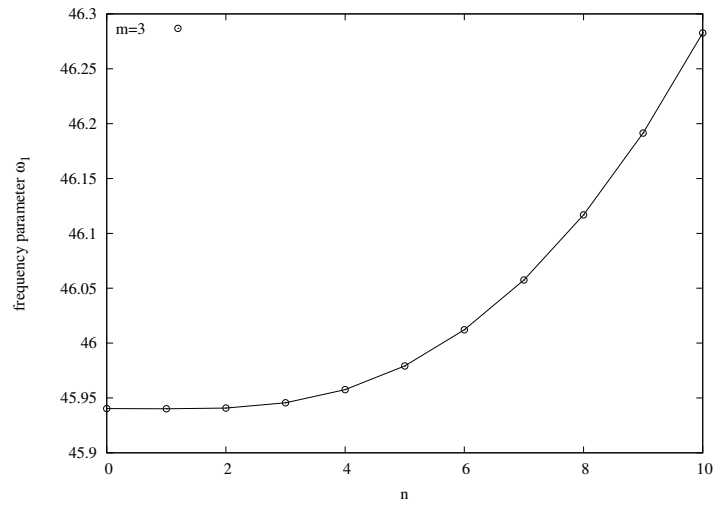


Figure 5.5. Detail for $\bar{\omega}_1$ with axial wave number $m=3$.

5.6 Conclusions

A unified approach to formulate two-dimensional shell theories has been here addressed to evaluate the free vibration response of cylindrical multi-layered shells made of composite materials. Both thin shallow shells and moderately thick deep ones are considered, as well as lower and higher vibration modes. Analyses are carried out considering the influence of the stacking sequences of laminate, the degree of orthotropy, the thickness and the curvature parameters. Higher-order theories are considered in the framework of Love- and Donnell-type approximations. Classical theories have been considered for comparison purpose. The following main remarks can be made: 1- Classical models yield good results only for thin shallow shells, 2- Zig-zag function increases the results accuracy of Equivalent Single Layer Models, 3- a very accurate description of the vibration response of highly anisotropic thick shells requires a Layer-Wise approach. Above all it must be highlighted that inclusion of shear deformation and higher-order effects could result meaningless unless curvatures terms are correctly included in a given theories.

Chapter 6

Trigonometric basis functions and Unified Formulation

6.1 Introduction

The aim of the present section is to extend the bases functions used for higher order shell theories to a trigonometric basis functions. Carrera Unified Formulation for the modelling of composite shell structures is adopted. Equivalent single layer and layer-wise shells theories based on trigonometric functions expansions are then considered to evaluate the static behavior of multilayered, orthotropic plates and shells.

Classical theories (Classical Lamination Theory, CLT) developed for thin elastic shells are based on Love-Kirchhoff's assumptions [61]. Nowadays curved shell structures made of composite laminae have gained widespread acceptance for primary structural components due to high value of strength- and stiffness-to-weight ratios. Love-Kirchhoff's kinematic assumptions applied to layered anisotropic composite shells may not yield a correct prediction of displacements and stresses fields. These materials exhibit high transverse shear deformation and discontinuous material properties in the thickness direction. These features require the development of refined theories [23, 25]. According to published research, various theories in mechanics for composite structures have been developed. They can be classified as:

- Equivalent Single Layer (ESL): the number of unknowns is independent from the number of layers, but the shear stress continuity on the interfaces of layers is often violated.
- Layer-wise approach (LW): this theory aims at overcoming the restriction of the ESL about the discontinuity of in-plane displacement on the interface layers.

A review of equivalent single layer and layer-wise laminate theories is presented by Reddy [98]. Concerning trigonometric theories for structural analysis the following literature is found. Shimpi and Ghugal [109] have used trigonometric terms in the displacements field for the analysis of two layers composite beams. An ESL model is developed by Arya et al. [6]

using a sine term to represent the non-linear displacement field across the thickness in symmetric laminated beams. An extension of [6] to composite plates is presented by Ferreira et al. [46]. A trigonometric shear deformation theory is used to model symmetric composite plates discretized by a meshless method based on global multiquadric radial basis functions. A specialized version of this theory with a layer-wise approach is proposed by the same authors in [104]. Vidal and Polit [121] designed a new three-noded beam finite element for the analysis of laminated beams, based on a sinus distribution with layer refinement. A recent work from the same authors [122] deals with the influence of the Murakami's zig-zag function in the sine model for static and vibration analysis of laminated beams. Static and free vibration analysis of laminated shells is performed by radial basis functions collocation, according to a sinusoidal shear deformation theory in Ferreira et al. [45]. It accounts for through-the-thickness deformation, by considering a sinusoidal evolution of all displacements with the thickness coordinate.

In the framework of the Unified Formulation 5.3.5, to postulate the displacements distribution, we present a new set of trigonometric functions of the shell thickness coordinate z . This approach is adopted in ESL and LW models. In the next subsections we present the unified and compact form of resulting equations.

6.2 Trigonometric Shell Theories

6.2.1 Equivalent single layer model

Considering equivalent single layer formulation, the two dimensional shells theories seen in Sec. 5.3.2 have been extended to a new trigonometric basis function defined as:

$$\{1, z, \cos(\pi z/h), \sin(\pi z/h), \cos(2\pi z/h), \sin(2\pi z/h), \cos(3\pi z/h), \dots, \cos(n\pi z/h), \sin(n\pi z/h)\} \quad (6.1)$$

The complete displacements field can be written as:

$$\begin{aligned} \mathbf{u} = & \mathbf{u}_0 + \mathbf{u}_1 z + \mathbf{u}_2 \cos\left(\pi \frac{z}{h}\right) + \mathbf{u}_3 \sin\left(\pi \frac{z}{h}\right) + \mathbf{u}_4 \cos\left(2\pi \frac{z}{h}\right) + \mathbf{u}_5 \sin\left(2\pi \frac{z}{h}\right) + \\ & + \mathbf{u}_6 \cos\left(3\pi \frac{z}{h}\right) + \dots + \mathbf{u}_N \cos\left(N\pi \frac{z}{2h}\right) + \mathbf{u}_{N+1} \sin\left(N\pi \frac{z}{2h}\right) \end{aligned} \quad (6.2)$$

where $\mathbf{u} = \{u_\alpha, u_\beta, u_z\}$. We mention this theory with the acronym 'TN', where 'T' refers to the trigonometric basis functions adopted to write the assumed displacements field. The kinematics of the proposed theory (Eq. 6.2) is useful, because if the trigonometric term (involving thickness coordinate z) is expanded in power series, the kinematics of higher order theories (which are usually obtained by power series in thickness coordinate z) are implicitly taken into account. Thus the use of trigonometric functions in the thickness coordinate (in the kinematics) also results in the reduction of the number of unknown variables as compared to other theories, as Layer-Wise (LW).

The ESL theories mentioned above have the number of unknown variables that are independent from the number of constitutive layers N_l .

6.2.2 Layer-wise approach

If detailed response of individual layers is required and if significant variations in displacements gradients between layers exist, as it is the case of local phenomena description, a layer-wise approach is necessary. That is, each layer is seen as an independent plate/shell and compatibility of displacement components with correspondence to each interface is then imposed as a constraint. Legendre Polynomials basis functions is usually adopted (Eqs. 5.10, 5.11). In the framework of trigonometric functions expansions, we present and validate a new set of thickness functions for layer-wise approach. We use functions containing sine and cosine terms instead of Legendre Polynomials. This new set of trigonometric functions meets conditions in Eq. 5.13. The thickness functions F_t and F_b are defined as previously:

$$F_t = \frac{P_0 + P_1}{2} \quad F_b = \frac{P_0 - P_1}{2} \quad (6.3)$$

whereas F_r , $r = 2, 3, \dots, N$, are redefined in the following way:

$$\begin{aligned} F_2 &= \cos\left(\frac{\pi}{2}\zeta_k\right), \quad F_3 = \sin\left(\frac{\pi}{2}\zeta_k\right) - \zeta_k, \quad F_4 = \cos(\pi\zeta_k) + 1, \quad F_5 = \sin(\pi\zeta_k) \\ F_6 &= \cos\left(\frac{3\pi}{2}\zeta_k\right), \quad F_7 = \sin\left(\frac{3\pi}{2}\zeta_k\right) + \zeta_k, \quad F_8 = \cos(2\pi\zeta_k) - 1, \quad F_9 = \sin(2\pi\zeta_k) \\ F_{10} &= \cos\left(\frac{5\pi}{2}\zeta_k\right), \quad F_{11} = \cos\left(\frac{5\pi}{2}\zeta_k\right) - \zeta_k \end{aligned} \quad (6.4)$$

The maximum expansion order introduced is $N = 11$. Besides to the sine and cosine functions, in some case we added a unit or a linear term, so as to satisfy the conditions of Eq. 5.13 seen before. The displacements expansion of Eq. 5.10 is still valid, but F_r are now defined by Eq. 6.4. We refer to this theories with the acronym 'LDTN', where 'T' stands for trigonometric thickness functions basis.

6.2.3 Carrera Unified Formulation

Carrera Unified Formulation (UF) is adopted to obtain two dimensional models for shells. In case only displacements assumption is introduced, the following expansion in the thickness coordinate z can be written:

$$\mathbf{u}^k = F_\tau(z)\mathbf{u}_\tau^k(\alpha, \beta) \quad k = 1, 2, \dots, N_l \quad (6.5)$$

where:

- $\mathbf{u} = \{u_\alpha, u_\beta, u_z\}$ are the three displacement components of the generic shell point $P(\alpha, \beta, z)$ measured in a curvilinear reference system (α, β, z) .
- $\mathbf{u}_\tau = \{u_{\tau\alpha}, u_{\tau\beta}, u_{\tau z}\}$ are the introduced displacement variables that depend only on the coordinates α and β , lying on the reference shell surface.
- F_τ are the introduced functions of the thickness coordinates z .

- N_l is the number of layers of the laminate.

Einstein convention for repeated indexes is referred to. The order of the expansion as well as the choice of the base functions used to build the thickness function F_τ is completely free. Therefore the set of trigonometric functions (Eq. 6.1) proposed in the present section can be easily introduced. The introduced assumptions for displacements 6.5 can be made at layer or at multilayer level. Layer-Wise (LW) description is obtained in the first case whereas Equivalent Single Layer (ESL) description is acquired in the latter one. If LW description is employed than \mathbf{u}_τ are layer variables. These are different in each layer. If ESL description is referred to, then \mathbf{u}_τ are shell variables. These are the same for the whole multilayer. Examples of ESL and LW assumption are given in Fig. 6.1.

The governing equations and the boundary conditions are derived via the Principle of

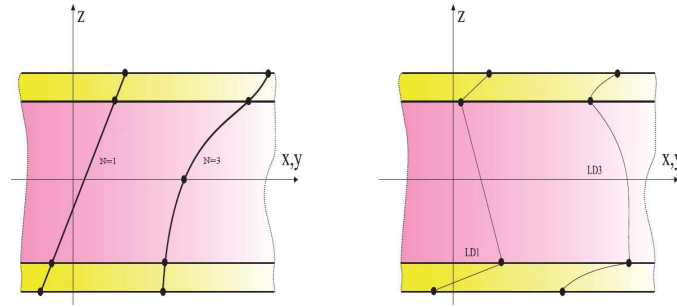


Figure 6.1. Examples of ESL (left) and LW (right) assumptions. Linear and cubic cases.

Virtual Displacements (PVD) in a general way that does not depend upon the variable description (ESL or LW) and the expansion order (Sec. 6.3). Carrera Unified Formulation (UF) is employed to derive shell equations that are solved for the case of simply supported boundary conditions and doubly curved shells with constant curvatures. Navier-type closed form solutions are obtained (Sec. 6.4). Results for multilayered cross-ply shells and plates are presented to validate the proposed theory, and further are compared with exact solutions present in literature.

6.3 Governing Equations

6.3.1 Equations for the N_l layers

The displacements approach is formulated in terms of \mathbf{u}^k by variationally imposing the equilibrium via PVD, considering also an external load p_z^k :

$$\begin{aligned} \sum_{k=1}^{N_l} \int \int_{\Omega_k h_k} (\delta \boldsymbol{\epsilon}_p^{kT} \boldsymbol{\sigma}_p^k + \delta \boldsymbol{\epsilon}_n^{kT} \boldsymbol{\sigma}_n^k) dz_k d\Omega_k &= \\ &= \sum_{k=1}^{N_l} \int_{\Sigma_k^b \cup \Sigma_k^t} \delta \mathbf{u}^{kT} \mathbf{p}^k d\Omega_k \end{aligned} \quad (6.6)$$

where

$$\boldsymbol{\epsilon}_p = \begin{Bmatrix} \epsilon_{\alpha\alpha} \\ \epsilon_{\beta\beta} \\ \epsilon_{\alpha\beta} \end{Bmatrix}, \boldsymbol{\epsilon}_n = \begin{Bmatrix} \epsilon_{\alpha z} \\ \epsilon_{\beta z} \\ \epsilon_{zz} \end{Bmatrix}, \boldsymbol{\sigma}_p = \begin{Bmatrix} \sigma_{\alpha\alpha} \\ \sigma_{\beta\beta} \\ \sigma_{\alpha\beta} \end{Bmatrix}, \boldsymbol{\sigma}_n = \begin{Bmatrix} \sigma_{\alpha z} \\ \sigma_{\beta z} \\ \sigma_{zz} \end{Bmatrix} \quad (6.7)$$

‘T’ as superscript stands for the transposition operator. δ signifies virtual variations. $\mathbf{p}^{kT} = \{p_\alpha^k, p_\beta^k, p_z^k\}$ is a generic pressure loading acting on the top (Σ_k^t) and on the bottom (Σ_k^b) of each lamina. The variation of the internal work has been split into in-plane and out-of-plane parts and involves the stresses obtained from Hooke’s law 5.23 and the strains from the geometrical relations 5.20, which replaced together with the unified displacement field of Eq. 6.5 into Eq. 6.6, gives:

$$\begin{aligned} & \sum_{k=1}^{N_l} \int_{\Omega_k} \delta \mathbf{u}_\tau^{kT} \int_{h_k} \{(-F_\tau \mathbf{D}_p^T + F_\tau \mathbf{A}_p^T)[\tilde{\mathbf{C}}_{pp}^k(F_s \mathbf{D}_p + F_s \mathbf{A}_p) + \tilde{\mathbf{C}}_{pn}^k(F_s \mathbf{D}_{n\Omega} + F_s \mathbf{A}_n + F_{s,z})] + (-F_\tau \mathbf{D}_{n\Omega}^T + \\ & + F_\tau \mathbf{A}_n^T + F_{\tau,z})[\tilde{\mathbf{C}}_{np}^k(F_s \mathbf{D}_p + F_s \mathbf{A}_p) + \tilde{\mathbf{C}}_{nn}^k(F_s \mathbf{D}_{n\Omega} + F_s \mathbf{A}_n + F_{s,z})]\} H_\alpha^k H_\beta^k dz_k \mathbf{u}_s^k d\Omega_k + \\ & + \sum_{k=1}^{N_l} \int_{\Gamma_k} \delta \mathbf{u}_\tau^{kT} \int_{h_k} \{F_\tau \mathbf{I}_p^T[\tilde{\mathbf{C}}_{pp}^k(F_s \mathbf{D}_p + F_s \mathbf{A}_p) + \tilde{\mathbf{C}}_{pn}^k(F_s \mathbf{D}_{n\Omega} + F_s \mathbf{A}_n + F_{s,z})] + F_\tau \mathbf{I}_{n\Omega}^T[\tilde{\mathbf{C}}_{np}^k(F_s \mathbf{D}_p + \\ & + F_s \mathbf{A}_p) + \tilde{\mathbf{C}}_{nn}^k(F_s \mathbf{D}_{n\Omega} + F_s \mathbf{A}_n + F_{s,z})]\} H_\alpha^k H_\beta^k dz_k \mathbf{u}_s^k d\Gamma_k = \sum_{k=1}^{N_l} \int_{\Sigma_k^b \cup \Sigma_k^t} \delta \mathbf{u}_\tau^{kT} \mathbf{p}_\tau^k d\Omega_k \end{aligned} \quad (6.8)$$

being:

$$\mathbf{I}_p = \begin{bmatrix} \frac{1}{H_\alpha^k} & 0 & 0 \\ 0 & \frac{1}{H_\beta^k} & 0 \\ \frac{1}{H_\beta^k} & \frac{1}{H_\alpha^k} & 0 \end{bmatrix} \quad \mathbf{I}_{n\Omega} = \begin{bmatrix} 0 & 0 & \frac{1}{H_\alpha^k} \\ 0 & 0 & \frac{1}{H_\beta^k} \\ 0 & 0 & 0 \end{bmatrix} \quad (6.9)$$

$\mathbf{p}_\tau^k = \{p_{\alpha\tau}^k, p_{\beta\tau}^k, p_{z\tau}^k\}$ are the variationally consistent load vectors coming from the applied loadings \mathbf{p}^k . By imposing the definition of virtual variations for the unknown displacement variables, the differential system of governing equations and related boundary conditions for the N_l k -layers in each Ω_k domain are found. The differential system of governing equations is:

$$\delta \mathbf{u}_\tau^k : \quad \mathbf{K}_d^{k\tau s} \mathbf{u}_s^k = \mathbf{p}_\tau^k \quad (6.10)$$

with boundary conditions:

$$\begin{aligned} \mathbf{u}_\tau^k &= \bar{\mathbf{u}}_\tau^k && \text{geometrical on } \Gamma_k^g \\ \mathbf{\Pi}_d^{k\tau s} \mathbf{u}_s^k &= \mathbf{\Pi}_d^{k\tau s} \bar{\mathbf{u}}_s^k && \text{mechanical on } \Gamma_k^m \end{aligned} \quad (6.11)$$

The further subscript d signifies values employed in the displacements formulation. Differential stiffness and mechanical boundary conditions matrices are:

$$\begin{aligned}
 \mathbf{K}_d^{k\tau s} &= \int_{h_k} \{(-F_\tau \mathbf{D}_p^T + F_\tau \mathbf{A}_p^T)[\tilde{\mathbf{C}}_{pp}^k(F_s \mathbf{D}_p + F_s \mathbf{A}_p) + \tilde{\mathbf{C}}_{pn}^k(F_s \mathbf{D}_{n\Omega} + F_s \mathbf{A}_n + F_{s,z})] + \\
 &+ (-F_\tau \mathbf{D}_{n\Omega}^T + F_\tau \mathbf{A}_n^T + F_{\tau,z})[\tilde{\mathbf{C}}_{np}^k(F_s \mathbf{D}_p + F_s \mathbf{A}_p) + \tilde{\mathbf{C}}_{nn}^k(F_s \mathbf{D}_{n\Omega} + F_s \mathbf{A}_n + F_{s,z})]\} H_\alpha^k H_\beta^k dz_k \\
 \mathbf{\Pi}_d^{k\tau s} &= \int_{h_k} \{F_\tau \mathbf{I}_p^T[\tilde{\mathbf{C}}_{pp}^k(F_s \mathbf{D}_p + F_s \mathbf{A}_p) + \tilde{\mathbf{C}}_{pn}^k(F_s \mathbf{D}_{n\Omega} + F_s \mathbf{A}_n + F_{s,z})] + \\
 &+ F_\tau \mathbf{I}_{n\Omega}^T[\tilde{\mathbf{C}}_{np}^k(F_s \mathbf{D}_p + F_s \mathbf{A}_p) + \tilde{\mathbf{C}}_{nn}^k(F_s \mathbf{D}_{n\Omega} + F_s \mathbf{A}_n + F_{s,z})]\} H_\alpha^k H_\beta^k dz_k
 \end{aligned} \tag{6.12}$$

Previous equations consist of 3×3 fundamental nuclei. The following sub/super-scripts are applied: τ , s and k . Explicit forms of the governing equations for each layer can be written by expanding the introduced subscripts and superscripts in the previous arrays as follows:

$$k = 1, 2, \dots, N_l; \quad \tau = 0, 1, \dots, N \quad s = 0, 1, \dots, N \tag{6.13}$$

6.3.2 Assemblage and Multilayer equations

PVD has been written for the N_l independent layers. C_z^0 requirements must be imposed to drive equations from layer to multilayer level. Multilayered equations can be written according to the usual variational statements: stiffness related to the same variables is accumulated in this process. Interlaminar continuity conditions are imposed at this stage. An example is shown in Figs. 6.2 and 6.3. Details on this procedure can be found in Carrera's papers [26]. Multilayered arrays are obtained at the very end of the assemblage. The equilibrium and boundary conditions for the displacements formulation take on the following form:

$$\begin{aligned}
 \mathbf{K}_d \mathbf{u} &= \mathbf{p} \\
 \mathbf{u} &= \bar{\mathbf{u}} \quad \text{or} \quad \mathbf{\Pi}_d \mathbf{u} = \mathbf{\Pi}_d \bar{\mathbf{u}}
 \end{aligned} \tag{6.14}$$

6.4 Closed form solution

In order to assess the proposed models, equations 6.10 are herein solved for a special case in which closed form solutions are given. The particular case in which the material has the following properties (as it is the case of cross-ply shells) $\tilde{\mathbf{C}}_{16} = \tilde{\mathbf{C}}_{26} = \tilde{\mathbf{C}}_{36} = \tilde{\mathbf{C}}_{45}$ has been considered, for which Navier-type closed form solutions can be found by assuming the following harmonic forms for the applied loadings $\mathbf{p}_k = \{p_{\alpha\tau}^k, p_{\beta\tau}^k, p_{z\tau}^k\}$ and unknown

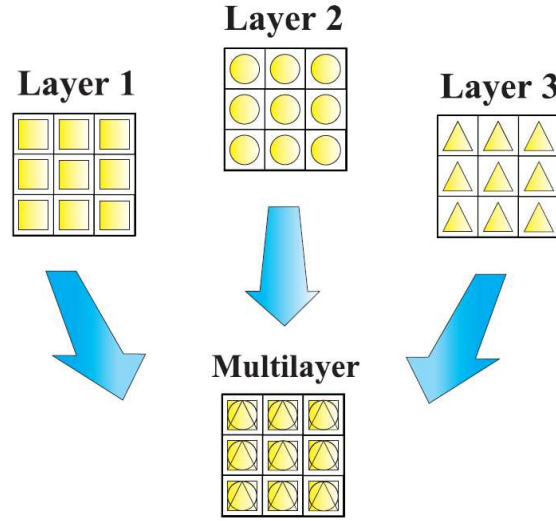


Figure 6.2. Assemblage from layer to multilayered level in ESLM description for a three layered plate.

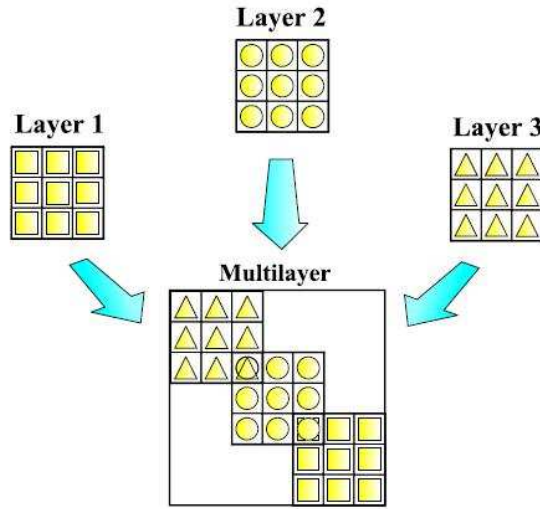


Figure 6.3. Assemblage from layer to multilayered level in LW description for a three layered plate.

displacement $\mathbf{u}_k = \{u_{\alpha\tau}^k, u_{\beta\tau}^k, u_{z\tau}^k\}$ variables in each k -layer:

$$\begin{aligned}
 (u_{\alpha\tau}^k, p_{\alpha\tau}^k) &= \sum_{m=1}^{\bar{m}} \sum_{n=1}^{\bar{n}} (U_{\alpha\tau}^k(z), P_{\alpha\tau}^k(z)) \cos\left(\frac{m\pi}{a_k}\alpha_k\right) \sin\left(\frac{n\pi}{b_k}\beta_k\right) \\
 (u_{\beta\tau}^k, p_{\beta\tau}^k) &= \sum_{m=1}^{\bar{m}} \sum_{n=1}^{\bar{n}} (U_{\beta\tau}^k(z), P_{\beta\tau}^k(z)) \sin\left(\frac{m\pi}{a_k}\alpha_k\right) \cos\left(\frac{n\pi}{b_k}\beta_k\right) \\
 (u_{z\tau}^k, p_{z\tau}^k) &= \sum_{m=1}^{\bar{m}} \sum_{n=1}^{\bar{n}} (U_{z\tau}^k(z), P_{z\tau}^k(z)) \sin\left(\frac{m\pi}{a_k}\alpha_k\right) \sin\left(\frac{n\pi}{b_k}\beta_k\right)
 \end{aligned} \tag{6.15}$$

$k = 1, \dots, N_l; \quad \tau = 0, \dots, N$

which correspond to simply-supported boundary conditions. a_k and b_k are the lengths of the shell along the two coordinates α_k and β_k . m and n represent the number of half-waves in α_k and β_k direction, respectively. Capital letters indicate amplitudes. Upon substitution of Eq. 6.15, the governing equations assume the form of a linear system of ordinary differential equations.

6.5 Numerical Results and Discussion

The higher-order trigonometric theories described above have been applied to the static analysis of multilayered composite plates and shells. The mechanical material properties of the lamina are: $E_L = 25E_T$, $G_{LT} = 0.5E_T$, $G_{TT} = 0.2E_T$, $\nu_{LT} = \nu_{TT} = 0.25$. Subscript 'L' stands for direction parallel to the fibres, 'T' identifies the transverse direction, ν_{LT} is the major Poisson's ratio. Thin and moderately thick plates and shells are considered. The total thickness of the laminate is h . We present results for 'classical' and trigonometric ESL and LW theories. A comparison with available exact solutions is given in the following paragraphs.

6.5.1 Assessment

Tables 6.1 and 6.2 show a comparison between the ESL models.

<i>layers</i>	$\bar{u}_z(a/2, a/2, 0)$		$\bar{\sigma}_{\alpha\alpha}(a/2, a/2, 1/2)$		$\bar{\sigma}_{\alpha z}(0, a/2, 0)$	
	3	9	3	9	3	9
<i>3D</i> [85]	1.709	1.512	0.559	0.551	0.301	0.247
<i>N</i> = 4	1.665	1.413	0.559	0.546	0.284	0.384
<i>N</i> = 3	1.665	1.413	0.560	0.547	0.284	0.384
<i>N</i> = 2	1.448	1.342	0.504	0.517	0.141	0.262
<i>N</i> = 1	1.436	1.333	0.501	0.515	0.140	0.260
<i>T4</i>	1.672	1.412	0.560	0.546	0.295	0.389
<i>T3</i>	1.672	1.412	0.561	0.547	0.295	0.389
<i>T2</i>	1.448	1.342	0.504	0.517	0.141	0.262
<i>CLT</i>	1	1	0.539	0.539	0.339	0.259

Table 6.1. Comparison between ESL with Lagrange polynomial basis functions and ESL with trigonometric basis functions results. Maximum transverse deflection \bar{u}_z and maximum stresses $\bar{\sigma}_{\alpha\alpha}$ and $\bar{\sigma}_{\alpha z}$ for 3-ply and 9-ply square plate, $a/h=10$ [85].

Results for the Lagrange polynomial basis functions and for the trigonometric basis functions are reported for a multilayered square plate and a circular cylindrical shell (see [85] and [119]). In table 6.1 we consider 3 and 9 layers cross-ply plates, with fixed side to thickness ratio $a/h = 10$. An expansion order up to four is taken into account. Considering the same stratification, with the trigonometric models we obtain almost the same results as that of the 'classical' ESL models or at least some improvements of about

R_β/h	$\bar{u}_z(z=0)$			$\bar{\sigma}_{zz}(z=0)$			$\bar{\sigma}_{\beta z}(z=0)$		
	100	10	4	100	10	4	100	10	4
3D [119]	0.4715	1.223	4.009	-8.30	-1.27	-0.62	-3.127	-3.264	-2.349
$N = 4$	0.4708	1.141	3.720	-6.28	-1.29	-0.59	-1.730	-2.292	-1.761
$N = 3$	0.4708	1.141	3.718	-6.28	-1.29	-0.59	-1.730	-2.292	-1.760
$N = 2$	0.4692	0.952	2.921	-2.52	-1.03	-0.56	-0.631	-1.158	-1.002
$N = 1$	0.4674	0.951	2.953	-2.63	-1.02	-0.54	-0.630	-1.157	-1.013
$T4$	0.4732	1.212	4.323	-6.55	-1.37	-0.67	-1.845	-2.535	-2.099
$T3$	0.4732	1.212	4.312	-6.54	-1.37	-0.68	-1.845	-2.525	-2.095
$T2$	0.4716	1.003	3.367	-2.53	-1.08	-0.66	-0.635	-1.221	-1.154
CLT	0.4656	0.5205	0.4796						

Table 6.2. Comparison between ESL with Lagrange polynomial basis functions and ESL with trigonometric basis functions results. Maximum transverse deflection \bar{u}_z and maximum stresses $\bar{\sigma}_{zz}$ and $\bar{\sigma}_{\beta z}$ for $[90^\circ/0^\circ/90^\circ]$ circular cylindrical shell [119].

4%, on equal expansion order.

Table 6.2 is referred to a 3-layers $[90^\circ/0^\circ/90^\circ]$ circular cylindrical shell subjected to transverse sinusoidal loadings at the inner layer. Thick and thin shells are considered. The TN solution is better or worse than the N solution depending on the case, but there is not a regular trend. For a given expansion order, ie. $N = 4$, the solution is worse for u_z , when $R_\beta/h = 100$ and 4, and for σ_{zz} when $R_\beta/h = 10$ and 4, whereas in other cases we obtain better results. However the maximum improvement that is achieved is at most 15%, compared to the N solution.

6.5.2 Bending of Plates

Pagano’s square laminates

In this section, we investigate the bending of square bidirectional plates consisting of 3, 5, 7 and 9 layers, loaded via a bisinusoidal loading p_{zz} . The elastic solution for this problem was given by Pagano and Hatfield in [85]. Symmetric laminations with respect to the central plane are considered, with fiber oriented alternating between 0° and 90° , with respect to the α -axis. The outer layers are 0° oriented and the total thickness of the 0° and 90° layers is the same. Moreover each layer with same orientation have same thickness. Results present the following dimensionless quantities:

$$\begin{aligned}
 \bar{u}_z &= \frac{\pi^4 Q}{12 p_0 h (a/h)^4} u_z \\
 \bar{\sigma}_{\alpha\alpha} &= \frac{1}{p_0 (a/h)^2} \sigma_{\alpha\alpha} \\
 \bar{\sigma}_{\alpha z} &= \frac{1}{p_0 (a/h)} \sigma_{\alpha z}
 \end{aligned} \tag{6.16}$$

where $Q = 4G_{LT} + (E_L + E_T(1 + 2\nu_{TT}))/ (1 - \nu_{LT}\nu_{TL})$ and p_0 is a constant representing the load’s amplitude. a is the edge length. In terms of normalized functions (6.16), the

CLT solution is independent of the ratio a/h .

a/h	$\bar{u}_z(a/2, a/2, 0)$			$\bar{\sigma}_{\alpha\alpha}(a/2, a/2, 1/2)$			$\bar{\sigma}_{\alpha z}(0, a/2, 0)$		
	100	10	4	100	10	4	100	10	4
3D [85]	1.008	1.709	4.491	0.539	0.559	0.720	0.339	0.301	0.219
T11	1.008	1.697	4.446	0.539	0.558	0.717	0.317	0.283	0.207
T10	1.008	1.694	4.433	0.539	0.558	0.717	0.338	0.302	0.158
T9	1.008	1.694	4.433	0.539	0.558	0.717	0.338	0.302	0.222
T8	1.007	1.687	4.410	0.539	0.558	0.715	0.371	0.332	0.244
T7	1.007	1.687	4.411	0.539	0.558	0.715	0.371	0.332	0.244
T6	1.007	1.686	4.401	0.539	0.558	0.714	0.377	0.335	0.240
T5	1.007	1.686	4.400	0.539	0.558	0.714	0.377	0.335	0.240
T4	1.007	1.672	4.360	0.539	0.560	0.723	0.329	0.295	0.219
T3	1.007	1.672	4.363	0.540	0.561	0.724	0.329	0.295	0.219
T2	1.005	1.448	3.454	0.539	0.504	0.432	0.149	0.141	0.118
CLT	1	1	1	0.539	0.539	0.539	0.339	0.339	0.339

Table 6.3. Maximum transverse deflection \bar{u}_z and maximum stresses $\bar{\sigma}_{\alpha\alpha}$ and $\bar{\sigma}_{\alpha z}$ for 3-ply square plate [85].

Table 6.3 reports the displacement \bar{u}_z and the stresses $\bar{\sigma}_{\alpha\alpha}$ and $\bar{\sigma}_{\alpha z}$ for a 3-ply laminate. When the plate is thin ($a/h = 100$) CLT results agree with the exact solution. It is almost unnecessary the use of higher-order theories. We have even worst results, for instance when we consider $\bar{\sigma}_{\alpha z}$. We can conclude that TN theories do not give improvement in the solution when $a/h = 100$. On the contrary considering a thick plate the proposed TN model gives better results compared with CLT ones. For the displacement \bar{u}_z we observe a smooth progression, when we increase the expansion order of the model we obtain better results. When $a/h = 4$, CLT leads to 77% error with respect to the reference solution. This error reduces to 23% using a T2 theory and it drops to less than 3% when a T3 is considered. Simply adding a sinus term it leads to a marked improvement of the solution. Finer solutions are obtained when we increase the expansion order, till an error of 1% when we take into account for a T11 theory.

In general considering all the quantities reported in the table it is important to notice the significant improvement in the results passing from T2 to T3 theory. Between these two theories an error up to 50% is seen. It is worth noting that, in some cases, when a cosine term is added in the adopted displacements field the solution doesn't change. This behavior is evident when we consider \bar{u}_z or $\bar{\sigma}_{\alpha z}$ at $a/h = 10$. Therefore it appears that in these cases there is no influence of the cosine term in the solution. We can note also an irregular trend for stresses. For $a/h = 4$ the in-plane stress $\bar{\sigma}_{\alpha\alpha}$ agrees with the exact solution when a T4 theory is considered, but adding other terms gives worse results. To have the same error of theory T4 it is necessary to go up to a T9. The same happens for the transverse stress $\bar{\sigma}_{\alpha z}$. When $a/h = 100$ or 10 a T11 gives a worse result than a T3 theory. For $a/h = 4$ an expansion order of 10 leads to an error of almost 30%, whereas already with a T3 we obtain the same value of the 3D solution. What should be noted

is that not always a higher order of expansion is associated with a solution more accurate. This means that some terms that are added to the displacements field, instead of improving the solution even lead to a worsening. We can conclude saying that increasing the expansion order can result meaningless. But when we consider the theories T2 and T3 instead, a great change in the results is seen. The sinus term added in T3 theory leads to a great improvement of the solutions. Tables 6.4, 6.5 and 6.6 refer to square bidirectional laminates consisting of 5, 7 and 9 layers respectively.

As we increase the number of layers and considering higher thickness, there is a more

a/h	$\bar{u}_z(a/2, a/2, 0)$			$\bar{\sigma}_{\alpha\alpha}(a/2, a/2, 1/2)$			$\bar{\sigma}_{\alpha z}(0, a/2, 0)$		
	100	10	4	100	10	4	100	10	4
3D [85]	1.006	1.570	4.291	0.539	0.545	0.685	0.272	0.258	0.238
T11	1.006	1.548	4.163	0.539	0.544	0.675	0.242	0.229	0.209
T10	1.006	1.544	4.140	0.539	0.543	0.671	0.240	0.226	0.205
T9	1.006	1.544	4.140	0.539	0.543	0.671	0.240	0.226	0.205
T8	1.006	1.536	4.094	0.539	0.542	0.670	0.280	0.264	0.239
T7	1.006	1.536	4.094	0.539	0.542	0.670	0.280	0.264	0.239
T6	1.005	1.496	3.912	0.539	0.544	0.671	0.384	0.364	0.324
T5	1.005	1.496	3.912	0.539	0.545	0.672	0.384	0.364	0.324
T4	1.005	1.455	3.692	0.539	0.536	0.623	0.477	0.453	0.403
T3	1.004	1.455	3.695	0.539	0.537	0.622	0.478	0.453	0.403
T2	1.004	1.365	3.143	0.539	0.506	0.456	0.309	0.292	0.255
CLT	1	1	1	0.539	0.539	0.539	0.272	0.272	0.272

Table 6.4. Maximum transverse deflection \bar{u}_z and maximum stresses $\bar{\sigma}_{\alpha\alpha}$ and $\bar{\sigma}_{\alpha z}$ for 5-ply square plate [85].

slowly convergence of the solution, both for displacement \bar{u}_z and for the in-plane stress $\bar{\sigma}_{\alpha\alpha}$. Transverse stress $\bar{\sigma}_{\alpha z}$ instead presents a different trend. As the number of layers increases, even if we consider the thin case, the solution obtained with higher order theories is worse than the results of CLT. The value that we consider in the point $(0, a/2, 0)$ has a swinging trend. We get to overcome a 50% error with for example a T10 theory. This behaviour can be explained by looking at figures 6.4 and 6.5.

A cross-ply 9 layers plate is considered. The reference solution is given by a fourth-order Layer-wise approach (LD4) [26]. Layered structures are characterized by non-continuous thermo-mechanical material property distribution in the thickness direction. We evaluate the transverse stress $\bar{\sigma}_{\alpha z}$ *a posteriori* from Hooke's law and by integration of the 3D indefinite equilibrium equations, respectively. The difference among this two ways of evaluating transverse shear stresses was investigated by Carrera in [22]. Superscript H denotes stresses evaluated with classical form of Hooke's law, while I denote stresses obtained by integration of the 3D-indefinite equilibrium equations. H type analyses lead to the poorest accuracy: interlaminar equilibria is violated in all the investigated cases. Transverse stresses evaluated by integration of the 3D indefinite equilibrium equations led to the best description in all the considered models. Considering figure 6.4 we can observe

a/h	$\bar{u}_z(a/2, a/2, 0)$			$\bar{\sigma}_{\alpha\alpha}(a/2, a/2, 1/2)$			$\bar{\sigma}_{\alpha z}(0, a/2, 0)$		
	100	10	4	100	10	4	100	10	4
3D [85]	1.005	1.529	4.153	0.539	0.548	0.678	0.272	0.255	0.219
T11	1.005	1.504	4.002	0.539	0.545	0.666	0.286	0.268	0.230
T10	1.005	1.482	3.878	0.539	0.544	0.663	0.238	0.223	0.192
T9	1.005	1.482	3.878	0.539	0.545	0.663	0.238	0.223	0.192
T8	1.004	1.482	3.654	0.539	0.544	0.653	0.170	0.223	0.140
T7	1.004	1.440	3.654	0.539	0.545	0.653	0.170	0.161	0.140
T6	1.004	1.431	3.594	0.539	0.541	0.638	0.147	0.140	0.125
T5	1.004	1.431	3.593	0.539	0.541	0.638	0.147	0.140	0.125
T4	1.004	1.424	3.540	0.539	0.542	0.632	0.171	0.163	0.147
T3	1.004	1.424	3.543	0.539	0.542	0.631	0.171	0.163	0.147
T2	1.003	1.348	3.091	0.539	0.513	0.477	0.114	0.109	0.098
CLT	1	1	1	0.539	0.539	0.539	0.272	0.272	0.272

Table 6.5. Maximum transverse deflection \bar{u}_z and maximum stresses $\bar{\sigma}_{\alpha\alpha}$ and $\bar{\sigma}_{\alpha z}$ for 7-ply square plate [85].

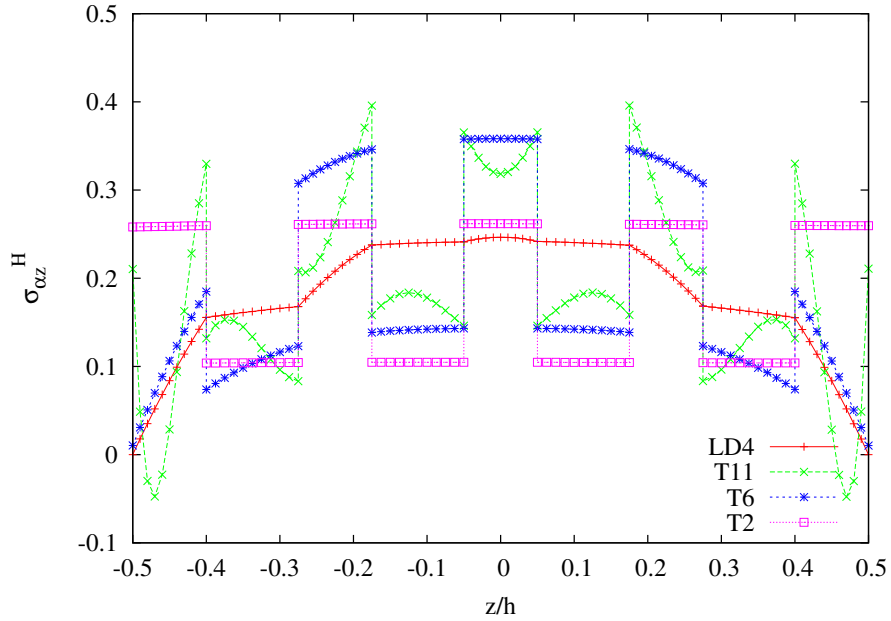


Figure 6.4. Distribution of stress $\bar{\sigma}_{\alpha z}$ for 9-ply laminate, Hooke's law case, $a/h = 10$.

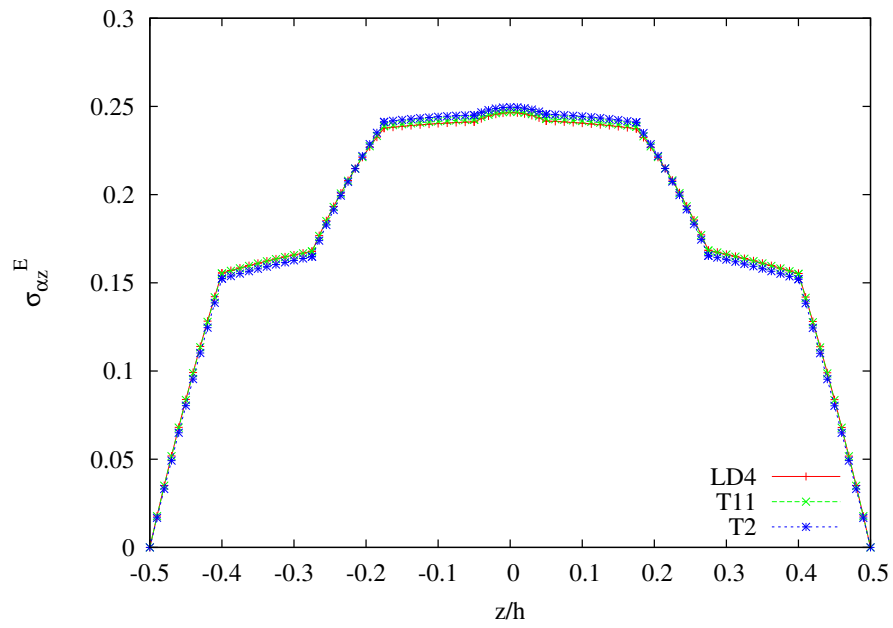


Figure 6.5. Distribution of stress $\bar{\sigma}_{\alpha z}$ for 9-ply laminate, Equilibrium equations case, $a/h = 10$.

a/h	$\bar{u}_z(a/2, a/2, 0)$			$\bar{\sigma}_{\alpha\alpha}(a/2, a/2, 1/2)$			$\bar{\sigma}_{\alpha z}(0, a/2, 0)$		
	100	10	4	100	10	4	100	10	4
<i>3D</i> [85]	1.005	1.512	4.079	0.539	0.551	0.684	0.259	0.247	0.223
<i>T11</i>	1.005	1.448	3.705	0.539	0.548	0.664	0.333	0.318	0.288
<i>T10</i>	1.004	1.420	3.544	0.539	0.546	0.649	0.406	0.390	0.355
<i>T9</i>	1.004	1.420	3.544	0.539	0.546	0.650	0.406	0.390	0.355
<i>T8</i>	1.004	1.419	3.537	0.539	0.546	0.651	0.404	0.387	0.347
<i>T7</i>	1.004	1.419	3.537	0.539	0.546	0.651	0.404	0.387	0.347
<i>T6</i>	1.004	1.415	3.507	0.539	0.545	0.647	0.376	0.358	0.317
<i>T5</i>	1.004	1.414	3.505	0.539	0.545	0.648	0.376	0.358	0.317
<i>T4</i>	1.004	1.412	3.479	0.539	0.546	0.646	0.405	0.389	0.353
<i>T3</i>	1.004	1.412	3.482	0.539	0.547	0.645	0.405	0.389	0.353
<i>T2</i>	1.003	1.342	3.072	0.539	0.517	0.491	0.272	0.262	0.240
<i>CLT</i>	1	1	1	0.539	0.539	0.539	0.259	0.259	0.259

Table 6.6. Maximum transverse deflection \bar{u}_z and maximum stresses $\bar{\sigma}_{\alpha\alpha}$ and $\bar{\sigma}_{\alpha z}$ for 9-ply square plate [85].

that the value of $\bar{\sigma}_{\alpha z}$ in the central point ($z=0$) is close to that of the reference solution when a T2 theory is adopted. To increase the expansion order leads to worse results. But if we consider the trend along the whole thickness of the plate, then we see that higher order theories, such as T6, give overall reduced errors. If we consider the I case instead we obtain the same solution for all the considered expansion orders and this results match the reference solution.

Table 6.7 reports the displacement u_z for a 9-ply laminate. When the plate is thin ($a/h = 100$) we have agreement with the reference solution for all the considered theories and expansion orders. Instead, when a/h decreases we notice the difference between ESL and LW theories. In the case $a/h = 10$ we have an error of 7% and it reaches 15% for $a/h = 4$. For this case, the trigonometric theories do not give improvements respect to the classic ones. This behavior is highlighted in Figure 6.6, which represents the displacement u_z in function of the plate's thickness. The most thick plate case has been considered ($a/h = 4$). The ED4 and EDT4 curves are overlapped as well as those related to LD4 and LDT4. Figures 6.7, 6.8 and 6.9 show the distributions of displacement u_z and stresses and for a 3-ply laminate, in the $a/h = 10$ case. Results for classical and trigonometric theories are comparable.

	<i>EDN</i>	<i>EDTN</i>	<i>LDN</i>	<i>LDTN</i>
<i>a/h</i> = 100				
Ref. [13]		1.005		
<i>N</i> = 4	1.004	1.004	1.005	1.005
<i>N</i> = 3	1.004	1.004	1.005	1.005
<i>N</i> = 2	1.003	1.003	1.005	1.005
<i>a/h</i> = 10				
Ref. [13]		1.512		
<i>N</i> = 4	1.413	1.412	1.512	1.512
<i>N</i> = 3	1.413	1.412	1.512	1.512
<i>N</i> = 2	1.342	1.342	1.512	1.512
<i>a/h</i> = 4				
Ref. [13]		4.079		
<i>N</i> = 4	3.488	3.479	4.079	4.079
<i>N</i> = 3	3.493	3.482	4.079	4.078
<i>N</i> = 2	3.074	3.072	4.078	4.078
<i>CLT</i>		1		

Table 6.7. Maximum transverse deflection \bar{u}_z evaluated in $z = 0$ for 9-ply square plate, Ref. [85].

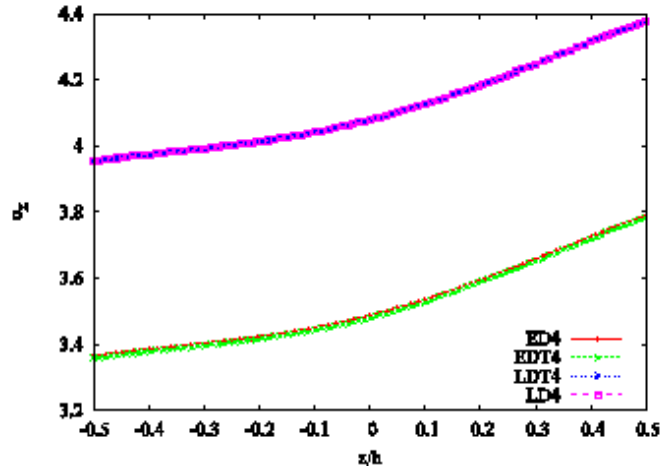


Figure 6.6. Distribution of displacement \bar{u}_z for 9-ply laminate, $a/h = 4$, expansion order $N = 4$. Results for classical and trigonometric ESL and LW models.

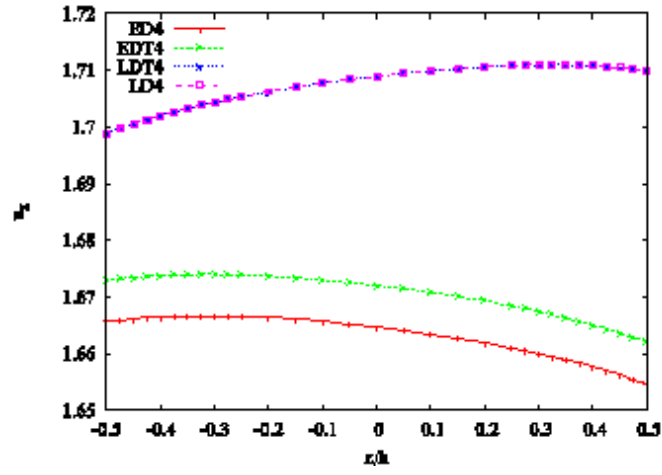


Figure 6.7. Distribution of displacement \bar{u}_z for 3-ply laminate, $a/h = 10$

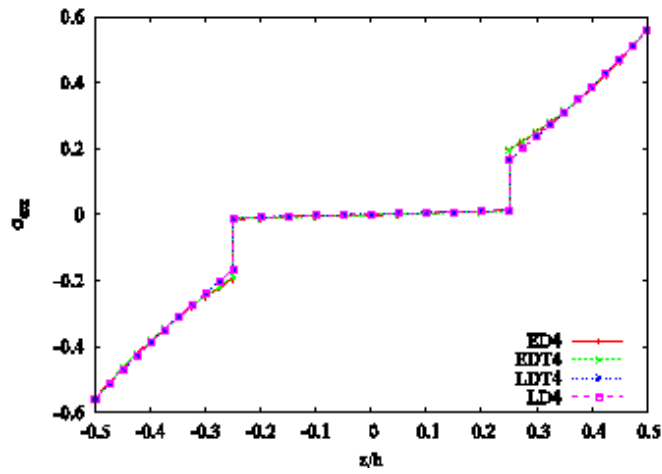
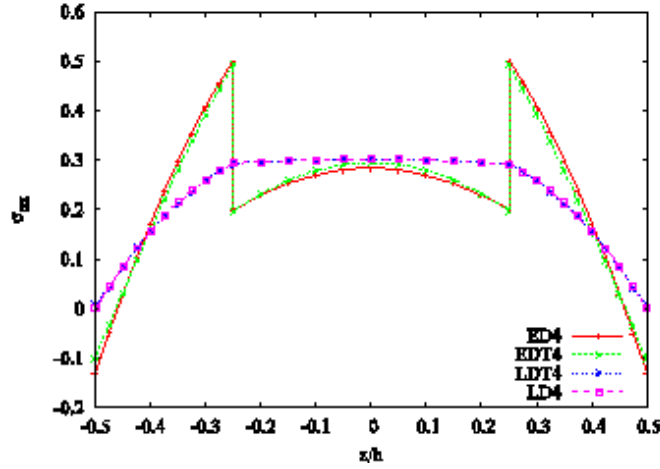


Figure 6.8. Distribution of stress $\bar{\sigma}_{\alpha\alpha}$ for 3-ply laminate, $a/h = 10$

Figure 6.9. Distribution of stress $\bar{\sigma}_{\alpha z}$ for 3-ply laminate, $a/h = 10$

6.5.3 Bending of Shells

Ren's Cylindrical Panels

Results presented in Table 6.8 refer to a $[90^\circ/0^\circ/90^\circ]$ cylindrical shell with layers of equal thickness, loaded via a bisinusoidal loading p_{zz} applied at the top (external) layer. Exact solutions were considered by Ren [103] for cross-ply cylindrical panels in cylindrical bending. The geometrical data (see fig. 6.10) are: number of half-waves in β_k direction $n = 1$ and $R_\beta/b = \pi/3$. Layers are numbered, starting from the shell bottom–internal surface.

The fibre L -orientation coincided with the α_k -layers direction. Transverse displacement, in-plane and transverse shear stresses values are normalized by:

$$\begin{aligned}\bar{u}_z &= \frac{10 E_T}{p_0 h (R_\beta/h)^4} u_z \\ \bar{\sigma}_{\beta\beta} &= \frac{1}{p_0 (R_\beta/h)^2} \sigma_{\beta\beta} \\ \bar{\sigma}_{\beta z} &= \frac{1}{p_0 (R_\beta/h)} \sigma_{\beta z}\end{aligned}\tag{6.17}$$

We consider the trigonometric set of thickness functions described in Sec. 6.2.1 to carry out the analyses. Some considerations about table 6.8 are made hereinafter.

We present results also for the classical ESL and LW models in order to provide a comparison with the new trigonometric basis functions. Concerning the displacement, \bar{u}_z trigonometric LW theories provide results in agreement with the reference solution for an expansion order as low as 3 and for both thin and thick shells. Therefore higher expansion orders are not necessary for this case. Instead, if we consider the TN models we note that for the displacement \bar{u}_z there is a regular trend. Adding terms in the expansion

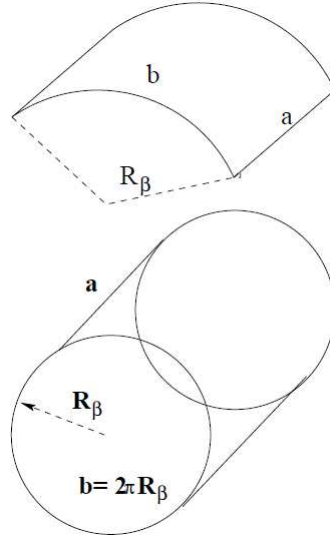


Figure 6.10. Geometrical notations used for the investigated cylindrical panels and cylindrical shells.

improves the result, especially considering thick shells ($R_\beta/h = 4$), but at least we get to an error of 11%. When the shell is thin ($R_\beta/h = 100$) higher-order theories do not give improvement in the solution, respect the CLT results. In fact the difference between CLT and LDT11 solutions is about 1%. Considering stress $\bar{\sigma}_{\beta\beta}$, with trigonometric ESL models, we notice that in some cases adding a term in the expansion leads to major errors. The thick shell case ($R_\beta/h = 4$) presents an irregular trend. For example the solution that we obtain with an expansion order of 10 is worse than that relative to $N = 3$. Therefore it becomes interesting to study the contribution of each term in the expansion. LDTN results convergence to the reference solution already for $N = 4$ and thus we do not need to add other terms to increase the accuracy of the solution. The transverse shear component $\bar{\sigma}_{\beta z}$ presents an unexpected behaviour. The solutions that we obtain with the trigonometric ESL models are better than the LW ones, when we consider high expansion orders. In fact, the LW solutions do not change from $N = 3$ onwards, but the error remains high especially in the case of thin plate where it reaches 30%. The EDTN models instead have a regular trend and as we add terms to the expansion we obtain more accurate solutions.

Varadan and Bhaskar's Cylindrical Shells

Varadan and Bhaskar [119] considered exact solutions for cross-ply laminated, cylindrical shells, subjected to transverse pressure p_{zz} at the bottom (internal) surface. The geometrical data (see fig. 6.10) are: $a/R_\beta = 4$, $m = 1$, $n = 8$. The three layers $[90^\circ/0^\circ/90^\circ]$

R_β/h	$\bar{u}_z(z=0)$			$\bar{\sigma}_{\beta\beta}(z=h/2)$			$\bar{\sigma}_{\beta z}(z=0)$		
	100	10	4	100	10	4	100	10	4
3D [103]	0.0787	0.144	0.457	0.781	0.897	1.367	0.523	0.525	0.476
LDT4 – 11	0.0786	0.144	0.458	0.779	0.897	1.367	0.367	0.497	0.442
LDT3	0.0786	0.144	0.458	0.779	0.896	1.363	0.367	0.497	0.442
LDT2	0.0786	0.144	0.454	0.779	0.895	1.344	0.366	0.496	0.438
LD4	0.0786	0.144	0.458	0.779	0.897	1.367	0.367	0.497	0.442
LD3	0.0786	0.144	0.458	0.779	0.897	1.367	0.367	0.497	0.442
LD2	0.0786	0.144	0.454	0.779	0.896	1.347	0.366	0.496	0.437
LD1	0.0785	0.141	0.441	0.779	0.866	1.213	0.366	0.498	0.446
T11	0.0782	0.135	0.404	0.775	0.831	0.910	0.416	0.524	0.436
T10	0.0782	0.135	0.403	0.775	0.830	0.895	0.430	0.537	0.454
T9	0.0782	0.135	0.396	0.774	0.846	1.140	0.430	0.537	0.451
T8	0.0782	0.135	0.395	0.775	0.845	1.136	0.408	0.515	0.426
T7	0.0782	0.135	0.397	0.775	0.849	1.187	0.408	0.515	0.427
T6	0.0781	0.133	0.388	0.775	0.845	1.180	0.337	0.446	0.365
T5	0.0781	0.133	0.387	0.775	0.846	1.169	0.337	0.446	0.365
T4	0.0781	0.131	0.380	0.775	0.842	1.179	0.233	0.356	0.317
T3	0.0781	0.131	0.380	0.776	0.844	1.196	0.233	0.355	0.317
T2	0.0779	0.113	0.292	0.774	0.739	0.710	0.033	0.166	0.164
CLT	0.0776	0.078	0.078	0.776	0.759	0.732			

Table 6.8. Maximum transverse deflection \bar{u}_z and maximum stresses $\bar{\sigma}_{\beta\beta}$ and $\bar{\sigma}_{\beta z}$ for $[90^\circ/0^\circ/90^\circ]$ cylindrical shell [103].

lamination schemes have been considered. Results are quoted in Table 6.9:

$$\begin{aligned}
 \bar{u}_z &= \frac{10 E_L}{p_0 h (R_\beta/h)^4} u_z \\
 \bar{\sigma}_{zz} &= \frac{1}{p_0} \sigma_{zz} \\
 \bar{\sigma}_{\beta z} &= \frac{10}{p_0 (R_\beta/h)} \sigma_{\beta z}
 \end{aligned} \tag{6.18}$$

The conclusions and comments reached for the cylindrical panels (Sec. 6.5.3) can be extended to cylindrical shells. For the transverse displacement \bar{u}_z a T2 ($R_\beta/h = 100$) or at least a T3 ($R_\beta/h = 10, 4$) theory is enough to match the reference solution. Actually by adding more terms the solution gets worse. We note the same behaviour considering stresses. For $\bar{\sigma}_{\beta z}$ at $R_\beta/h = 10$ the error respect the reference solution goes from 5% to 15% when we consider a T5 or a T9 theory, respectively. In figures 6.11 and 6.12 we show the behaviour of $\bar{\sigma}_{zz}$ and $\bar{\sigma}_{\beta z}$ along the shell's thickness. We notice that the introduction of trigonometric thickness functions can leads to variations of the solution. It is meaningful the wide variation between a T7 theory with respect to a T8 theory (Fig. 6.11). Then it is evident that theories developed from a new basis of trigonometric thickness

R_β/h	$\bar{u}_z(z=0)$			$\bar{\sigma}_{zz}(z=0)$			$\bar{\sigma}_{\beta z}(z=0)$		
	100	10	4	100	10	4	100	10	4
<i>3D</i> [119]	0.4715	1.223	4.009	-8.30	-1.27	-0.62	-3.127	-3.264	-2.349
<i>T11</i>	0.4737	1.264	4.329	-6.82	-1.27	-0.65	-2.949	-3.664	-2.895
<i>T10</i>	0.4737	1.263	4.332	-7.08	-1.31	-0.86	-3.028	-3.736	-2.800
<i>T9</i>	0.4737	1.265	4.508	-7.08	-1.27	-0.61	-3.028	-3.739	-2.840
<i>T8</i>	0.4737	1.263	4.497	-7.16	-1.26	-0.55	-2.898	-3.586	-2.719
<i>T7</i>	0.4737	1.262	4.448	-7.16	-1.27	-0.61	-2.898	-3.585	-2.709
<i>T6</i>	0.4736	1.243	4.343	-6.93	-1.28	-0.62	-2.468	-3.104	-2.283
<i>T5</i>	0.4736	1.243	4.362	-6.93	-1.28	-0.60	-2.468	-3.104	-2.289
<i>T4</i>	0.4732	1.212	4.323	-6.55	-1.37	-0.67	-1.845	-2.535	-2.099
<i>T3</i>	0.4732	1.212	4.312	-6.54	-1.37	-0.68	-1.845	-2.525	-2.095
<i>T2</i>	0.4716	1.003	3.367	-2.53	-1.08	-0.66	-0.635	-1.221	-1.154
<i>CLT</i>	0.4656	0.5205	0.4796						

Table 6.9. Maximum transverse deflection \bar{u}_z and maximum stresses $\bar{\sigma}_{zz}$ and $\bar{\sigma}_{\beta z}$ for $[90^\circ/0^\circ/90^\circ]$ circular cylindrical shell [119].

functions are effective depending on the terms that are adopted in the expansion. It becomes interesting to evaluate the importance of higher-order terms (see [32]).

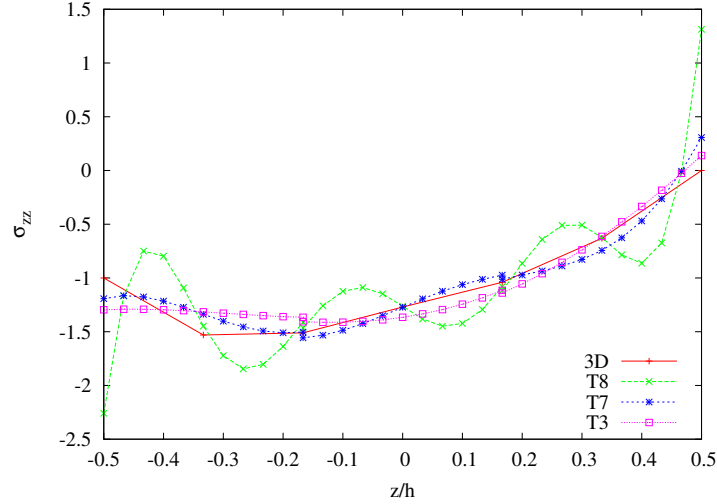


Figure 6.11. Distribution of stress $\bar{\sigma}_{zz}$ for $[0^\circ/90^\circ/0^\circ]$ cylindrical shell, $a/h = 10$. 3D solution in [119]

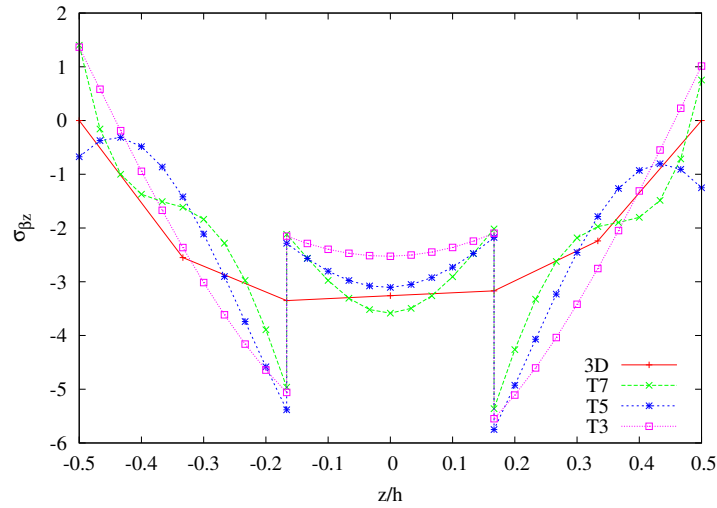


Figure 6.12. Distribution of stress $\bar{\sigma}_{\beta z}$ for $[0^\circ/90^\circ/0^\circ]$ cylindrical shell, $a/h = 10$. 3D solution in [119]

Another analysis was carried out considering a two layers $[0^\circ/90^\circ]$ lamination scheme. For the sake of brevity, results quoted in Figures 6.13, 6.14 and 6.15 are referred to the

$R_\beta/h = 10$ case and present the behaviour of the investigated quantities (Eq. 6.18) along the shell's thickness. We compared the solutions obtained for $N = 4$ for each theory that we have considered in the second part of the thesis, as the classical theories and the trigonometric ESL and LW. Being equal the approach adopted, the trends do not change, with or without the use of trigonometric functions. This applies especially to stresses, whereas the displacement \bar{u}_z undergoes an improvement when we consider the TN model, compared to the EDN one.

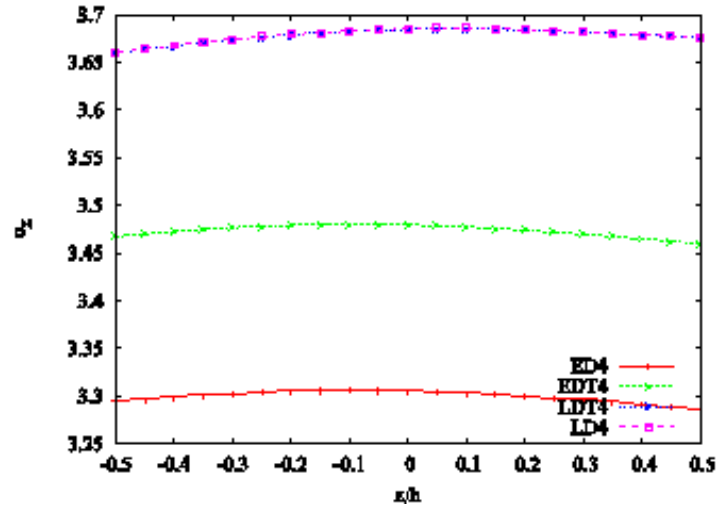


Figure 6.13. Distribution of displacement \bar{u}_z for $[0^\circ/90^\circ]$ cylindrical shell, $a/h = 10$. 3D solution in [119]

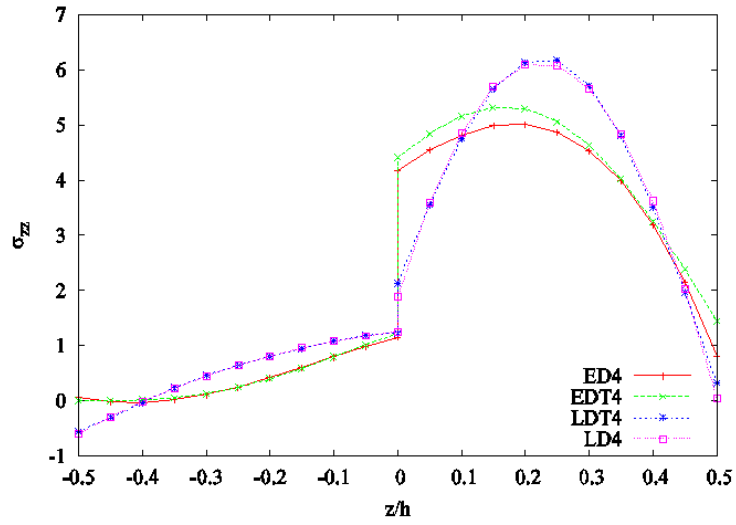


Figure 6.14. Distribution of stress $\bar{\sigma}_{zz}$ for $[0^\circ/90^\circ]$ cylindrical shell, $a/h = 10$. 3D solution in [119]

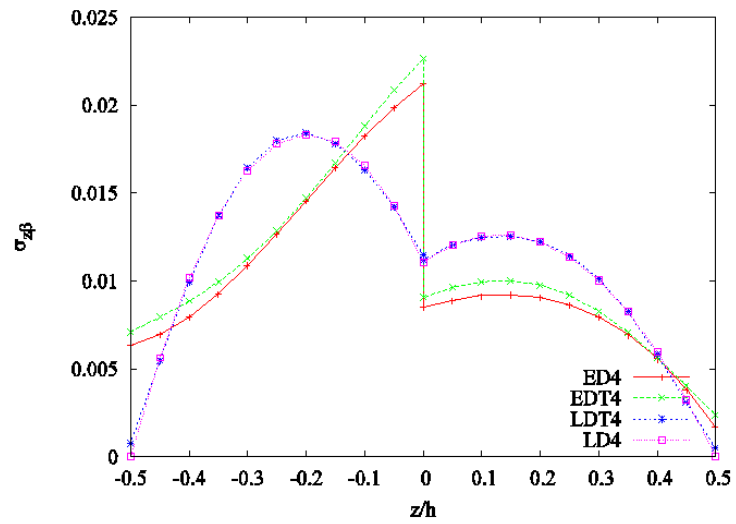


Figure 6.15. Distribution of stress $\bar{\sigma}_{\beta z}$ for $[0^\circ/90^\circ]$ cylindrical shell, $a/h = 10$. 3D solution in [119]

6.6 Conclusions

In the framework of axiomatic approaches which can be developed on the basis of variational statements, new trigonometric displacement distributions in the thickness of the shell z have been postulated. We presented higher-order shell theories based on Equivalent Single Layer approach that have been formulated on the basis of new kinematic assumptions. We built up a set of trigonometric thickness functions to write the assumed displacement field. Governing equations and boundary conditions were derived via the Principle of Virtual Displacement. A unified approach to formulate two-dimensional shell theories has been here addressed to evaluate the static response of cylindrical multilayered plates and shells made of composite materials. Navier-type closed form solution is considered, that corresponds to simply supported boundary conditions. All results have been compared with exact solutions available in literature. On the basis of the presented results, we can make some considerations about the effectiveness of the formulation. When the thickness of the shell becomes high, we need to use higher order theories, which provide better results compared to classical theories. It should be take into account that depending on the case considered we note that some terms used in the expansion are not very useful or even negative. We must therefore understand which order of expansion is appropriate depending on the problem being analysed. The theories that we have proposed are suitable for further investigation and in the opinion of the authors can bring improvements in the field of shells structural models.

Chapter 7

Conclusions

Carrera's Unified Formulation (UF) has been presented, in the framework of beams, as well as plates and shells modelling. The UF is based on a compact notation allowing to obtain classes of Equivalent Single Layer (ESL) or Layerwise (LW) theories characterised by the type of the main unknowns via the assumption of either the Principle of Virtual Displacement (PVD) or the Reissner's Mixed Variational Theorem (RMVT). Concerning the first part of the thesis, the free vibration analysis of thin-walled isotropic beams is carried out through a closed form, Navier type solution. Slender and deep beams are investigated. Bending, torsional and axial modes, as well as local modes are considered. Results are assessed toward finite element solutions. The numerical investigation has shown that the proposed unified formulation yields accurate results as long as the appropriate approximation order is considered. The accuracy of the solution depends upon the geometrical parameters of the beam.

Functionally graded beams have been introduced. Their modal response has been evaluated through higher-order models, in the framework of UF. Bending, torsion and axial modes are investigated. Slender as well as short beams are considered. Numerical results highlight the effect of different material distributions on natural frequencies and mode shapes and the accuracy of the proposed models.

The Unified formulation has been extended to evaluate the thermal behaviour of beams made of several materials. The temperature profile is determined by solving Fourier's heat conduction equation. The governing equations are, then, derived from the Principle of Virtual Displacements considering the temperature field as an external load. A Navier-type, closed form solution is used. Simply supported beams are, therefore, considered. Functionally graded mono-layer and sandwich cross-section configurations are investigated. Numerical results in terms of temperature, displacement and stress distributions are provided for different beam slenderness ratios. Results are assessed towards three-dimensional finite element solutions demonstrating that accurate results can be obtained with reduced computational costs.

Concerning the second part of the thesis, an introduction to Equivalent single layer and layer-wise models for shells analysis has been presented. These models have been applied

to the modal analysis of thin and moderately thick as well as shallow and deep shells. Several parametric analyses are carried out depending on the stacking sequences of laminates, on the degree of orthotropic ratio and the thickness and on the curvature parameters. Conclusions are drawn with respect to the accuracy of the theories for the considered lay-outs and geometrical parameters. In the framework of shells modelling, besides the polynomial approximation for the main unknown variables, we presented new basis functions for the assumed displacement field, that account for trigonometric variation. Equivalent single layer and Layer-wise shells theories based on trigonometric functions expansions are considered to evaluate the static behavior of multilayered, orthotropic plates and shells. Carrera Unified Formulation for the modeling of composite shell structures is adopted, extending the bases functions used for higher order shell theories to trigonometric bases functions. The governing differential equations of the problem are presented in a compact general form. These equations are solved via a Navier-type, closed form solution. The static behaviour of plates and shells is investigated. As assessment, results are compared with available exact solutions present in literature.

Bibliography

- [1] A. Alibeigloo. Static and vibration analysis of axi-symmetric angle-ply laminated cylindrical shell using state space differential quadrature method. *International Journal of Pressure Vessels and Piping*, 86:738–747, 2009.
- [2] A.E. Alshorbagy, M.A. Eltaher, and F.F. Mahmoud. Free vibration characteristics of a functionally graded beam by finite element method. *Applied Mathematical Modelling*, 35:412–425, 2011.
- [3] D. Ambrosini. On free vibration of nonsymmetrical thin-walled beams. *Thin-Walled Structures*, 47:629–636, 2009.
- [4] D. Ambrosini. Experimental validation of free vibrations from nonsymmetrical thin walled beams. *Engineering Structures*, 32:1324–1332, 2010.
- [5] v10.0 ANSYS. *theory manual*. ANSYS Inc., Southpointe, PA, 2006.
- [6] H. Arya, R.P. Shimpi, and N.K. Naik. A zigzag model for laminated composite beams. *Composite Structures*, 56(1):21–24, 2002.
- [7] R. Attarnejad, S. J. Semnani, and A. Shahba. Basic displacement functions for free vibration analysis of non-prismatic timoshenko beams. *Finite Elements in Analysis and Design*, 46(10):916–929, 2010.
- [8] M. Aydogdu and V. Taskin. Free vibration analysis of functionally graded beams with simply supported edges. *Materials and Design*, 28:1651–1656, 2007.
- [9] A. Bahtui and M. R. Eslami. Coupled thermoelasticity of functionally graded cylindrical shells. *Mechanics Research Communications*, 34(1):1–18, 2007.
- [10] E. J. Barbero. *Finite element analysis of composite materials*. CRC Press, New York, 2008.
- [11] R. Benamar, M. M. K. Bennouna, and R. G. White. The effects of large vibration amplitudes on the mode shapes and natural frequencies of thin elastic structures. part i: simply supported and clamped-clamped beams. *Journal of Sound and Vibration*, 149(2):179–195, 1991.
- [12] D. Bernoulli. *De vibrationibus et sono laminarum elasticarum*. In: *Commentarii Academiae Scientiarum Imperialis Petropolitanae*, petropoli edition, 1751.
- [13] A. Bhimaraddi. Free vibration analysis of doubly curved shallow shells on rectangular planform using three-dimensional elasticity theory. *International Journal of Solids and Structures*, 27(7):897–913, 1991.
- [14] S. Brischetto, R. Leetsch, E. Carrera, T. Wallmersperger, and B. Kröplin. Thermo-mechanical bending of functionally graded plates. *Journal of Thermal Stresses*, 31(3):286–308, 2008.

- [15] R. Byrne. Theory of small deformations of thin shells. *University of California at Los Angeles Publications on Mathematics*, 3:103–152, 1944.
- [16] A. Carpinteri and M. Paggi. Thermo-elastic mismatch in nonhomogeneous beams. *Journal of Engineering Mathematics*, 61(2-4):371–384, 2008.
- [17] E. Carrera. The effects of shear deformation and curvature on buckling and vibrations of cross-ply laminated composite shells. *Journal of Sound and Vibration*, 150:405–433, 1991.
- [18] E. Carrera. Evaluation of layer-wise mixed theories for laminated plates analysis. *AIAA Journal*, 26:830–839, 1998.
- [19] E. Carrera. Layer-wise mixed models for accurate vibration analysis of multilayered plates. *Journal of Applied Mechanics*, 65:820–828, 1998.
- [20] E. Carrera. An assessment of mixed and classical theories for the thermal analysis of orthotropic multilayered plates. *Journal of Thermal Stresses*, 23:797–831, 2000.
- [21] E. Carrera. An assessment of mixed and classical theories on global and local response of multilayered, orthotropic plates. *Computers and Structures*, 50:183–198, 2000.
- [22] E. Carrera. A priori vs. a posteriori evaluation of transverse stresses in multilayered orthotropic plates. *Composite Structures*, 48(4):245–260, 2000.
- [23] E. Carrera. Developments, ideas, and evaluations based upon reissners mixed variational theorem in the modeling of multilayered plates and shells. *Applied Mechanics Review*, 54:301–329, 2001.
- [24] E. Carrera. Temperature profile influence on layered plates response considering classical and advanced theories. *AIAA Journal*, 40(9):1885–1896, 2002.
- [25] E. Carrera. Historical review of zig-zag theories for multilayered plates and shells. *Applied Mechanics Review*, 56:287–308, 2003.
- [26] E. Carrera. Theories and finite elements for multilayered plates and shells: a unified compact formulation with numerical assessment and benchmarking. *Archives of Computational Methods in Engineering*, 10(3):215–296, 2003.
- [27] E. Carrera. On the use of murakami’s zig-zag function in the modeling of layered plates and shells. *Composite Structures*, 82(7-8):541–554, 2004.
- [28] E. Carrera and S. Brischetto. Analysis of thickness locking in classical, refined and mixed multilayered plate theories. *Composite Structures*, 82(4):549–562, 2008.
- [29] E. Carrera and S. Brischetto. Analysis of thickness locking in classical, refined and mixed theories for layered shells. *Composite Structures*, 85(1):83–90, 2008.
- [30] E. Carrera, G. Giunta, P. Nali, and M. Petrolo. Refined beam elements with arbitrary cross-section geometries. *Computers and Structures*, 88(5-6):283–293, 2010.
- [31] E. Carrera, G. Giunta, and M. Petrolo. *Beam Structures: Classical and Advanced Theories*, Wiley Series in Computational Mechanics. John Wiley and Sons, ISBN: 978-0-470-97200-7, 2011.
- [32] E. Carrera and M. Petrolo. On the effectiveness of higher-order terms in refined beam theories. *Journal of Applied Mechanics*, 78(2):pp.17, 2011.
- [33] A. Chakraborty, S. Gopalakrishnan, and J. N. Reddy. A new beam finite element for the analysis of functionally graded materials. *International Journal of Mechanical Sciences*, 45(3):519–539, 2003.

- [34] R.Z. Chaudhuri and H.R.H. Kabir. Static and dynamic fourier analysis of finite cross-ply doubly curved panels using classical shallow shell theories. *Composite Structures*, 28:73–91, 1994.
- [35] H. H. Chen and K. M. Hsiao. Coupled axial-torsional vibration of thin-walled z-section beam induced by boundary conditions. *Thin-Walled Structures*, 45:573–583, 2007.
- [36] H. H. Chen and K. M. Hsiao. Quadruply coupled linear free vibrations of thin-walled beams with a generic open section. *Engineering Structures*, 30:1319–1334, 2008.
- [37] W. Q. Chen, C. F. Lü, and Z. G. Bian. A semi-analytical method for free vibration of straight orthotropic beams with rectangular cross-sections. *Mechanics Research Communications*, 31(6):725–734, 2004.
- [38] G. R. Cowper. The shear co-efficient in timoshenko beam theory. *Journal of Applied Mechanics*, 33(10):335–340, 1966.
- [39] F. de Borbón and D. Ambrosini. On free vibration analysis of thin-walled beams axially loaded. *Thin-Walled Structures*, 48:915–920, 2010.
- [40] A. De Saint-Venant. Mémoire sur la flexion des prismes. *Journal de Mathématiques pure et appliqués*, 1:89–189, 1856.
- [41] L.H. Donnell. Stability of thin-walled tubes under torsion. *NACA Report*, 479:1–24, 1933.
- [42] H. Duan. Nonlinear free vibration analysis of asymmetric thin-walled circularly curved beams with open cross section. *Thin-Walled Structures*, 46:1107–1112, 2008.
- [43] L. Euler. De curvis elasticis. In: *Methodus Inveniendi Lineas Curvas Maximi Minimi Proprietate Gaudentes, Sive Solutio Problematis Isoperimetrici Lattissimo sensu Accepti*, 1744. Bousquet.
- [44] S. A. Fazelzadeh and M. Hosseini. Aerothermoelastic behavior of supersonic rotating thin-walled beams made of functionally graded materials. *Journal of Fluids and Structures*, 23(8):1251–1264, 2007.
- [45] A.J.M. Ferreira, E. Carrera, M. Cinefra, C.M.C. Roque, and O. Polit. Analysis of laminated shells by a sinusoidal shear deformation theory and radial basis functions collocation, accounting for through-the-thickness deformations. *Composites Part B: Engineering*, 42(5):1276–1284, 2011.
- [46] A.J.M. Ferreira, C.M.C. Roque, and R.M.N. Jorge. Analysis of composite plates by trigonometric shear deformation theory and multiquadrics. *Computers and Structures*, 83(27):2225–2237, 2005.
- [47] A.J.M. Ferreira, C.M.C. Roque, and R.M.N. Jorge. Static and free vibration analysis of composite shells by radial basis functions. *Engineering Analysis with Boundary Elements*, 30:719–733, 2006.
- [48] W. Flügge. *Statik und Dynamik der Schalen*. Berlin: Springer-Verlag, 1934.
- [49] M. Ganapathi. Dynamic stability characteristics of functionally graded materials shallow spherical shells. *Composite Structures*, 79(3):885–902, 2007.
- [50] G. L. Ghiringhelli. On the thermal problem for composite beams using a finite element semi-discretisation. *Composite Part B*, 28(5-6):483–495, 1997.

-
- [51] J. B. Gunda, R. K. Gupta, G. R. Janardhan, and G. V. Rao. Large amplitude free vibration analysis of timoshenko beams using a relatively simple finite element formulation. *International Journal of Mechanical Science*, doi:10.1016/j.ijmecsci.2010.07.009, 2010.
- [52] R.B. Hetnarski and M.R. Eslami. *Thermal stresses - Advanced theory and applications*. Springer, 2009.
- [53] F.B. Hildebrand, E. Reissner, and G.B. Thomas. Note on the foundations of the theory of small displacements of orthotropic shells. *NACA-TN*, 1833:1–59, 1949.
- [54] X. L. Huang and H. S. Shen. Nonlinear vibration and dynamic response of functionally graded plates in thermal environments. *International Journal of Solids and Structures*, 41(9–10):2403–2427, 2004.
- [55] R.M. Jones. *Mechanics of composite materials*. Taylor & Francis, 1999.
- [56] L. Jung, H. Hongxing, S. Rongying, and J. Xianding. Dynamic response of axially loaded monosymmetrical thin-walled bernoulli-euler beams. *Thin-Walled Structures*, 42:1689–1707, 2004.
- [57] R. Kadoli, K. Akhtara, and N. Ganesanb. Static analysis of functionally graded beams using higher order shear deformation theory. *Applied Mathematical Modelling*, 32(12):2509–2525, 2008.
- [58] S. Kapuria, M. Bhattacharyya, and A. N. Kumarb. Bending and free vibration response of layered functionally graded beams: A theoretical model and its experimental validation. *Composite Structures*, 82(3):390–402, 2008.
- [59] S. Kapuria, P. C. Dumir, and A. Ahmed. An efficient higher order zigzag theory for composite and sandwich beams subjected to thermal loading. *International Journal of Solids and Structures*, 40:6613–6631, 2003.
- [60] W.T. Koiter. A consistent first approximation in the general theory of thin elastic shells. *Proc. of Symp. on the Theory of Thin Elastic Shells*, pages 12–23, 1959.
- [61] H. Kraus. *Thin Elastic Shells*. John Wiley & Sons, New York, 1967.
- [62] A.W. Leissa. *Vibration of shells*. NASA Report SP-288, 1973.
- [63] X. F. Li. A unified approach for analyzing static and dynamic behaviors of functionally graded timoshenko and euler-bernoulli beams. *Journal of Sound and Vibration*, 318(4–5):1210–1229, 2008.
- [64] L. Librescu, S.Y. Oh, and O. Song. Spinning thin-walled beams made of functionally graded materials: modeling, vibration and instability. *European Journal of Mechanics - A/Solids*, 23(3):499–515, 2004.
- [65] K.M. Liew, L.X. Peng, and T.Y. Ng. Three-dimensional vibration analysis of spherical shell panels subjected to different boundary conditions. *International Journal of Mechanical Sciences*, 44:2103–2117, 2002.
- [66] A. E. H. Love. The small free vibrations and deformation of a thin elastic shell. *Philosophical Transactions of the Royal Society of London, A*, 179:491–546, 1888.
- [67] A.L. Lur'e. The general theory of elastic shells. *Priklady Matematika y Mekanika*, 4:7–34, 1940.
- [68] E. Madenci and I. Guven. *The Finite Element Method and Applications in Engineering using ANSYS®*. Springer, New York, USA, 2006.

- [69] R.M. Mahamood, E.T. Akinlabi, M. Shukla, and S. Pityana. Functionally graded material: An overview. *Proceedings of the World Congress on Engineering*, 3:1593–1597, 2012.
- [70] A. Mahi, E. A. Adda Bedia, A. Tounsi, and I. Mechab. An analytical method for temperature-dependent free vibration analysis of functionally graded beams with general boundary conditions. *Composite Structures*, 92:1877–1887, 2010.
- [71] H. Matsunaga. Buckling instabilities of thick elastic beams subjected to axial stresses. *Computers and structures*, 59(5):859–868, 1996.
- [72] H. Matsunaga. Free vibration and stability of thin elastic beams subjected to axial forces. *Journal of Sound and Vibration*, 191(5):917–933, 1996.
- [73] H. Matsunaga. Vibration and buckling of cross-ply laminated composite circular cylindrical shells according to a global higher-order theory. *International Journal of Mechanical Sciences*, 49:1060–1075, 2007.
- [74] R.D. Mindlin. Influence of the rotatory inertia and shear on flexural motions of isotropic elastic plates. *Journal of Applied Mechanics*, 18:31–38, 1951.
- [75] T. Mori and K. Tanaka. Average stress in matrix and average elastic energy of materials with misfitting inclusions. *Acta Metall*, 21:571–574, 1973.
- [76] M. Murakami. Laminated composites plate theory with improved in-plane responses. *Journal of Applied Mechanics*, 53:661–666, 1986.
- [77] J. Murin, M. Aminbaghai, and V. Kutis. Exact solution of the bending vibration problem of fgm beams with variation of material properties. *Engineering Structures*, 32:1631–1640, 2010.
- [78] A. V. K. Murty. Analysis of short beams. *AIAA Journal*, 8:2098–2100, 1970.
- [79] K.M. Mushtari. *On the stability of cylindrical shells subjected to torsion*. Trudy Karanskego auiatsionnugo inatituta, 1938.
- [80] P.M. Naghdi. A survey of recent progress in the theory of elastic shells. *Applied Mechanics Review*, 9:365–368, 1956.
- [81] M.C. Narasimhan and R.S. Alwar. Free vibration analysis of laminated orthotropic spherical shells. *Journal of Sound and Vibration*, 154(3):515–529, 1992.
- [82] N. Noda. Thermal stresses in functionally graded materials. *Journal of Thermal Stresses*, 22:477–512, 1999.
- [83] S.-Y. Oh, L. Librescu, and O. Song. Vibration and instability of functionally graded circular cylindrical spinning thin-walled beams. *Journal of Sound and Vibration*, 285(4-5):1071–1091, 2005.
- [84] N. J. Pagano. Exact solutions for composite laminates in cylindrical bending. *Journal of Composites Materials*, 3:398–411, 1969.
- [85] N. J. Pagano and S. J. Hatfield. Elastic behavior of multilayered bidirectional composites. *AIAA Journal*, 10(7):931–933, 1972.
- [86] G. M. Philips. *Interpolation and approximation by polynomials*. Springer-Verlag, 2003.
- [87] A.L. Poore, A. Barut, and E. Madenci. Free vibration of laminated cylindrical shells with a circular cutout. *Journal of Sound and Vibration*, 312:55–73, 2008.
- [88] G. N. Praveen and J. N. Reddy. Nonlinear transient thermoelastic analysis of functionally graded ceramic-metal plates. *International Journal of Solids and Structures*,

- 35(33):4457–4476, 1998.
- [89] M.S. Qatu. Accurate stress resultant equations for laminated composite deep thick shells. *Composites for the pressure vessel industry, ASME-PVP*, 302:39–46, 1995.
- [90] M.S. Qatu. Accurate equations for laminated composite deep thick shells. *International Journal of Solids and Structures*, 36:2917–2941, 1999.
- [91] M.S. Qatu. Recent research advances in the dynamic behavior of shells. part 1 : Laminated composite shells. *Applied Mechanics Reviews*, 55:325–350, 2002.
- [92] M.S. Qatu. Recent research advances in the dynamic behavior of shells. part 2: Homogeneous shells. *Applied Mechanics Reviews*, 55:415–434, 2002.
- [93] M.S. Qatu. Vibration of homogeneous and composite thick barrel shells. *Journal of Vibration and Control*, 10:319–341, 2004.
- [94] M.S. Qatu. *Vibration of Laminated Shells and Plates*. Elsevier, 2004.
- [95] M.S. Qatu. Recent research advances on the dynamic analysis of composites shells: 2000-2009. *Composite Structures*, 93:14–31, 2010.
- [96] L. F. Qian, R. C. Batra, and L. M. Chena. Static and dynamic deformations of thick functionally graded elastic plates by using higher-order shear and normal deformable plate theory and meshless local petrov-galerkin method. *Composites Part B: Engineering*, 35(6-8):685–697, 2004.
- [97] J. N. Reddy. *Mechanics of Laminated Composite Plates and Shells Theory and Analysis*. CRC Press, Boca Raton, Florida, USA, 2nd edition, 2004.
- [98] J.N. Reddy. An evaluation of equivalent-single-layer and layerwise theories of composite laminates. *Composite Structures*, 25:21–35, 1993.
- [99] J.N. Reddy and C.F. Liu. A higher-order shear deformation theory of laminated elastic shells. *International Journal of Engineering Science*, 23(3):319–330, 1985.
- [100] E. Reissner. Stress-strain relations in the theory of thin elastic shells. *Journal of Mathematical Physics*, 31:109–119, 1952.
- [101] E. Reissner. On a certain mixed variational theory and a proposed application. *International Journal for Numerical Methods in Engineering*, 20:1366–1368, 1984.
- [102] E. Reissner. On a mixed variational theorem and on shear deformable plate theory. *International Journal for Numerical Methods in Engineering*, 23:193–198, 1986.
- [103] J.G. Ren. Exact solutions for laminated cylindrical shells in cylindrical bending. *Composites Science and Technology*, 29(3):169–187, 1987.
- [104] C.M.C. Roque, A.J.M. Ferreira, and R.M.N Jorge. Modelling of composite and sandwich plates by a trigonometric layerwise deformation theory and radial basis functions. *Composites Part B: Engineering*, 36(8):559–572, 2005.
- [105] K.S. Sai Ram and T. Sreedhar Babu. Free vibration of composite spherical shell cap with and without a cutout. *Computers and Structures*, 80:1749–1756, 2002.
- [106] L. Sanders. Nonlinear theories for thin shells. *Quarterly of Applied Mathematics*, 21:21–36, 1963.
- [107] O. Sayman. An elastic-plastic thermal stress analysis of aluminum metal-matrix composite beams. *Composite Structures*, 53:419–425, 2001.
- [108] H. S. Shen. Thermal postbuckling behavior of functionally graded cylindrical shells with temperature-dependent properties. *International Journal of Solids and Structures*, 41(7):1961–1974, 2004.

- [109] R.P. Shimpi and Y.M. Ghugal. A new layerwise trigonometric shear deformation theory for two-layered cross-ply beams. *Composites Science and Technology*, 61(9):1271–1283, 2001.
- [110] M. Simsek. Fundamental frequency analysis of functionally graded beams by using different higher-order beam theories. *Nuclear Engineering and Design*, 240:697–705, 2010.
- [111] S.A. Sina, H.M. Navazi, and H. Haddadpour. An analytical method for free vibration analysis of functionally graded beams. *Materials and Design*, 30:741–747, 2009.
- [112] K.P. Soldatos. Influence of thickness shear deformation on free vibrations of rectangular plates, cylindrical panels and cylinders of antisymmetric angle-ply construction. *Journal of Sound and Vibration*, 119:111–137, 1987.
- [113] M. Tanaka and A. N. Bercin. Free vibration solution for uniform beams of non-symmetrical cross section using mathematica. *Computers and Structures*, 71:1–8, 1999.
- [114] Y. Tanigawa, H. Murakami, and Y. Ootao. Transient thermal stress analysis of a laminated composite beam. *Journal of Thermal Stresses*, 12(1):25–39, 1989.
- [115] S. P. Timoshenko. On the corrections for shear of the differential equation for transverse vibrations of prismatic bars. *Philosophical Magazine*, 41:744–746, 1921.
- [116] S. P. Timoshenko. On the transverse vibrations of bars of uniform cross section. *Philosophical Magazine*, 43:125–131, 1922.
- [117] Y. S. Touloukian. *Thermophysical properties of high temperature solid materials*. MacMillan, New York, 1967.
- [118] N. F. J. van Rensburg and A. J. van der Merwe. Natural frequencies and modes of a timoshenko beam. *Wave Motion*, 44(1):58–69, 2006.
- [119] T.K. Varadan and K. Bhaskar. Bending of laminated orthotropic cylindrical shells - an elasticity approach. *Composite Structures*, 17(2):141–156, 1991.
- [120] P. Vidal and O. Polit. A thermomechanical finite element for the analysis of rectangular laminated beams. *Finite Elements in Analysis and Design*, 42:868–883, 2006.
- [121] P. Vidal and O. Polit. A family of sinus finite elements for the analysis of rectangular laminated beams. *Composite Structures*, 84(1):56–72, 2008.
- [122] P. Vidal and O. Polit. A sine finite element using a zig-zag function for the analysis of laminated composite beams. *Composite Part B: Engineering*, 42(6):1671–1682, 2011.
- [123] G. M. Vörös. On coupled bending-torsional vibrations of beams with initial loads. *Mechanics Research Communications*, 36:603–611, 2009.
- [124] H. Wang and Q-H. Qin. Meshless approach for thermo-mechanical analysis of functionally graded materials. *Engineering Analysis with Boundary Elements*, 32(9):704–712, 2008.
- [125] N. Wattanasakulpong, B. Gangadhara Prusty, and Kelly D.W. Thermal buckling and elastic vibration of third-order shear deformable functionally graded beams. *International Journal of Mechanical Sciences*, 53:734–743, 2011.
- [126] J. Woo and S. A. Meguid. Nonlinear analysis of functionally graded plates and shallow shells. *International Journal of Solids and Structures*, 38(42–43):7409–7421, 2001.

- [127] P.B. Xavier, C.H. Chew, and K.H. Lee. Buckling and vibration of multilayer orthotropic composite shells using a simple higher-order layerwise theory. *International Journal of Solids and Structures*, 32(23):3479–3497, 1995.
- [128] H. J. Xiang and J. Yang. Free and forced vibration of a laminated fgm timoshenko beam of variable thickness under heat conduction. *Composites:Part B*, 39:292–303, 2008.
- [129] Y. Xu and D. Zhou. Two-dimensional thermoelastic analysis of beams with variable thickness subjected to thermo-mechanical loads. *Applied Mathematical Modelling*, doi: 10.1016/j.apm.2012.01.048, 2012.
- [130] D. Yadav and N. Verma. Free vibration of composite circular cylindrical shells with random material properties. *Composite Structures*, 51:371–380, 2001.
- [131] J. Ye and K.P. Soldatos. Three-dimensional vibration of laminated cylinders and cylindrical panels with symmetric or antisymmetric cross-ply lay-up. *Composites Engineering*, 4:429–444, 1994.
- [132] X. Zhao, K.M. Liew, and T.Y. Ng. Vibration analysis of laminated composite cylindrical panels via a meshfree approach. *International Journal of Solids and Structures*, 40:161–180, 2003.

Curriculum Vitae

Name	Daniela Crisafulli
Date of birth	29 May 1984
Place of birth	Milazzo (ME), Italy
e-mail	daniela.crisafulli@polito.it

Education

January 2010 - December 2012	Ph.D. student at Politecnico di Torino and Université Paris Ouest - Nanterre La Défense
October 2006 - Mars 2009	Master of Science degree in Aerospace engineering at Politecnico di Torino
September 2003 - October 2006	Bachelor degree in Aerospace engineering at Politecnico di Torino

Professional experience

April 2010 - April 2013	Employee at CRP H. Tudor of Luxembourg
July 2009 - January 2010	Research assistantships at Politecnico di Torino